A proton source in the ALPHA apparatus for precision measurements of antihydrogen and hydrogen

by Patrick Stephen Mullan

Swansea University
Prifysgol Abertawe

Submitted to Swansea University in fulfilment of the requirements for the Degree of Doctor of Philosophy

May 2023

Patrick Stephen Mullan, 2023

Abstract

The apparent lack of antimatter within our local solar system, the Milky Way, and at Galactic boundaries is inconsistent with the Big Bang hypothesis. This disagreement has motivated many experiments to compare the properties and behaviour of antimatter and matter. The ALPHA (Antihydrogen Laser PHysics Apparatus) experiment produce, trap and study antihydrogen. This synthesis involves antiprotons sourced from the limited schedule of the Antiproton Decelerator facility. The restricted availability hinders the number of novel antiproton experiments, which could potentially increase the number of trapped antihydrogen atoms per Antiproton Decelerator cycle. Some of these studies can be performed using a substitute for antiprotons, such as protons, allowing the limited antiprotons to be used during the implementation of their results.

This research demonstrates a method that adapts an existing Penning trap to produce protons on demand within reasonable operating time scales of minutes. The availability of protons enables the consideration of new physics studies within ALPHA, including hydrogen formation, trapping, and possibly *in situ* hydrogen-antihydrogen comparisons. The study produced protons from radiofrequency-driven electrons through electron impact ionisation of the cryogenic Penning trap residual gas. The resulting positive ions were sympathetically cooled and compressed by positrons. All positive ions, except protons, were ejected from the trapping potentials using the autoresonance method. The remaining trapped population is approximately $(0.9 - 1.2) \times 10^6$ protons.

This research proves the feasibility of generating protons within the ALPHA apparatus, paving the way for future prospects of hydrogen generation.

Declaration

This work has not previously been accepted in substance for any degree and is not being concurrently submitted in candidature for any degree.
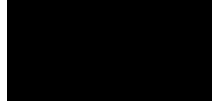
Patrick Stephen Mullan, 24th May 2023

This thesis is the result of my own investigations, except where otherwise stated. Other sources are acknowledged by footnotes giving explicit references. A bibliography is appended.

Patrick Stephen Mullan, 24th May 2023

I hereby give consent for my thesis, if accepted, to be available for photocopying and for inter-library loan, and for the title and summary to be made available to outside organisations.

Patrick Stephen Mullan, 24th May 2023

The University's ethical procedures have been followed and, where appropriate, that ethical approval has been granted.

Patrick Stephen Mullan, 24th May 2023

CONTENTS

ACKNOWLEDGEMENT

Antimatter is truly as natural as everything around us, though it is plainly a faint detail that has eluded us until modern times. Although it is not as ghostly as neutrinos, it is delicate and vanishes upon touch. This behaviour might inspire the imagination, though it is surely not what makes antimatter research profitable. Matter-antimatter comparisons have been an essential vehicle for moving the understanding of fundamental physics forward, it breaks beautifully symmetric theories and brings us all back to reality.

1.1 Antiprotons, positrons and antihydrogen

In 1928 Dirac derived a relativistic quantum theory [1], he noted the validity of positively charged electron solutions within the theory, and naturally excluded them as charge-conjugate transitions are not observed experimentally. Although persistence by the community pushed for a more critical consideration of the "meaning" of such solutions. Initial discussions consider unoccupied positively charged solutions as protons, though by 1930 Oppenheimer [2] logically argued for the interpretation of two distinct oppositely charged particles with an electron mass. In 1931 Dirac [3] made a further statement on the possible existence of the antiproton. During the following year Carl D. Anderson published evidence of positrons [4] produced by cosmic rays colliding with a lead plate, causing pair production and opposing magnetic deflections of similar curvature. Just over 20 years later in 1955, a University of California group confirmed the existence of antiprotons by using the Bevatron accelerator facility [5], by which an accelerated proton beam hit a copper target and negative products were magnetically filtered.

During the initial few years after Dirac's 1928 paper, an electron annihilation process was hypothesised, where an electron transitions to an unoccupied positively charged solution, causing both the electron and positron to vanish. From both conservation

of energy and conservation of momentum arguments, such a process would require the emission of at least two γ-rays. Remarkably this phenomena is observed, as a low energy electron-positron pair will annihilate to emit two 511 keV γ-rays. When the rest mass energy and kinetic energy of an annihilating particle-antiparticle pair is large enough pair production of other particle-antiparticle pairs will occur, for example annihilation of a low energy proton-antiproton pair typically produces various pion particles.

The list of observed antiparticles has grown, and the charge, parity and time reversal (CPT) theorem, discussed later in Section 1.3.1, predicts the existence of counterpart antiparticle for each known "ordinary" particle. Once the existence of both positrons and antiprotons was known, an interest appeared for the bound state antihydrogen. This was confirmed by the PS210 experiment in 1995 at the CERN-LEAR, Low Energy Anti-Proton Ring, facility [6]. A beam of antiprotons hit a xenon gas target causing electron-positron pair production and subsequent positron capture. Soon after, Fermilab Experiment E862 had also produced antihydrogen atoms [7]. The PS210 experiment has been succeeded by the Antiproton Decelerator (AD) facility, at European Organisation for Nuclear Research (CERN).

1.2 Baryon asymmetry

With the development of astronomical techniques in the early twentieth century, it became clear that astronomical objects are receding from our solar system at increasing speeds proportional to their distance from us. This is known as the Hubble–Lemaître law [8, 9] and is evidence of the universe expanding. Later with the discovery of the cosmic microwave background, which is a far-field source of microwaves, the Big Bang hypothesis gained serious support. This hypothesis assumes the early universe was minute, hot and dense, these initial conditions predict early element abundances and the cosmic microwave background. A consequence of this hypothesis is that matter was produced by pair production during the early universe, and its abundance would be due to the equilibrium of pair production and annihilation processes. The energy density of the universe decreased as it expanded. During early periods, pair production processes for lighter and lighter masses become near non-existent. Eventually pair production became insignificant on a universal scale. Antimatter dominated astronomical objects have not been found yet. If antimatter existed in the local vicinity to matter then an annihilation boundary would be outlined by a glow of γ-rays. Also, if antimatter stars formed then their outward solar winds would contain anti-helium. The Alpha Magnetic Spectrometer is located on the International Space Station, this is currently a second generation experiment, it is a wide energy range charge particle detector [10]. Anti-helium detection events have been found, but those have been limited and have yet to be verified. Observed

extrasolar fluxes of positrons are nearly consistent with cosmic-ray mechanisms.

To reconcile the apparent absence of antimatter in the present universe with the Big Bang hypothesis, there must have been a process in the early universe that generated an asymmetry between matter and antimatter. This phenomenon is known as baryogenesis.

1.3 Tests of Physics

1.3.1 CPT Symmetry

The application of mathematics within physics has been an effective tool, this has been done by a reduction of generalisable mathematics to restricted forms. These restrictions are, in part, symmetries imposed by us. Restrictions allow us to formulate concise mathematical descriptions, such as the Standard Model of Particle Physics.

A physics theory is symmetric with respect to a transformation if the transformation of the theory does not change its predictions. In the early 20th century, particle physics theories had three symmetries, charge conjugation (C), parity inversion (P) and time reversal (T). C inverts the electric charge sign of fundamental particles, P reflects all coordinate unit vectors, this is distinct from a rotation, and T reverses the flow of time. In 1956 theorists Lee and Yang [11] reviewed previous weak interaction studies, with the intent of clarifying the absence of parity conservation measurements. In the very same year, motivated by this review, Wu *et al.* [12] measured a parity violation occurring in the β decay of Co^{60}, where the spin direction of decayed electrons have a preference to anti-align to the nuclear spin of Co^{60}. This was accounted for in successive theories that exhibited a combined CP symmetry. Later, kaon decay experiments measured a charge-parity violation. The current Standard Model of Particle Physics integrates these and more symmetry violating mechanisms within its mathematical description. This theory has a combined symmetry of all three symmetries, charge-parity-time (CPT) symmetry, such that it is identical to the CPT transform of itself.

A theory that encapsulates the predictions of both the Standard Model of Particle Physics and General Relativity has yet to be formed. It has been difficult for novel fundamental physics experiments to be proposed because of the lack of awareness of where the individual theories fail. Therefore, an effective theory has been formulated called the Standard Model Extension [13]. This framework allows different types of Lorentz and CPT violations to be quantified, which has been characterised for antihydrogen and hydrogen physics [14].

1.3.2 Gravity

General relativity does not distinguish between matter and antimatter, though it has been formulated from observations of our apparently matter dominated universe. The Weak Equivalence Principle states that the motion of all point-like fundamental particles within a gravitational field is defined by its initial velocity and position regardless of its constituent particles. The vertical gravitational potential energy gradient for hydrogen (or protons) within a laboratory on Earth is 0.1 μeV m^{-1}. Gravitational measurements of electrically charged antimatter [15] are difficult due to stray patch potentials and other electric field generating systematic effects [16]. Instead, modern efforts focus on the neutral antihydrogen atom and the mixed matter-antimatter systems of positronium and muonium.

There are three experiments that aim to measure the gravitational effect of the Earth on antihydrogen. The Antihydrogen Experiment: Gravity, Interferometry, Spectroscopy (AEGIS) aim to measure the gravitational deflection of an antihydrogen beam [17]. Alternatively, both the ALPHA-g and the Gravitational Behaviour of Antimatter at Rest (GBAR) experiment aim to measure the gravitational free-fall path of antihydrogen [18]. The ALPHA experiment performed a proof-of-principle measurement of the gravitation mass of antihydrogen, though it is not in ideal vertical orientation. The gravitational mass was bound to greater than -65 and less than 110 times the hydrogen mass with 95% confidence [19]. This demonstration helped motivate the development of ALPHA-g.

The Weak Equivalence Principle can be split into two tests, the previously described free-fall test and the second is a matter clock and antimatter clock test of time dilation within a gravitation field [20]. The Baryon Antibaryon Symmetry Experiment (BASE) perform precision measurements of the antiproton-proton charge-to-mass ratio. They have constrained the differential clock Weak Equivalence Principle to a 3% level [21].

1.4 Short history of the field

1.4.1 The Antiproton Decelerator

As mentioned previously, the initial demonstration of antihydrogen production was in flight, not trapped. Thus in these experiments any antihydrogen produced would be lost on the order of 100 ns from annihilation with the apparatus. This was not ideal for studying its properties, which partially motivated the construction of a facility dedicated to decelerating antiprotons for the production and study of antihydrogen. This has been one of the key objectives of the Antiproton Decelerator (AD) at CERN [22]. This facility accepts a 25 GeV proton beam from CERN's

Proton Synchrotron every 120 s. Antiprotons are produced by pair production via proton-proton collisions. In practise, the proton beam is directed onto a proton dense material to increase the rate of proton-proton collisions. The AD uses an iridium target [23]. Antiprotons are magnetically filtered from scattered products and magnetically guided into the AD ring. Captured antiprotons are decelerated to energies of 5.3 MeV, to be then transported to one of the many user experiments [24]. The existing experiments are AEGIS, ALPHA, ASACUSA, BASE and GBAR. BASE performs precision comparisons of antiprotons and protons [25]. They have two primary measurements, the magnetic moment and the charge-to-mass ratio of the antiproton and proton. AEGIS produces cold antihydrogen from positronium-antiproton collisions, with a goal of measuring gravitational deflections of an anti-hydrogen beam [26]. ASACUSA has two primary spectroscopy experiments. One is spectroscopy of the hyperfine ground-state splitting of an antihydrogen beam produced by mixing positrons and antiprotons [27]. Their other experiment is spec-troscopy of Rydberg state antiprotonic helium. This second experiment measures the antiproton-electron mass ratio [28]. GBAR aims to measure the gravitational freefall of antihydrogen [18]. They aim to produce cold antihydrogen ions $\bar{H}^+$. A laser will then photodetach the outer positron to produce neutralised antihydrogen. During the period of this thesis. the AD facility underwent an upgrade, which aimed to further reduce the antiproton beam energy from 5.3 MeV to 0.1 MeV and improve the antiproton bunch density provided to the AD's user experiments. This upgrade is the Extra Low Energy Antiproton Project (ELENA) [29]. It is a decelerator ring coupled with the AD. ELENA was commissioned during the second long shutdown of CERN. The ALPHA antiproton Catching Trap would perform very poorly at capturing antiprotons from ELENA because the energy degrading foil was too thick for the reduced beam energy. This has meant that once the studies within this thesis concluded, the antiproton catch trap was upgraded with a thinner energy degrader foil and a large cryostat redesign [30].

1.4.2 ALPHA progress

The ALPHA-2 apparatus is primarily an antihydrogen spectroscopy experiment. The hydrogen atom can be considered a simple system to theoretically describe, allowing for high-order QED terms to be calculated. The 1S-2S hydrogen transition has been measured to a relative precision of 4.2×10^{-15} [31]. This means that a measurement of the antihydrogen 1S-2S transition can be used to test CPT sym-metry to high precision. Progress has already been made, as ALPHA has measured 1S-2S antihydrogen transitions to a consistent relative precision of 2×10^{-12} [32]. Additionally, both the ground-state hyperfine structure and two of the 1S-2P fine structure of the antihydrogen have been measured so far [33, 34]. The ALPHA

Collaboration has also made progress in the assembly and commissioning of their antihydrogen gravitational experiment, ALPHA-g. The neutral atom traps used by ALPHA to contain antihydrogen have a cylindrical geometry with a small trap diameter relative to the trap body length. The ALPHA-g apparatus has both its cylindrical axisymmetric axis aligned parallel to the normal of the Earth's surface and has a longer trap body length than the ALPHA-2 experiment. This increased vertical height occupied by the antihydrogen neutral trap causes the trapped atoms to be more sensitive to the Earth's gravitational potential across the entire trap length. The initial version of the ALPHA-g experiment aims to measure the gravitational mass of antihydrogen with an absolute precision comparable to the value of hydrogen. This is why it is often called an up-down measurement. Recently, laser cooling of antihydrogen was demonstrated by the ALPHA-2 experiment [35]. Laser cooling uses a laser field to cool the trapped atoms. The application of this method is expected to be beneficial to both spectroscopy and gravitational measurements as colder trapped antihydrogen will reduce both the line-broadening systematics in spectroscopy and reduce the trapped antihydrogen energies towards the energy scale of the gravitational potential difference across the length of the ALPHA-g neutral atom trap.

The ALPHA Collaboration has dozens of members that actively pursue many other projects with the common goal of producing and trapping antihydrogen. These efforts range from further reducing the limits on the positron temperature by sympathetic cooling with laser cooled Beryllium [36], to developing novel plasma reproducibility techniques [37] and novel systematic diagnostics [38], all to optimise the production and trapping of antihydrogen.

1.5 Aims of the presented work

A precision comparison of antihydrogen and hydrogen requires a detailed understanding of systematic effects, which is a combination of the apparatus and the measurement methodology. A poor understanding of systematics produces inaccuracies, such an error can appear falsely as new physics, or it could falsely hide new physics. Since the ALPHA antihydrogen neutral trap is in theory capable of trapping cold hydrogen atoms, a direct comparison might be possible. There are two technical developments that are required before an equivalent hydrogen experiment can be performed. The present antiproton detection scheme relies on the detection of energetic charged pions produced by antiproton annihilations. An alternative detection scheme for either hydrogen or protons is needed. Detection schemes of either hydrogen and protons have been internally discussed within the ALPHA Collaboration. One plausible scheme is to capture the photoionised products of hydrogen and direct them onto charge-sensitive detectors. However, attempts to capture an-

tiprotons from photoionised antihydrogen have not yet succeeded. An alternative detection scheme is to install photon detectors within the Penning trap to observe relaxation transitions. The current trap geometry is restrictive and, therefore, would have to be redesigned to be able to integrate photon detectors.

Secondly, the ALPHA apparatus lacks a proton source. Proton production is an ongoing consideration within the ALPHA Collaboration, in principle the antihydrogen production process could be charge conjugated to produce hydrogen. Those previously and currently developed methods are discussed later in Chapter 3. So far, studies of proton production have been restricted to external laboratories. This is in part due to a more modular approach, where a device would be adapted onto the current ALPHA apparatus and would provide low-energy protons on demand. As an alternative approach, this thesis will investigate a methodology for proton generation within the existing ALPHA apparatus.

Chapter 2, will discuss the apparatus, some theory, and techniques used in the development of this study. This will include the ALPHA apparatus in varying levels of detail and focussing more on the Catching Trap apparatus as it pertains to the later studies. The theory is split between Penning trap physics of the single particle regime and the plasma regime.

Chapter 3 considers what proton generation techniques are applicable within the ALPHA apparatus. The time scale of positive hydrogen ion losses by collisions with residual gas in the trap vacuum is estimated with some back of the envelope calculations. This time scale informs us how long to restrict the duration of total proton generation operations.

Chapter 4 describes the development of a positive hydrogen ion production scheme by electron impact ionisation, followed by tailoring methods to cool and compress the positive ion mixture using positrons. Positive hydrogen ion species are identified from time-of-flight measurements.

An autoresonance study is carried out with the objective of purifying the positive hydrogen ion mixture to a proton population. Chapter 5 describes an autoresonance study on the positive hydrogen ion mixture. This study aimed to determine a drive signal that removes all species besides protons. Some parameter scans of the drive signal are shown and analysed to obtain some insight into the performance of the autoresonance.

A brief disclaimer: I have become aware of a similar study within the ASACUSA Collaboration [39]. Similar positive ion generation was performed, and protons were obtained by removing secondary positive ions by manipulation of magnetron motions. The work presented here has been carried out from the Autumn of 2019 until the Autumn of 2020.

CHAPTER 2

THE ALPHA APPARATUS AND EXPERIMENTS

The synthesis, trapping and then study of antihydrogen requires a collection of systems. Both positrons and antiprotons need to be generated on-site, after which specialised charged particle traps are used to manipulate and combine them into a mixture. Antihydrogen is dominantly produced via a three-body recombination process, where two positrons scatter within a volume localised to an antiproton causing the remaining low energy positron and antiproton to bind. A combination of superconducting magnets traps a fraction of the formed antihydrogen. So far, all investigations of antihydrogen involve measuring its annihilation products which is performed with charge particle detectors. Spectroscopic investigations use microwave and/or laser systems to resonantly cause the anithydrogen atoms to leave the trap and annihilate. Gravitational investigations require increasing the complexity of the trap superconducting magnet geometry and improved control of the magnetic field within the trapping region.

The directionality along the apparatus is by ALPHA convention with respect to the central magnetic axis. The direction of travel towards the antiproton source is called 'upstream' and towards the positron accumulator is called 'downstream'. This convention for directionality will be used throughout this thesis.

The proton source study within this work is an *ad hoc* use of many systems intended for antihydrogen experiments. This chapter will detail the apparatus and some physics involved in this work.

2.1 The Penning-Malmberg Trap

It is necessary to confine antimatter within a vacuum using electromagnetic fields because contact with its matter counterpart (the apparatus surfaces) will result in loss by annihilation. Ion traps are devices designed to confine charged particles using electric fields, magnetic fields, or a combination of both. Currently, within ALPHA,

only Penning-Malmberg traps are used, which are a variation of the Penning trap. Penning-Malmberg traps can confine charged particles by employing a combination of hollow cylindrical electrodes and a solenoid magnet, as shown in Figure 2.1. DC voltages are applied to each electrode to create a U-shaped potential well, which confines particles along the centre axis of the electrode. At short distances from the electrode centre, the electric potential ϕ due to the electrode can be approximately described by a quadratic electrostatic potential:

$$\phi(x,y,z) = V_0 \left(2, z^2 - x^2 - y^2\right) / R^2 \tag{2.1}$$

Here, (x, y, z) is the position with respect to the centre of the electrode, and z is aligned with the centre axis of the electrode. V_0 is the electric potential of the electrode and R is the radius of the electrode

This radial repulsion from the centre of the electrode is overcome with a strong magnetic field directed parallel with the centre electrode axis. This magnetic field is produced by an external solenoid magnet that is orientated parallel to the electrode's axis. This combination of static electric and magnetic fields confines charged particles within the inner volume of the electrode.

In principle, all Penning traps operate using the same physics, although the geometry of the trap can be tailored to suit the purpose of the experiment. The Penning traps in ALPHA have electrode diameters of roughly 2 centimetres, and with cylindrical electrodes, this allows for a lot of freedom for transporting particles into and out of the traps' centre axis. Additionally, these traps have at least 8 electrodes to have greater control of positioning particles and to be able to store oppositely signed charged particles within the inner region of neighbouring electrodes. The lifetime of trapping requires the device to be under vacuum to reduce collisions with background gas that will cause scattering radially outward or annihilation. A high-quality vacuum of 10^{-13} mBar can sustain trapping on time scales of hours.

2.1.1 Single particle motion

The electric potential of a single electrode is a quadrupole potential, as described by Equation 2.1. When the electrode potential is biased correctly, a charged particle will be attracted to the electrode centre along the centre axis, z, and repelled radially outwards towards the electrode surface. This radial drift is modified by a uniform magnetic field produced by the external solenoid magnet.

A charged particle within a uniform magnetic field experiences the Lorentz force, causing it to move in a circular path known as cyclotron motion, illustrated in Figure 2.2 (a). In a Penning trap, the external solenoid magnet is orientated parallel to the electrode centre axis. The radius of this cyclotron motion is inversely proportional
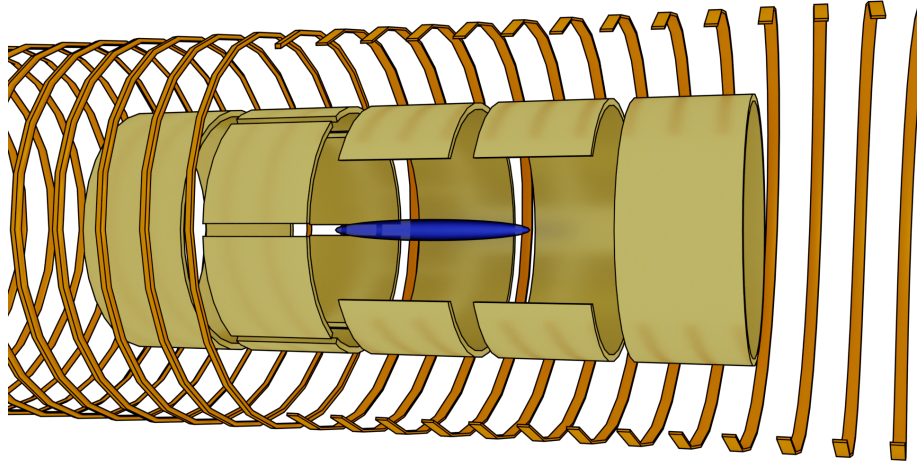
Figure 2.1: A cross sectional diagram of a Penning-Malmberg trap with four stacked hollow cylindrical electrodes and a single azimuthally segmented electrode, these are surrounded by an axisymmetric aligned solenoid magnet.

to the strength of the magnetic field. A strong magnetic field strength on the order of 1 T, is used to keep the cyclotron motion smaller than the radius of the electrode, which is 1 cm within this work, preventing collision with the surface. The magnetic force continuously turns the direction of motion either towards or away from the electrode surface. Additionally, the radius of this cyclotron motion is directly proportional to the speed of the particle.

Consider this cyclotron motion with the electric force of the electrode (directed radially outward), the speed of the particle increases when moving toward the surface and decreases when moving away. Consequently, the radius of the cyclotron motion grows when moving towards the electrode surface and shrinks when moving away. This motion causes the particle to drift azimuthally around the centre axis of the electrode. When the magnetic field strength is increased, the Lorentz force becomes stronger than the radial electric potential, resulting in the azimuthal motion of a charged particle forming a closed orbit around the centre axis of the electrode. This motion is called the magnetron motion, depicted in Figure 2.2 (c). The combined axial, magnetron, and cyclotron motions are shown in (d) as a red curve. The cyclotron, axial and magnetron motions are each described by their oscillation frequency: ω_c, ω_z and ω_m, respectively. These motions have a hierarchy condition:

$$\omega_c \gg \omega_z \gg \omega_m. \tag{2.2}$$

When this hierarchy is not satisfied the balance between the electric and magnetic fields that keep the charged particle confined becomes disturbed, leading to unstable particle motion. The Penning traps used by ALPHA are not hyperbolic geometries that produce ideal harmonic electric potentials, defined by Equation 2.1. Instead,
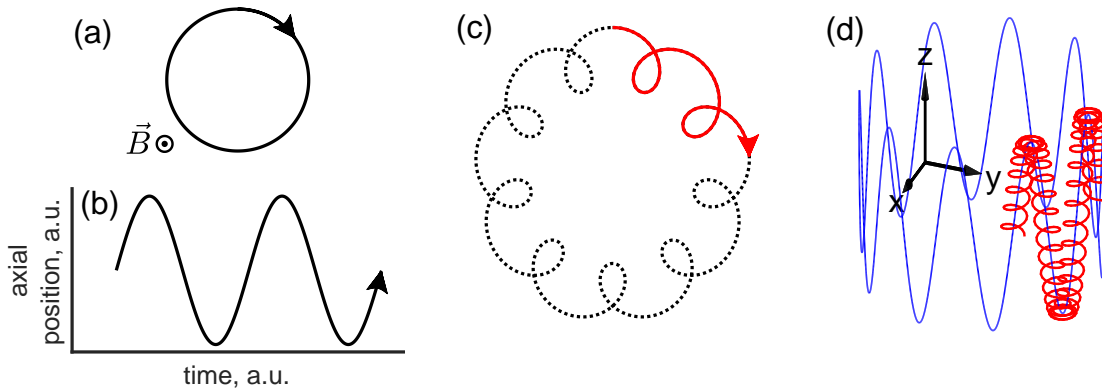
Figure 2.2: Periodic motion of particles within fields. (a) Cyclotron motion within a uniform magnetic field. (b) Axial motion (bounce) within the axial potential well. (c) A radial orbit from magnetron motion and fast cyclotron motion. (d) Full motion within a Penning trap.

the hollow cylindrical geometry produces a nonharmonic electric potential. The anharmonic electric potentials are U-shaped, suitable for trapping charge particles, though axial frequency changes are energy dependent. This non-ideal electrode geometry is used because the experiments in which ALPHA is interested are not single-particle motion studies. Instead, the traps are designed to trap large clouds of particles and plasmas, typically larger than 10^4 in population size. The motion of trapped particles within a non-ideal geometry does not greatly differ from what was mentioned before, though the motional frequencies will vary with the particle energy. This energy dependence allows methods such as autoresonance to be used, as discussed in Chapter 5.

2.1.2 Specialised traps

The ALPHA apparatus is composed of a number of Penning traps, each trap has a specialised role. The positron accumulator has electrodes with greatly different diameters. This geometry is used to create a constriction that causes a pressure differential across the trap to perform buffer gas cooling. The Catching trap has two high-voltage electrodes to trap an incoming antiproton bunch, whose energies are moderated by an adjacent metal foil. Both Penning traps in the ALPHA-2 atom trap and the ALPHA-g atom trap have aluminium electrodes nested in the middle of their electrode stacks that are thin, 1.5 mm thick wall and have inner diameters of 44.5 mm [40]. Thin electrodes reduce the material through which antiproton annihilation products need to travel to get to a detector. Larger diameter thin electrodes effectively increase the antihydrogen trap depth of the surrounding neutral atom trap, which is limited by annihilation on inner surfaces.

2.1.3 Positron Accumulator

The Positron Accumulator is a specialised system for trapping positrons. Positrons are produced by a radioactive sodium-22 source, see section 2.3.2. The source is mounted onto a coldhead to cool the source surface to 5 Kelvin. At this low temperature by injecting neon gas into the source's vacuum chamber a solid moderator film grows onto the source's surface, this moderator is intended to increase the number of positrons with energies below 80 eV such that a practical number can be captured by the trap. A neon moderator is used because in general it has the highest moderation efficiencies up to 0.5% [41, 42]. These positrons are magnetically guided by a series of solenoid magnets into what is called a Surko-type positron accumulator, see Fig. 2.3. This Surko-type Penning trap is composed of successively increasing
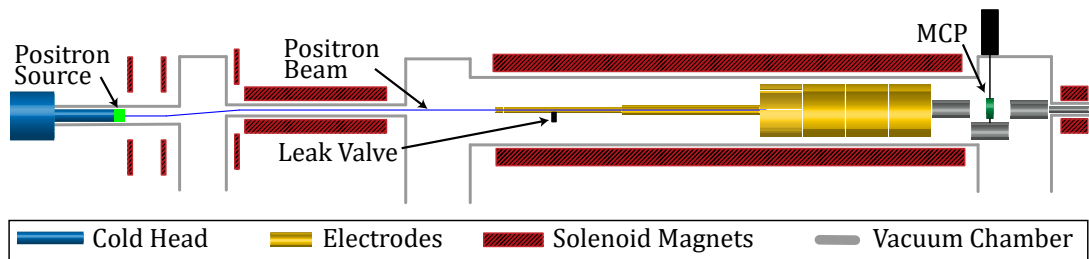
Figure 2.3: Schematic of the positron accumulator system at ALPHA. This system is composed of a sodium-22 which is the source of positrons. A system of magnetic guide to guide positrons into a Surko-type Penning trap. The trap is specialised to continuously accumulated positrons, by using the buffer gas cooling technique combined with radial compression using the rotating wall technique. The geometry of the electrodes produces a differential pressure of buffer gas (nitrogen) and varying electric potential across the trap essential for its operation, as shown in Figure 2.4. Adapted from [40].

diameter electrodes. With respect to the electrode's distance to the positron source, the first electrode is a 509.6 mm long, 12.7 mm internal diameter, tube, the second electrode is a 539.8 mm long, 30.5 mm diameter, electrode, and the further four separate electrodes are each 154.0 mm long and of 200.7 mm internal diameter [40]. A low-pressure nitrogen buffer gas is introduced, via a leak valve, into the narrowest electrode, causing a pressure gradient across the length of the entire trap. This buffer gas cools the positrons, causing them to be trapped within the Penning trap's confining electromagnetic fields. The trap electrodes are electrically biased such that as the positrons cool they accumulate towards a low pressure region of 3×10^{-6} mBar. A six-segmented electrode is used to radially compress the accumulated positrons. This buffer gas cooling process is illustrated in Figure 2.4. Before the positrons can be extracted from the trap, a valve to a turbomolecular pump is opened to remove the nitrogen gas. The positron accumulator has a dedicated multi-instrument stick with a MCP instrument and a pass-through electrode. Accumulated positrons can
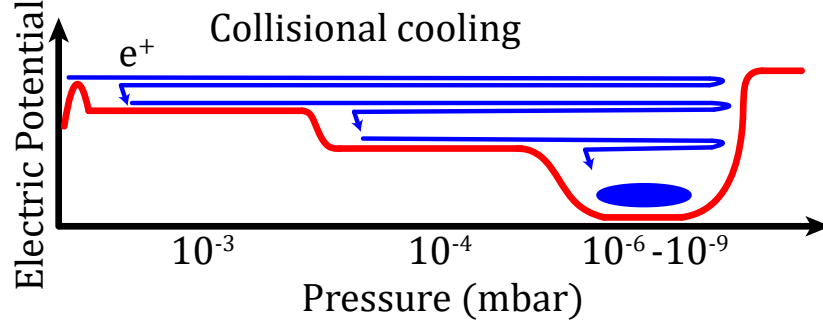
Figure 2.4: Positron collisional cooling in a pressure gradient of nitrogen gas. The horizontal axis corresponds to the pressure values along the axial length of the Surko-type trap. Pressure changes are due to changing diameters of electrodes. The on-axis electric potential (shown as a red line) produced by the electrodes has an increasing well depth with decreasing buffer gas pressure. A positron beam is depicted as losing kinetic energy via collisions with buffer gas. The configuration of electric potentials causes that for decreasing kinetic energies the axial motion of positions become constrained to the lower pressure regions. The positrons will accumulate to the lowest pressure region forming a cloud. Adapted from [40].

be diagnosed by ejecting them onto the MCP instrument or magnetically guided to other traps by moving the stick to the pass through electrode before ejection.

2.1.4   The Atom Trap

ALPHA-2 is designed to trap both charged particles and neutral atoms. It combines a Penning-Malmberg trap with an Ioffe-Pritchard trap (for neutral atoms) in such a way that their trapping volumes overlap. The cross section of this configuration is illustrated in Figure 2.5.

A neutral atom has a magnetic moment vector, denoted as $\vec{\mu}$, which can interact with an external magnetic field, represented by $\vec{B}$. The interaction between these vectors results in a magnetic potential $U(\vec{x})$, defined by:

$$U(\vec{x}) = -\vec{\mu} \times \vec{B}. \qquad (2.3)$$

If a neutral atom moves slowly enough, its magnetic moment will exhibit adiabatic behaviour. Similarly, if the external magnetic field vector changes at a slow rate compared to the magnetic moment's precession time scale, the neutral atom's magnetic moment will behave adiabatically. For ground-state antihydrogen, the positron magnetic moment dominates its magnetic properties. The magnetic moment of the positron can align parallel $(+)$ or antiparallel $(-)$ with the external magnetic field. The two alignments result in distinct magnetic potentials:

$$U(\vec{x})_{\pm} \simeq \mp\mu_{\mathrm{B}}|\vec{B}|, \qquad (2.4)$$

13

Here, $\pm$ indicates the direction of alignment, and the magnitude of the positron magnetic moment is approximately equal to a Bohr magneton, μ_{B}. This expression for the potential highlights two opposing dynamics: trajectories toward magnetic field strength maxima, referred to as "high field seeker", and trajectories towards minima, called "low field seeker". The "high field seeker" and "low field seeker" states correspond to the parallel and antiparallel intrinsic spin states, respectively.

The Ioffe-Pritchard trap, also known as the neutral trap, is a three-dimensional magnetic trap featuring a magnetic minimum at its centre, which effectively traps "low field seeker" atoms. The trap's field shape is generated by the combination of multiple superconducting solenoids that create axial magnetic gradients along the electrode stack's axis, and a superconducting octupole that produces a radial magnetic gradient centred on the electrode stack's axis. The octupole consists of a serpentine winding pattern that runs repeatedly along the length of the ultra-high vacuum (UHV) pipe and alternates the turn direction at each coil end. It is made up of eight layers, each offset by 45 degrees azimuthally in relation to the previous layer. The polarity of the octupole magnetic field oscillates azimuthally around the central axis, but the trapping mechanism is not influenced by the field's polarity. A surrounding solenoid magnet is essential for the neutral atom trap, as it prevents the existence of null magnetic field regions within the trapping volume. Without it, an antihydrogen atom could undergo a Majorana transition (spin flip) and be ejected from the trap. For a more complete understanding of neutral atom traps, refer to [43].

A cross section of the ALPHA-2 Ioffe-Pritchard trap is shown in Figure 2.5. A Penning-Malmberg superconducting solenoid magnet surrounds the components, producing a uniform 1 T magnetic field within the innermost cylindrical electrodes. The outermost component shown is a three-layered cylindrical silicon vertex detector for measuring antiproton annihilation products. Moving radially inward, the Ioffe-Pritchard trap's superconducting magnets are centred on the electrode stack, creating the magnetic minimum region for trapping neutral antihydrogen. Within this, a one-meter stack of cylindrical electrodes manipulates plasmas to form antihydrogen. Windows at both ends of ALPHA-2 serve as laser access ports for directing laser light into the neutral atom trap region. Enclosed by boxes with platforms for mounting optics and detectors, the Ioffe-Pritchard trap consists of one octupole, two long solenoids at each end of the octupole, and five short solenoids (mirrors) evenly distributed along the interior axial length. These mirrors help to tailor the axial magnetic field gradient, which can be used for cooling via adiabatic expansion of the trap length.
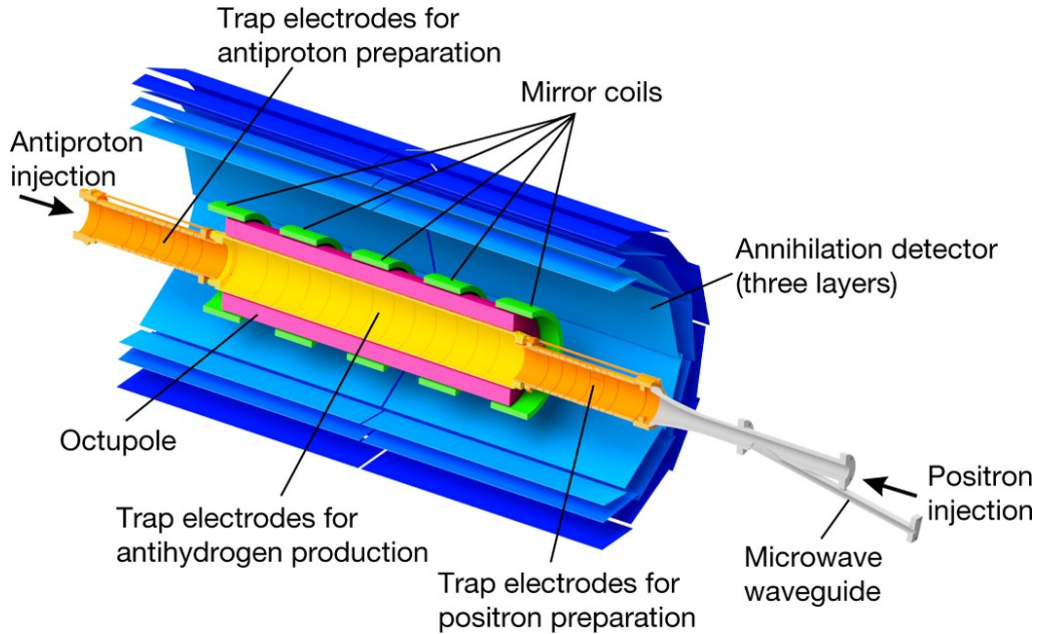
Figure 2.5: This cross section schematic shows the antihydrogen production and trapping region of ALPHA-2. The vacuum wall and the cryostat for the superconducting magnets are not shown. All of the components shown are immersed in a uniform, 1 T, axial magnetic field, provided by an external solenoid (not shown). Adapted from [44].

2.1.5 The Catching Trap

The antiproton catching trap, shown in Figure 2.6, is specifically designed to capture and tailor antiprotons from the AD beamline before transferring them to one of the two antihydrogen synthesis and trapping apparatuses, ALPHA-2 or ALPHA-g. The majority of the positive hydrogen ion work described in this thesis was carried out using this machine (refer to chapters 4 and 5). This cryogenic Penning-Malmberg trap features a uniform 3 T magnetic field generated by a cryocooled superconducting solenoid. The electrode stack consists of 20 hollow cylindrical electrodes with inner diameters of 29.6 mm and a total length of 396 mm, as shown in Figure 2.7. These electrodes are cryocooled to temperatures between 4 and 7 K using a helium cryogenic cooler. The incoming antiproton bunches from AD have an energy of 5.3 MeV, which is too high to be efficiently trapped using only a Penning trap. A thin metal foil is placed in the path of the antiproton bunches to reduce the energy via inelastic scattering. However, numerous antiprotons will annihilate and scatter onto untrappable trajectories. The thin metal foil also serves as the interface between the Catching Trap and the AD vacuums. The electrode closest to the AD interface and another electrode located approximately halfway along the stack are specialised high-voltage electrodes used for capturing antiprotons. The capture process is similar to that shown for positrons in Figure 4.8, with the exception that electrons are nested within the Penning trap electric potential to assist in capturing and cooling
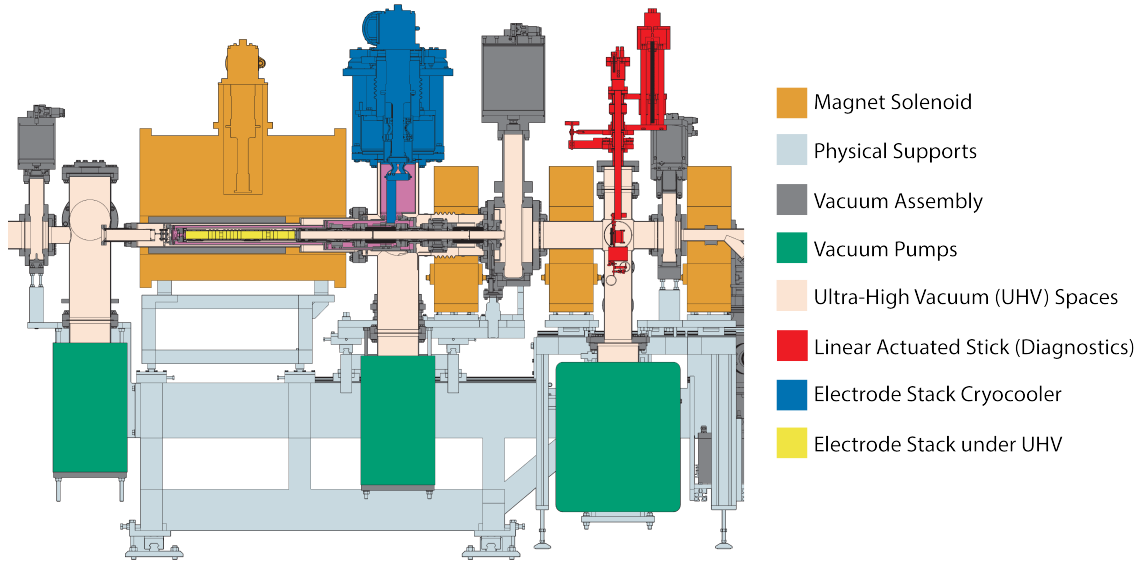
Figure 2.6: Labelled schematic of the experimental apparatus called the Catching Trap. Adapted from [45].
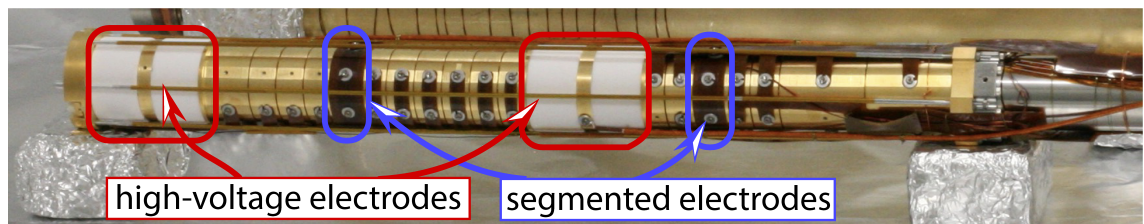
Figure 2.7: The catching trap electrode stack assembly. Image from the ALPHA Collaboration.

antiprotons, and the electric potentials used for capturing antiprotons are operated at high voltages. The Penning trap is divided into two halves by a high-voltage electrode. Each half has a single azimuthally segmented electrode, each containing six segments, for rotating wall compression, which will be discussed later. Each electrode is connected to a ± 140 V DC power supply with 16-bit digital to analogue control, providing a resolution of 4 mV. During antiproton studies, the high-voltage electrodes are operated at approximately 5 kV DC. Each electrode has a filter board connected to its feedthrough. These boards feature two parallel inputs to a single electrode, one with a low-pass filter and the other with a high-pass filter, with cutoff frequencies of 25 kHz and 170 kHz, respectively. This design helps to reduce environmental electrical noise on the electrodes, as the apparatus is within the centre of the Antiproton Decelerator ring and neighbouring other user experiments.

2.1.6 Multi-instrument stick

Diagnostic measurements in the ALPHA apparatus are primarily conducted using vertically stacked instruments housed within an adjustable bellow. This bellow can

be compressed and expanded by an external linear actuator. The combination of stacked instruments and adjustable bellows is known as a "stick" [46]. The Catching Trap stick is coloured red in Figure 2.6. Sticks are typically positioned next to the main solenoid magnets of all ALPHA Penning traps and are integrated into ultra-high vacuum (UHV) systems and magnetic beamlines, as discussed in Section 2.6. Each stick features an electron gun (described in Section 2.3.1) and a Multi-Channel-Plate (MCP) phosphor screen instrument (explained in Section 2.5.2). Additional instruments are chosen on each stick according to the specific function of the corresponding Penning trap.

This work uses two sticks: the Catching Trap stick (illustrated in Figure 2.6) and the downstream Atom Trap Stick. The vertical position of the linear actuator can be adjusted to align one of the various instruments with the central magnetic field lines of the adjacent Penning trap. Electrons are routinely captured within the Catching Trap to aid in antiproton capture. When the electron gun instrument is aligned (see Section 2.3.1 for more information) with the central field lines, electrons can be injected from the instrument into the Penning trap. Alternatively, charged particles can be ejected from a Penning trap onto one of the aligned detectors, such as an MCP-phosphor or Faraday cup.

2.1.7 Programmable experiments

ALPHA designed Penning traps and other systems to be digitally controlled using computers, typically using LabVIEW software. Manipulation of the voltages applied to individual electrodes in the Penning traps is carried out using PXI hardware from National Instruments. This hardware can sequentially output analogue voltages that are synchronously timed with the hardware's integrated clock. A custom LabVIEW project acts as front-end software, allowing users to programmatically write experimental procedures in a sequential manner. These files are internally known as "sequences".

Within this environment, macros have been created to perform routine procedures, such as moving the MCP-phosphor instrument into view of the Penning trap, waiting for the stick to stop moving, adjusting the applied voltages on the MCP-phosphor instrument, and finally waiting until the power supply output voltages have reached and stabilised at the target values. Another type of macro is used for adjusting the trap electrodes' voltages, which is key for manipulating trapped particles. This macro generates a set of voltages to be applied to each electrode, with a target voltage for each electrode, as well as the number of voltage steps and the total duration to reach the target voltage.

A typical plasma in ALPHA experiments can be transported to another axial region of the Penning trap by using a large number of voltage steps. Depending on the

plasma's characteristics and composition, this manipulation can involve using thousands of steps and can occur over time scales larger than 1 ms to avoid heating the plasma and being axially stretched and compressed. This combination of software and hardware is collectively referred to as the "sequencer".

2.2   Non-Neutral Plasma Physics

Naturally, as more charged particles are added to a well in a Penning trap, the dynamics of the particles transitions from single-particle motion to correlated motion, resulting in macroscopic behaviour. A cold and dense collection of charged particles behaves as a plasma. Plasma is commonly found in various forms, such as fire, lightning storms, auroras, and stars. Due to the trapping nature, the plasma within Penning traps consists of a single sign charge and is referred to as non-neutral plasma.

When an external electric field is applied to a plasma, a charge flow is induced until the electric field is screened inside the plasma. We will use the definition of a plasma from [47] (Chapter nine). A plasma of length L has a shorter screening length scale, known as the Debye length λ_D. Furthermore, changes in plasma density n_0 are small on the screening length scales. This can be more concisely expressed as follows:

1. $\lambda_D \ll L$

2. $\lambda_D \gg a \equiv n_0^{-1/3}$,

where a is the mean inter-particle spacing. For the second condition to be satisfied, any volume λ_D^3 within the plasma should contain many particles, ensuring sufficient particle flow for screening. A collection of particles are considered plasma if they satisfy these two conditions.

In a plasma with equilibrium density and temperature, the Debye length (λ_D) is defined as follows:

$$\lambda_D = \sqrt{\frac{\varepsilon_0 k_B T}{n_0 q^2}}, \tag{2.5}$$

Here, ε_0 is the electric permittivity of free space, k_B is Boltzmann constant, T is the plasma temperature and q is the unit electric charge. The Debye length represents the distance over which an externally applied electric field decreases by $1 - 1/e \approx 63.2\%$.

The shielding response time of the plasma is limited by the average velocity of the particles, $\sqrt{2k_B T/m}$, and the length scale of the shielding, λ_D. If an external electric field oscillates faster than this response time, the particles will not exhibit plasma-like behaviour. The plasma response time (τ_p) and its reciprocal, the plasma

frequency (ω_p), are:

$$\omega_p = \frac{1}{\tau_p} = \sqrt{\frac{2k_BT}{m}}\frac{1}{2\lambda_D} \tag{2.6}$$

$$= \sqrt{\frac{n_0q^2}{m\varepsilon_0}}. \tag{2.7}$$

Unlike the Debye length, the plasma frequency depends on the species mass. For a plasma to reach thermal equilibrium, it must equilibrate across all degrees of freedom. This can occur through collisions with large scattering angles. The rate of such scattering determines the thermalisation time scale and informs on what time scale the plasma can be considered to be in thermal equilibrium. The collisional equipartition rate ($\nu_{\perp\parallel}$), as given in Glinsky (1992) [48], is:

$$\nu_{\perp\parallel} = n_0\bar{v}(2b)^2 I(\bar{\kappa}), \tag{2.8}$$

where the magnetisation parameter, $\bar{\kappa} = \sqrt{2}b/r_c$, the distance of closest approach, $b = q^2/(4\pi\epsilon_0 k_BT)$, and the average thermal speed, $\bar{v} = \sqrt{2k_BT/m}$. The Coulomb logarithm, $I(\bar{\kappa})$, has an asymptotic expression for a nonmagnetised plasma (that is, when $\bar{\kappa} \ll 1$):

$$I(\bar{\kappa}) = -\frac{\sqrt{2\pi}}{15}\ln\left(0.333 \times \bar{\kappa}\right) \tag{2.9}$$

In order for the motion of particles within a plasma to be primarily influenced by external magnetic and electric fields, the collisional rate must be significantly slower than the plasma frequency, i.e., $\nu_{\perp\parallel} \ll \omega_p$.

The plasma physics discussed so far pertains to single-species plasmas. This plasma theory will be loosely applied, disregarding interspecies interactions, as much of the subsequent work involves mixed plasmas that contain up to four species.

Consider, for example, a 1500 K positive hydrogen ion plasma prepared in Chapter 4 and studied in Chapter 5. This plasma contains 3 million ions with an average density of 1.1×10^8 cm^{-3}. Comprised of protons, H$_2^+$ ions, and H$_3^+$ ions, its characteristic plasma parameters are $\omega_p = $ [13 MHz, 9 MHz, 8 MHz], $\lambda_D = 0.27$ mm, and $\nu\perp\parallel = $ [320 Hz, 240 Hz, 200 Hz] for [H$^+$, H$_2^+$, H$_3^+$], respectively. The perturbation to interspecies scattering simply involves a weight factor containing a reduced mass factor, which is less than an order of magnitude for hydrogen ion scattering.

2.2.1 The rotating wall technique

The dynamics of radial trapping within a Penning trap is delicate. Collisions and azimuthal symmetry breaking can result in radial transport and particle loss. This loss process can be counteracted using the rotating wall technique for plasma, as

described by Huang *et al.* [49]. The axialization technique is used for a collection of trapped particles that are not a plasma. In this discussion, only the dynamics within the plasma regime will be considered.

Magnetron motion, previously mentioned in the single particle regime, appears as a bulk rotation in the plasma regime. Plasma within a Penning trap assumes a spheroidal shape with varying aspect ratios. To gain insight into the bulk rotational dynamics, a highly prolate shape can be considered, which can be approximated as a rotating cylinder of plasma. Assume that a plasma cylinder has length L and radius r_p, with uniform density n. In the limit where L is much larger than r_p, the radial electric field E_r produced by the plasma is given by:

$$E_r = \frac{nqr}{2\varepsilon_0}. \tag{2.10}$$

A plasma inside a uniform magnetic field B, aligned with the cylindrical axis, undergoes an azimuthal $\vec{E} \times \vec{B}$ drift, resulting in a rotation f_E around the plasma's radial centre. The rotation frequency f_E is calculated as:

$$f_E = \frac{E_r}{2\pi r B} \tag{2.11}$$
$$= \frac{nq}{4\pi\varepsilon_0 B}, \tag{2.12}$$

where the second line uses Equation 2.10. Note that this rotation frequency does not vary across the radius of the cylinder, indicating rigid body rotation. Implying that applying an external torque on the plasma to adjust its rotational frequency also controls its radial distribution, i.e., the plasma density.

The rotating wall technique compresses a plasma using an external electric dipole centred and rotating around the plasma symmetry axis. The plasma is offset from the electric dipole, ensuring that only one end of the plasma is exposed, as shown in Figure 2.8 (a). The dipole rotation frequency is chosen to couple with the plasma through plasma modes. The coupling can occur with non-rotational modes, resulting in heating and requiring a cooling mechanism, as increasing temperatures reduce the coupling strength to the rotating dipole. The ALPHA apparatus uses six-segmented electrodes to produce this azimuthally rotating electric dipole. A sinusoidally oscillating signal is applied to each electrode with a phase offset of $\pi/3$ to each electrode segment, see Figure 2.8 (c). The electric potential of the *jth* segment $\phi_j(\theta, t)$ is

$$\phi_j(\theta, t) = V_{\mathrm{RW}} \cos\left(\theta_j - 2\pi f_{\mathrm{RW}} t\right), \tag{2.13}$$
$$\theta_j - \frac{\pi}{6} < \theta < \theta_j + \frac{\pi}{6}; \tag{2.14}$$

where θ is the azimuthal angle, V_{RW} is the dipole amplitude, and f_{RW} is the rotational frequency of the dipole. The vacuum electric potential within the segmented

electrode is shown in Figure 2.8 (d).
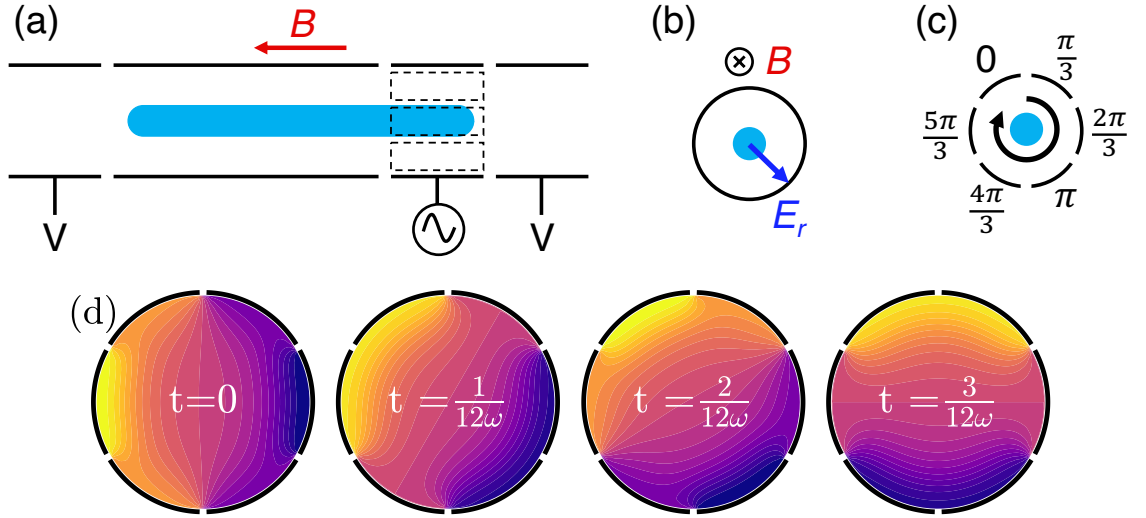
Figure 2.8: Schematic diagrams of segmented electrodes for the rotating wall technique, adapted from Chapter 11 of [47]. Rotating vacuum dipole mode electric potentials of segmented electrodes with phase steps $\pi/6$ are also shown. Yellow and blue indicate positive and negative electric potentials, respectively.

2.2.2 Electron kick

In a Penning trap, electric potential wells separate particles of a single electric charge sign, allowing the trapping of either positive or negatively charged particles. Mixing negatively charged particles with electrons or positively charged particles with positrons allows for useful tailoring methods, such as sympathetic cooling. The temperature of trapped ions in a Penning trap can be critical for certain studies, but the cooling mechanisms within the system are limited.

The cyclotron radiative cooling rate for ions in strong magnetic fields created in the lab exceeds practical time scales, taking more than tens of years. However, the cyclotron cooling time scales for electrons and positrons in a 3 T magnetic field are much shorter, in the subsecond range. When positrons are mixed with positively charged ions, the ions can transfer energy to the positrons through collisions, which the positrons then radiate.

In a thermal equilibrium mixture, leptons have the fastest motion speeds and respond more quickly to changes in the trapping electric potential than other mixture components. By manipulating the trapping potential on time scales shorter than the axial motion of the ions, the leptons can be guided out of the well. In practise, this is achieved by applying an electrical pulse with a duration of 40 ns to 100 ns and an amplitude greater than the depth of the well to one of the two electrode potential barriers, rather than the inner well electrodes, and with a positive potential well

minimum to ensure particle ejection.

To avoid ion heating when a significant amount of lepton charge is removed with a single pulse, multiple pulses of increasing amplitude can be used to remove fractional amounts of the total lepton population, ultimately eliminating the remaining population. The mixture is held between these pulses to allow it to equilibrate and for the remaining lepton population to provide additional cooling.

This method is used to remove electrons after capturing and cooling antiprotons. Because antiprotons are mixed with positrons to form antihydrogen, the presence of electrons could lead to loss of positrons through annihilation and formation of positronium. This technique is also used later in this work to remove positrons from a mixture of positive ions, as positrons within a positive ion mixture were found to shield the entire plasma mixture from external axial electric drives.

2.3 Particle Sources

2.3.1 Electrons

Thermionic electrons are generated by a heated barium oxide filament, which is attached to the multi-instrument stick (see Section 2.1.6). The emitted electron current is regulated by the filament current and a potential difference between the filament and a biased plate. These electrons are accelerated to 21 eV and collimated through a small hole in an acceleration plate, creating an electron beam that when suitably aligned can be effectively transported into a Penning-Malmberg trap. The vertical position of the stick is adjusted to ensure that the electron beam aligns with the Penning-Malmberg trap axis, as it is guided by a magnetic beamline and the trap solenoid magnet.

Electrons are captured within trapping electric potentials using a method called
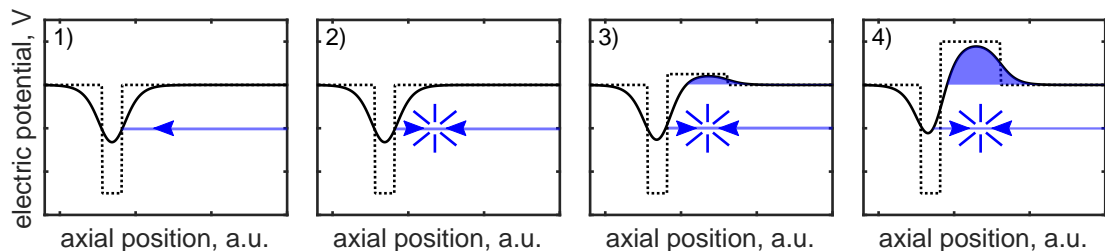
Figure 2.9: Simplified diagram of electron capture. The blue fill and the lines represent electrons, dashed black lines denote the applied electrode potentials, and solid black lines illustrate on-axis electric potentials.

"suck load" (see Figure 2.9). In this process, a blocking potential reflects the electron beam back onto itself [steps 1-2], resulting in the scattering of ingoing and outgoing electrons within a potential minimum. Electrons with excess energy will escape,

leaving the remaining electrons trapped in the potential well [step 3]. This continuous process is carried out over several seconds as the depth of the well increases until the desired number of electrons, ranging from 10^5 to 10^9, is trapped [step 4].

2.3.2 Positrons

Positrons can be obtained as a decay product from the sodium-22 isotope, $^{22}_{11}$Na. 90.26(2)% of this isotope decays through the Beta positive decay mode, as shown in the following equation [50, 51]:

$$^{22}_{11}\text{Na} \rightarrow {}^{22}_{10}\text{Ne} + e^+ + \nu_e \qquad (2.15)$$

Both neon-22 and the electron-neutrino are stable and neutrally charged particles, which weakly interact with the electrically charged positron. Sodium-22 has a half-life of 950.34(13) days [52], so a sample with an initially useful amount of radioactivity can provide approximately the same positron flux for extended operational periods, on the order of years. The simple decay modes, the stable daughter isotope, the radioactivity, and the availability of manufacturing make sodium-22 an appealing candidate as a positron source in experimental physics. Other beta-positive decaying isotopes, such as cobalt-58 and copper-64, can be manufactured, although these have much shorter half-lives.

Alternatively, positrons can be produced using a linear electron accelerator with specialised generation materials to enhance the production of bremsstrahlung light and subsequently facilitate the pair production of electron-positron pairs. In theory, such a machine can operate for extended periods and produce a high-intensity positron beam. However, in the context of the ALPHA experiment, such an intense source has not yet been needed.

2.3.3 Antiprotons

The Antiproton Decelerator (AD) currently serves as the only global source of low-energy antiprotons, with energies around 5.3 MeV. The AD relies on proton bunches accelerated by the LHC proton accelerator complex, which includes LINAC2 and the Proton Synchrotron. Through 25 GeV relativistic proton collisions, proton-antiproton pairs are generated. These antiprotons are then collected and shaped into 2.7 GeV bunches, before being injected into a magnetic storage ring known as the AD.

Once the antiprotons enter the AD ring, a process of beam tailoring and cooling begins. This procedure results in antiproton energies as low as 5.3 MeV, at which point the antiproton bunch is injected from the AD ring into an experimental user area. Each bunch has a temporal length of 200 ns and contains 3×10^7 antiprotons.

2.4 Cooling techniques within a Penning trap

There are a variety of cooling techniques for trapped plasma. Direct cooling techniques include laser cooling, resistive cooling, adiabatic cooling, evaporative cooling and radiative cooling.

Laser cooling requires an atomic electron configuration that has an electron manifold with a closed cycle, of course this is not applicable to the proton.

Resistive cooling can be achieved passively or actively, both will involve integrating a charge sensing circuit across the trapping electrodes, where the axial motion of a trapped charge particle acts as an image current source. In passive resistive cooling this image current is dissipated in the sensing circuit's resistance, while in active resistive cooling the sensed image current is fed back to the electrodes in an opposite phase, acting to drive against the motion of the charged particle. Practical cooling times require a resonant circuit, which leads naturally to charge-to-mass selective cooling. Resistive cooling is used throughout many Penning trap proton studies [25]. By increasing the trapping volume size at a rate much slower than the axial, magnetron and cyclotron motions of the charged particles, thereby it being an adiabatic process, the motional energies of the particles can be reduced, this is referred to as adiabatic cooling. This effect can be achieved by changing either the trapping electric potential or changing the magnetic field as shown in ref. [53].

When a plasma is in thermal equilibrium it has a Maxwellian-like energy distribution. This exhibits a long energy tail, where at any given time relatively few particles can be associated with a substantial amount of the total thermal energy. By reducing the trap electric potential depth these higher energy particles can be removed, thereby reducing the average energy of the remaining population. This process is referred to as evaporative cooling.

The acceleration undergone by a charged particle in a Penning trap generates cyclotron radiation, though due to the power emission being inversely proportional to the mass cubed, practical cooling times occur only for light particles, most commonly either electrons or positrons.

Additionally, there are indirect cooling techniques where a secondary species is cooled, possibly by one of the previously described direct cooling techniques, and is simultaneously or later allowed to interact with the concerned primary plasma. This is referred to as sympathetic cooling. Another method in this category, previously discussed in Section 2.1.3, is buffer gas cooling.

2.4.1 Axialization

During a cooling process both the modified cyclotron motion and axial motion will be reduced. However, during cooling processes the magnetron motion increases in

magnitude, since the magnetron motion has negative potential energy, leading to magnetron heating. In the 1991 Savard *et al.* paper [54], a technique is described for both centering and cooling ions in a mass selective manner. This is done by a combination of buffer gas cooling (leaked in helium gas at a pressures of 10^{-4} mBar) and an azimuthally applied RF quadrupolar field, driven in autoresonance with the species' cyclotron motion. The buffer gas provides cooling to both the cyclotron and axial motion, though it is a source of heating for the magnetron motion. A blue sideband coupling is performed on the modified cyclotron motion and the magnetron motion. This motional coupling allows for the cooling to be applied to magnetron motion. By reducing the magnetron motion the particle gradually drifts towards the trap central axis. For this to be applicable in the ALPHA Catching Trap apparatus RF quadrupolar fields of an appropriate frequency needs to be injected on to the segmented electrodes.

In later literature this technique, for centralising the motion of the trapped ions onto the central axis, has been referred to as axialization and sideband cooling. An analogue laser cooling technique was first demonstrated by Powell et al. 2002 [55].

2.5 Charge Detection

2.5.1 Faraday cup

A Faraday cup is an instrument used to collect and measure electric charge by recording the potential difference between a charge-collecting surface and an electrical ground. The collecting surface is connected to the ground through a resistor, allowing it to discharge and be used to measure successive groups of charged particles. In this thesis, two instruments serve as Faraday cups: the first is the antiproton degrader foil exposed to the interior of the Catching Trap and the second is the phosphor surface within the MCP-phosphor instrument. The phosphor surface is coated with a thin layer of indium tin oxide to serve as a transparent conductive layer.

The degrader foil is an electrically isolated metal conductor connected to an external readout circuit. The electrical behaviour of this circuit is similar to an ideal capacitor connected to a ground potential through a resistor. When charged particles strike the foil's surface, its electric potential increases and then gradually decays exponentially to its referenced ground potential as the surface discharges. This signal passes through a shielded BNC cable to an amplifier and noise filtering device, the Stanford Research Systems SR560 low noise voltage preamplifier, and is finally read by a data acquisition PCI card. High-pass and low-pass filters help remove background electrical noise, and the amplifier gain is tuned to maximise the signal-to-noise ratio.

Assuming that the circuit is purely capacitive, it can easily be modelled and under-
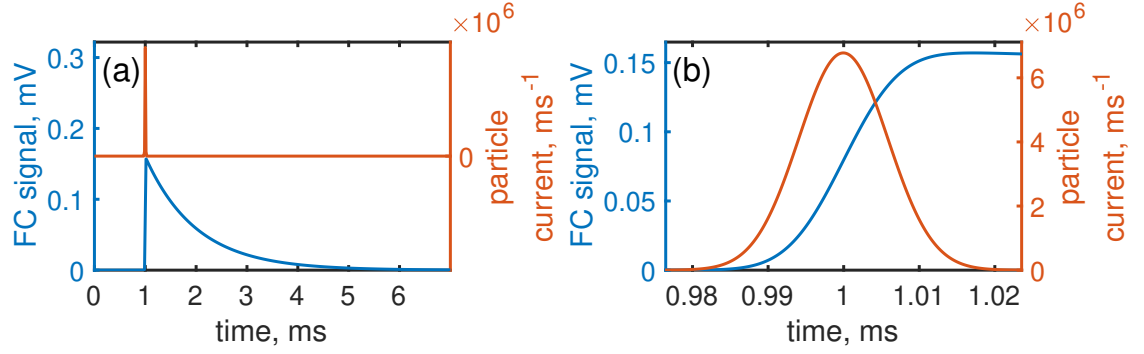
Figure 2.10: Example of Faraday cup readout with particle flux. Orange lines: particle flux over time, Blue lines: solution of Equation 2.16 for voltage difference readout. (a) A 7 ms window of the signal, displaying the exponential decay. (b) A zoomed-in window, illustrating the temporal distribution of charged particles and the voltage rise on the Faraday cup.

stood through the following first-order differential equation:

$$\frac{dV}{dt} + \frac{1}{\tau}V(t) = G\frac{Q_{flux}(t)}{C}, \tag{2.16}$$

where t represents time and V denotes the voltage difference relative to the reference ground. The second term on the left-hand side is a voltage difference damping term with a characteristic decay time of $\tau = RC$ for a circuit with capacitance C and electrical resistance R between the charge collection surface and the reference ground. The term on the right-hand side is the voltage difference source term, where $Q_{flux}(t)$ is the charged particle flux arriving at the foil's surface, and G is the amplifier gain factor applied to the signal. When the characteristic decay time τ is significantly greater than the time scale of all particles arriving at the surface, the potential difference between the peak voltage and the ground reference is related to the total number of particles. This is a valid approximation for all Faraday cup measurements used throughout this thesis, as the decay time of these circuits is empirically about 1 ms and the particles arrive in a time interval of approximately 10 μs. The MCP phosphor screen, when used as a Faraday cup, requires a high-pass pick-off circuit in parallel with the high-voltage circuit of the phosphor screen to protect and operate the readout hardware. This device is much more sensitive to the quantity of charged particles arriving from the Penning trap than the antiproton degrader foil, as the charge signal is amplified by an electron avalanche inside the MCP. This instrument enables quantitative measurements of small particle fluxes, such as timing information, and is used for temperature diagnostics (see Section 2.5.2) and time-of-flight measurements.

To recover the original qualitative particle flux, a basic signal analysis method called impulse response can be employed. An impulse response function can be generated by analysing the circuit's response to a known input impulse signal. An input

impulse signal is a pulse with a short duration time compared to any characteristic time scale of the circuit. The impulse response function maps the readout circuit's frequency components to the input signal's frequency components, as discussed in Section 5.6.

2.5.2 Micro-channel Plate - Phosphor - CCD

The micro-channel plate (MCP), phosphor, and CCD (charge-coupling device) setup is a series of interconnected devices used to image the radial profile of plasma extracted from a Penning trap. The MCP consists of an array of microscopic channels angled away from the plate's symmetry axis. A high voltage is applied between the front and back of the plate, and the front plate power supply generates both positive and negative voltages relative to the ground. The polarity of the front plate voltage is selected based on the charge of the particles to be measured, accelerating them towards the surface. As incoming charged particles have a relatively large longitudinal-to-radial velocity, they primarily move normally incident to the front of the plate. When a charged particle enters one of the angled channels, its motion is obstructed, leading to collisions with the channel's interior surface and the production of secondary electrons. This process triggers an avalanche of electron production, amplifying the original plasma signal. The gain can be controlled by adjusting the voltage difference across the front and back of the micro-channel plate. The applied voltage difference between the front and back of the plate is positive, and only negatively charged particles will pass entirely through the channels. Consequently, the resulting collection of charged particles consists primarily of electrons and possibly any negatively charged particles that initially enter the channels. After exiting the channels, these particles are further accelerated by a larger voltage difference toward a phosphor screen. Phosphorescent light is emitted when energetic charged particles collide with the screen.

The phosphor screen faces the beamline direction, and to extract light, an adjacent mirror positioned at an angle of $\pi/4$ radians relative to the screen reflects light towards a vacuum window. A CCD imaging camera is externally mounted on the window to capture the light.

The resulting image is proportional to the radial profile of the axially integrated plasma signal. Knowing the magnetic field strength ratio at the plasma extraction position in the Penning trap and at the MCP, the size of the plasma can be calculated, assuming that the magnetic moment of the charged particles in the plasma is conserved during extraction.

Plasma image analysis

Plasmas trapped within ALPHA Penning traps typically exhibit axisymmetry, as non-axisymmetric modes are not intentionally excited. For single species plasmas imaged using the MCP, this symmetry is expected to be maintained. While this is observed for lighter components like electrons and positrons, heavier ion species often appear as ellipses or exhibit further distortion in their shape. This distortion is believed to result from a combination of the nonadiabatic magnetic moment dynamics of particles transported along the magnetic beamline, to which heavier ions are more sensitive, causing radial expansion, and the increasing nonhomogeneity of the electric potential at the front surface of the MCP with greater radial distances from its centre, which distorts the shape of the heavier ion plasma.

Plasma radius is determined from the MCP image using an empirically justified radial fit function of the camera pixel light intensity $I(r)$, a Gaussian-Power law fit defined as:

$$I(r) = a \exp\left(- \left[\frac{r - r_0}{b} \right]^n \right) + \text{Background Level,} \tag{2.17}$$

where we have a mean noise background light level in the image, the position of the plasma central symmetry axis r_0, the peak amplitude of the plasma centre a (minus the mean noise background level), the plasma radius b (the radial position where the light intensity decreases to $1/e$ of the peak intensity), and the Gaussian power n that flattens the profile curvature. For multicomponent plasmas exhibiting centrifugal separation, see Appendix B. An image of the phosphor screen can be captured with the same camera under brighter conditions to identify features of the MCP assembly. This enables measurement of the imaged plasma size with reference to the known dimensions of the phosphor screen.

Furthermore, if the plasma is transported adiabatically, as discussed in Section 2.6, the radial size of the plasma within the Penning trap can be estimated. By multiplying its size on the MCP surface, taken from the MCP image, by the ratio of the magnetic field strength at the MCP instrument and inside the Penning trap, which is approximately 0.15. For example, if a plasma ejected on to the Catching Trap MCP is measured to have a plasma radius of 1 cm across the MCP surface, then its radius within the Catching Trap is approximately 0.15 cm.

Temperature diagnostic

The temperature of a plasma affects its dynamics, which can lead to undesirable effects. For example, when mixing positrons and antiprotons, their temperatures influence both the efficiency of antihydrogen production and trapping. Additionally, a hot plasma may promote radial transport outward, resulting in particle loss. Therefore, monitoring plasma temperature changes during a sequence can indicate

whether adjustments should be made. Instead of passive monitoring, a destructive but robust method is employed within ALPHA. Assuming that a plasma is in thermal equilibrium, such that both axial and radial components of the plasma temperature are equal, the central core of the plasma can be ejected by slowly reducing the well depth. The initial current of the particles will correspond to the high-energy tail of a Maxwell-Boltzmann energy distribution [56]. The energy of an ejected particle E must be at least the effective depth of the well of the trap $E \geq q\left(\phi_{\mathrm{vac}} - \phi_{\mathrm{self}}\right)$, which combines both the trapping electric field ϕ_{vac} and the plasma self-potential ϕ_{self}. If the plasma self-potential does not vary significantly during the initial fraction of extracted particles, then the number of extracted particles N will scale as an exponential curve:

$$N(\phi_{\mathrm{vac}}) = \frac{1}{\sqrt{\pi k_B T_{\parallel}}} \exp\left(-\frac{q\phi_{\mathrm{vac}}}{k_B T_{\parallel}}\right). \tag{2.18}$$

The ejection time scale should be slower than the axial motion of the particles to ensure that all particles with sufficient energy escape, and faster than the time scales of induced instabilities. Typically, a temperature dump takes 1 ms to 20 ms to perform, with 10^3 to 10^4 voltage increments.

The ejected particle signal is measured differently depending on the species. Ejected antiprotons are directed onto the Catching Trap degrader foil, and the annihilation products are measured using scintillating detectors positioned on both sides of the Catching Trap apparatus. Ordinary matter and positrons are measured using the MCP instrument, similar to the imaging technique. The MCP is configured to operate at a higher charge avalanche gain compared to imaging the plasma; however, this requires reducing the phosphor voltage from 5000 V to 1500 V to avoid saturation of the phosphorescence light produced by the phosphor material. The particle signal can be measured either by using the Phosphor screen as a Faraday cup or by measuring the phosphorescence light with an external Silicon photomultiplier (described later in this chapter). The measuring device's signal is amplified to improve the signal-to-noise ratio of the initial exponentially rising component of the particle signal, even if later components of the measured signal saturate. An example of a recorded ejected particle signal is shown in Figure 2.11 (a). The natural logarithm of the signal is plotted versus the calculated on-axis potential well depth, as shown in (b), in (c). Taking the natural logarithm of Equation 2.18 results in the linear equation:

$$\ln\left(N(\phi_{\mathrm{vac}})\right) = \ln\left(\frac{1}{\sqrt{\pi k_B T_{\parallel}}}\right) - \frac{q\phi_{\mathrm{vac}}}{k_B T_{\parallel}}. \tag{2.19}$$

The gradient of this linear equation represents the temperature scaled. In practise, a line is fitted to a restricted range of the on-axis well depth, as shown by the blue patch
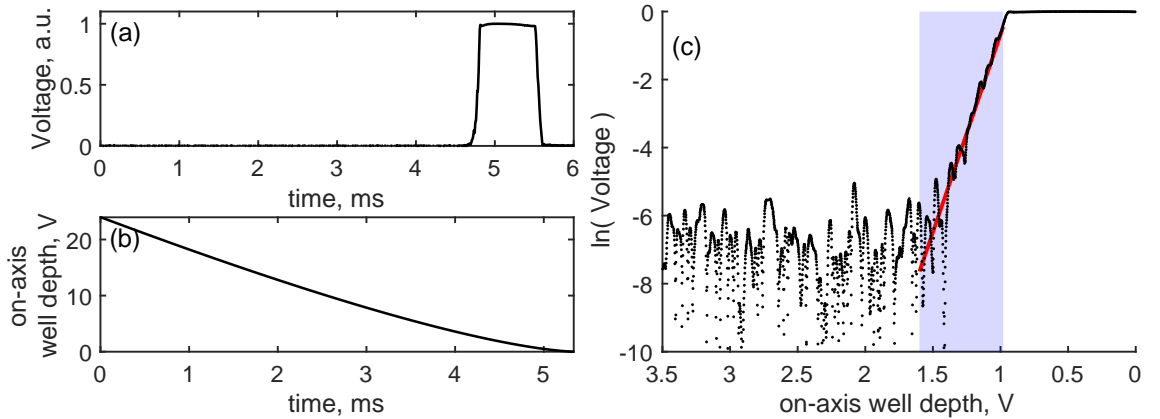
Figure 2.11: An example of a temperature diagnostic analysis for a 1535 K positive ion mixture. (a) Full signal of ejected particles during a temperature dump. (b) Calculated well depth during the dump. (c) The red line represents the linear fit, and the blue region indicates the fit range.

in Figure 2.11. The measured signal is dominated by environmental electrical noise during the early stages of the temperature dump, and only the initial particle signal is expected to increase exponentially, with the signal peaking at later times. This is the reason for restricting the linear fit to the initial appearance of the particle signal. Given a measured gradient X, the corresponding temperature can be determined as:

$$T_{\parallel} = \frac{q}{k_B X}. \tag{2.20}$$

2.5.3 Silicon photo-multiplier

The lower bound of plasma temperature calculated from the electrical readout of particle current on the MCP-Phosphor instrument is limited by electrical noise generated by mechanical vibrations. However, colder temperatures can be measured by using a light detector to measure the change in intensity of phosphorescence light rather than imaging the spatial distribution of plasma. This method has been demonstrated by colleagues [57] and was implemented within the ALPHA apparatus, utilising similar silicon photon-multiplier (SiPM) detectors, which are less sensitive to local magnetic fields produced by sources such as beamline magnets, compared to a photomultiplier tube. A SiPM consists an array of micro-sized avalanche photodiodes connected in parallel. When a photon enters the SiPM, it creates electron-hole pairs that trigger an avalanche in the avalanche photodiodes, producing a measurable current pulse. This system has also been applied to time-of-flight measurements, later discussed in Chapter 5.

2.5.4 CsI

The emission of 511 keV gamma rays from positron annihilation can be utilised to detect the presence of positrons, and the intensity of these rays is proportional to the number of positrons. This signal is detectable with a caesium iodide (CsI) detector, which is a combined package of a sensitive scintillating crystal and a photodetector. Numerous detectors are placed around the apparatus, and their compact form allows easy relocation to different positions.

These detectors can be used to debug the transport of positrons between traps. By analysing the time-of-flight signal from multiple detectors, the region where particle loss occurs can be identified, allowing appropriate corrective measures to be taken. Furthermore, there are mobile panel detectors that use a combination of scintillating plastic and a photomultiplier tube. These detectors have a larger sensitive area and can be used to measure the temporal distribution of positron bunches by obstructing the positron bunch path, either with a gate valve or by suitably positioning a multi-instrument stick.

2.6 Beamline - Plasma Transferline

Charged particles are transported between traps using magnetic beamlines, which consist mainly of a series of aligned solenoid magnets. The most complex beamline system within the ALPHA apparatus is the section connecting ALPHA-2, ALPHA-g, and the Positron Accumulator. This system incorporates an interconnect magnetic setup that can be configured to direct particles into one of the two antihydrogen apparatuses. A detailed discussion of this beamline system can be found in Mark A. Johnson's Ph.D. thesis [45]. Particles are ejected from traps with energies up to 140 eV, and the guiding magnets operate with field strengths between 0.01 T and 0.07 T.

The dynamics of charged particles within slowly changing strong magnetic fields is constrained by the adiabatic conservation of the magnetic moment, whereby the charged particles' motion becomes nearly fixed to the magnetic field lines. An adiabatic parameter γ approximates this condition as follows:

$$\gamma = \frac{\left(\left| \frac{\partial B}{\partial z} \right| / B_z \right)}{\left(\frac{\omega_c}{2\pi v_z} \right)}, \tag{2.21}$$

where the numerator represents the relative change in axial magnetic field strength per unit axial distance and the denominator is the unit axial distance travelled per cyclotron cycle. An ideal magnetic beamline will have values of γ much smaller

than one. This condition holds true for particle transport from the Catching Trap to ALPHA-2, as seen in red in Figure 2.12 (b). However, this condition is not satisfied for higher ejection energies required for MCP diagnostics, as illustrated in black in (b). This condition becomes less satisfied with heavier ions, as γ is directly proportional to the mass-to-charge ratio. For example, H_3^+ will experience poor transport conditions at 100 eV between the Catching Trap and the CT stick. Furthermore, at
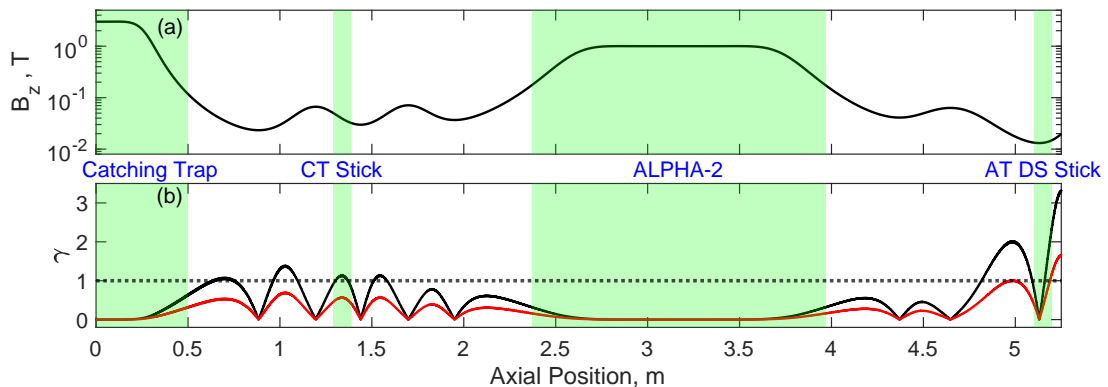
Figure 2.12: (a) Axial magnetic field strength of the ALPHA apparatus, and (b) approximate adiabatic parameter calculated for a 100 eV (black line) and 25 eV (red line) proton. Blue regions indicate the location of each labeled system.

the downstream stick beyond ALPHA-2, the condition is not satisfied for energies as low as 25 eV, as seen at the far right end of Figure 2.12. This issue was addressed by Mark A. Johnson in his thesis work [45], which focused on the transport of particles from the Catching Trap to ALPHA-g. The beamline performs exceptionally well during operation, but it does require some fine-tuning depending on changes to nearby magnetic materials and the usage of nearby magnets. Fine-tuning is carried out shot-to-shot from the relevant particle source.

2.7 Vacuum and Cryostat Systems

For effective particle dynamics within a Penning trap, minimal scattering is necessary since it can cause outward radial transport to untrappable regions, leading to particle ejection. Coulomb scattering between trapped charged particles occurs over long ranges, resulting in shallow scattering angles. In contrast, neutral atoms approach charged particles at much closer distances, causing larger scattering angles. Particle losses can also occur if trapped particles are reactive with the residual gas, which poses a significant concern for antimatter, as it can annihilate with any neutral gas atom.

The intrinsic lifetimes of free antiprotons, positrons, and antihydrogen have not been directly observed. Antiprotons have been continuously trapped for 405 days by the BASE Collaboration [58] without any evident intrinsic lifetime within these

timescales. Current lifetime limitations are primarily associated with the quality of the trap vacuum. Consequently, antimatter trap experiments require an ultra-high vacuum to ensure that the annihilation lifetime is negligible compared to the timescale of each antimatter measurement or to have a systematic understanding of this lifetime within their system.

2.7.1 Cryogenics and cryocooling

A cryogenic trap serves two purposes: it reduces the heating of trapped particles due to blackbody radiation and acts as a cryopump to further reduce the vacuum pressure. Both liquid and compressor methods are used to obtain a cryogenic environment in the ALPHA apparatus. Both the Catching Trap and Positron Accumulator use helium compressors and cold heads for both the main superconducting solenoid and electrode stack. Although ALPHA-2 uses both liquid helium and liquid nitrogen to cool its main superconducting solenoid, and only liquid helium to cool its superconducting neutral atom trap and electrode stack. Alternatively, ALPHA-g uses a cryocooler for its primary superconducting solenoid and liquid helium to cool its superconducting neutral atom trap and electrode stack. All electrode stacks are cooled to around 7 K and can vary by a few Kelvin across the stack. Additional vacuum volumes exist surrounding cryogenic volumes to reduce heat flow from the room temperature laboratory to the cooled material.

2.7.2 Operational performance

ultra-high vacuums within the ALPHA apparatus are obtained using conventional methods and commercial hardware. These systems use a series of scroll pumps, turbo pumps, and ion pump stages from initial atmospheric pressure to ultra-high vacuum. The vacuum is monitored using Pirani gauges and cold cathode gauges. These are typically paired up and placed adjacent to the Penning-Malmberg traps and along magnetic beamlines. Gate valves are positioned between neighbouring Penning traps and close to the multi-instrument sticks. These reduce cross-contamination between different systems, as the positron accumulator operates with both neon gas and nitrogen gas, and to reduce the volume of the vacuum exposed to air when an intervention is necessary. Systems that are exposed to air will be baked out to improve the base vacuum pressure by 1 to 2 orders of magnitude and to minimise ice build-up when at cryogenic temperatures. When the traps are at cryogenic temperatures (4 K - 10 K), the cold cathode gauges will read about 10^{-10} mBar, as they are positioned at a room temperature location. The pressure within the cryopumping Catching Trap can be estimated with measured antiproton annihilation lifetimes and theory from Xiang Fei's Ph.D. thesis [59, Chapter 6, Eq. 6.11], as 10^{-12} mBar to 10^{-13} mBar. The pump rate of cryopumping reduces with time following

the adsorption of many layers of residual gas. This reduced pump rate will increase the base vacuum pressure within the trap, causing the antiproton annihilation rate to increase. Therefore, the antiproton annihilation lifetime is monitored, and when it is short enough to affect the yield of trappable antihydrogen, the system is thermally cycled. This causes the adsorbed material to boil off and be pumped out of the system, which essentially resets the vacuum quality of the trap.

2.8   The 1S-2S transition in antihydrogen

Antihydrogen, the antimatter counterpart to hydrogen, is an intriguing subject of study, particularly in the context of 1S-2S spectroscopy. Precise spectroscopic measurements of the 1S-2S transition in antihydrogen can test the Charge-Parity-Time (CPT) symmetry, a fundamental principle of quantum field theory which posits that the laws of physics remain unchanged under charge conjugation, parity transformation, and time reversal. By comparing the 1S-2S transition frequencies in hydrogen and antihydrogen, we can verify whether this principle holds. Moreover, these experiments can also test the predictions of the standard model of particle physics, which suggests that hydrogen and antihydrogen should have identical spectroscopic properties.

The 1S-2S transition in hydrogen is a transition of an electron from the ground state to the 2S excited state that is performed by absorbing two counter propagating photons of 243 nm wavelength. The energy level diagram of the 1S and 2S hyperfine states of hydrogen as a function of the external magnetic field strength is depicted Figure 2.14, and the 1S-2S c-c and d-d transitions are indicated by arrows.

Hydrogen has been measured with a fractional precision of 4.2×10^{-15} [31]. Recent measurements determined the 1S-2S transition frequencies, d-d line, of antihydrogen at a fractional precision of 2×10^{-12} [32].

2.8.1   Laser system of 1S-2S measurements

A schematic of the 1S-2S spectroscopy system is shown in Figure 2.13. All technical details related to the laser system and enhancement cavity was taken from [60]. The system has been coloured into different regions for different purposes. High 243 nm laser power is needed to induce the 1S-2S transition of antihydrogen in the ALPHA-2 trap, due to the low density and thermal broadening of trapped antihydrogen. A Fabry-Pérot enhancement cavity is used to increase the laser power within the ALPHA-2 magnetic trap region, as a 1 W laser power, 243 nm laser, is not commercially available. A commercial Toptica tapered amplifier fourth harmonic generation (TA-FHG) laser is used to generate 243 nm light. The diode laser generates the fundamental frequency of 972 nm at an intensity of 50 mW, which is

increased 2.5 W by a tapered amplifier. This frequency is next twice doubled in the Second Harmonic Generation cavity to produce 100 mW of 243 nm light. The 243 nm laser light is transported from a neighbouring laser laboratory into the ALPHA-2 apparatus. The enhancement cavity is contained within the ultra-high vacuum of the ALPHA-2 trap, which is cooled to cryogenic temperatures. The optical path
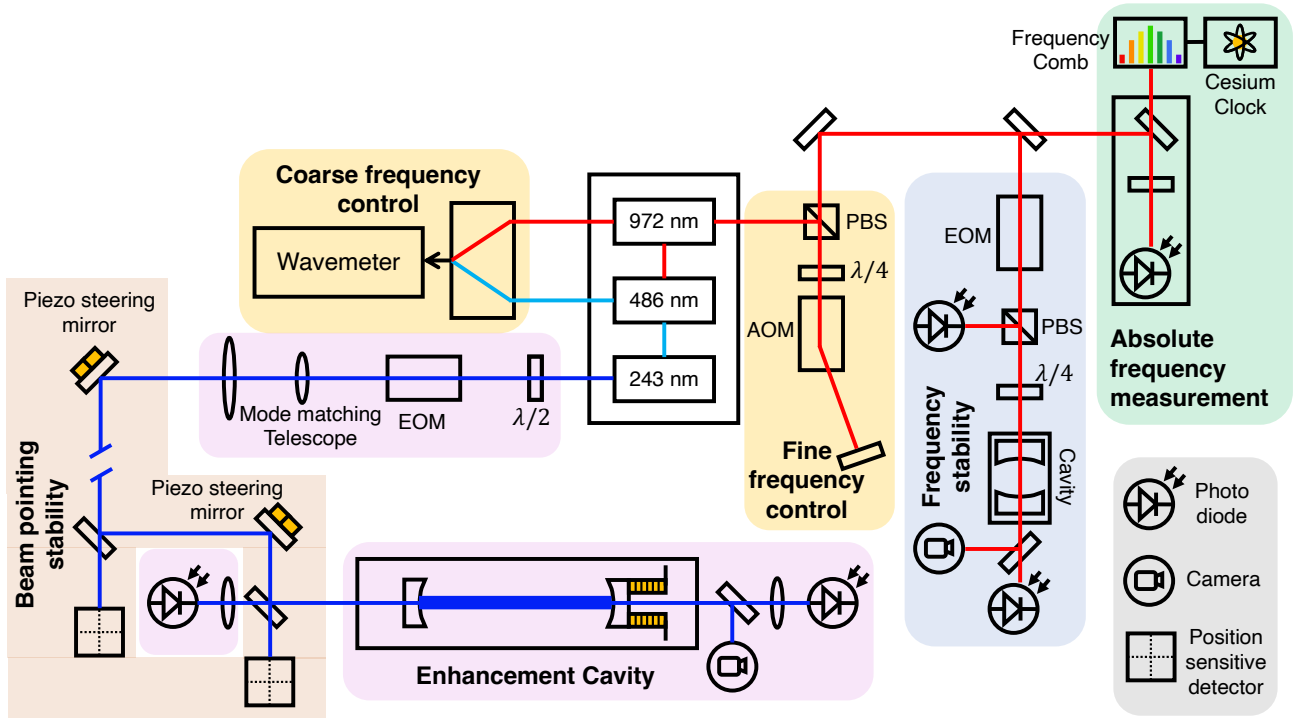
Figure 2.13: A schematic of the 1S-2S spectroscopy setup. Red, cyan, and dark blue lines are the paths of 972 nm, 486 nm and 243 nm laser light. Adapted from [60].

uses a combination of piezo steering mirrors and position sensitive detectors to stabilise beam pointing, as misalignment of the enhancement cavity will reduce power build up by 50 %. The enhancement cavity is locked using the Pound–Drever–Hall locking method, by using sidebands generated from an electrical optical modulator that intercepts the beam before entering the cavity.

The enhancement cavity in the ALPHA-2 trap is mounted to direct laser light, such that the beam crosses the central trap axis at an angle of 2.3°. This beam overlaps with the antihydrogen trapping volume in the middle of the ALPHA-2. The beam waist at the trapping region is 0.2 mm.

The frequency control and frequency stability of the 243 nm laser light is inherited from the 972 nm laser, and its absolute frequency value is determined from this 972 nm laser. This frequency stability is from a laser locked ultra-stable reference cavity, composed of ultra-low coefficient of thermal expansion glass, with a 1 Hz line width and a 53 mHz/s linear drift. The line width of this reference cavity is monitored by beating it against an identical system. The frequency control is obtained from two systems. Coarse control is performed by sending the second harmonic generated
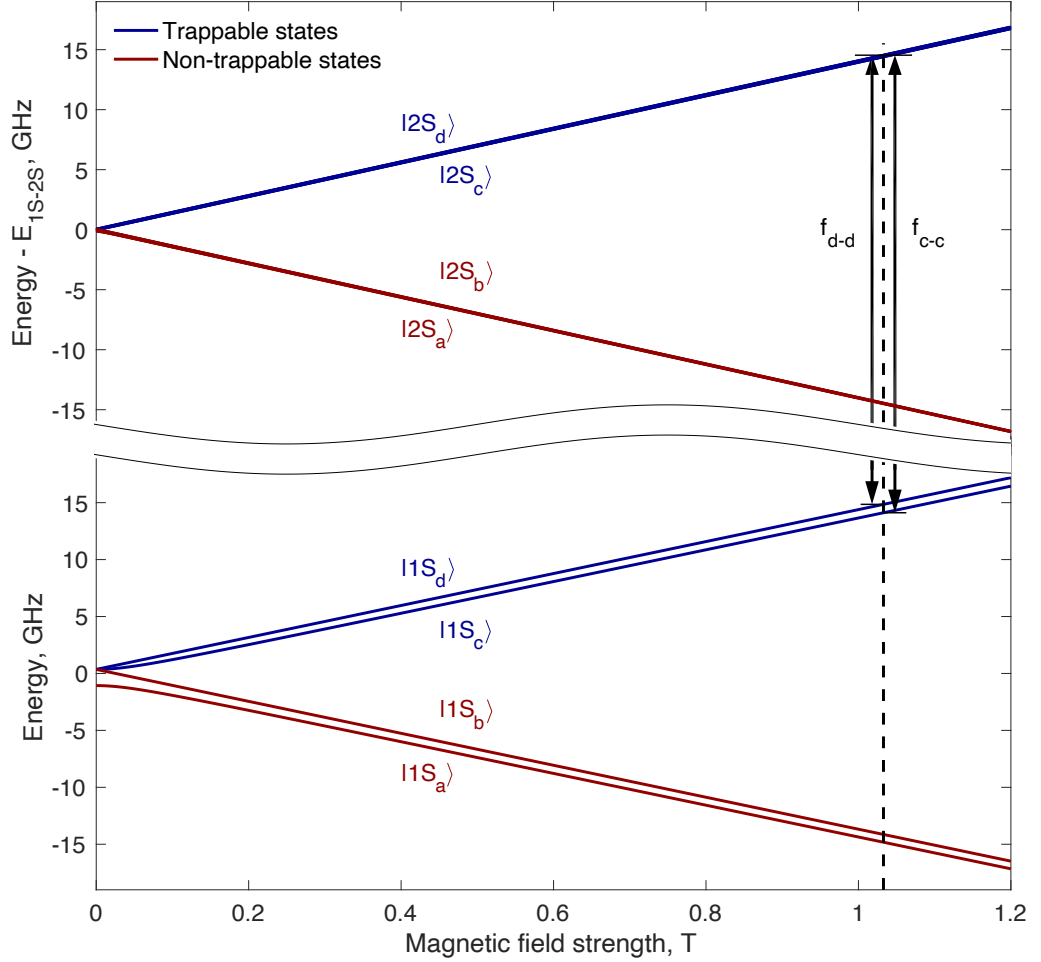
Figure 2.14: Hydrogenic energy levels. Calculated energies for hydrogen of the hyperfine sublevels of the 1S (bottom) and 2S (top) states as functions of magnetic field strength. The centroid energy difference $E_{1S-2S} = 2.4661 \times 10^{15}$ Hz has been suppressed on the vertical axis. Vertical black arrows indicate the two-photon transitions (which occur with frequency f_{c-c} or f_{d-d} between the trappable 1S and 2S states. Adapted from [61]

486 nm laser light into a wavemeter with a 2 MHz precision, which then feedback into the 972 nm laser. Fine control is performed with an acousto-optical modulator (AOM) acting on the 972 nm laser light that is sent to both the reference cavity and a frequency comb. The AOM can sweep the laser frequency between the c-c and d-d antihydrogen 1S-2S transitions and finely scan the line width of each transition. The 972 nm laser frequency is obtained by beating the reference cavity laser against a tooth from a frequency comb (Menlo Systems FC1500-250-WG). The comb is referenced to a Symmetricom CS4000 Caesium microwave clock and is stabilised from a GPS-disciplines oven controlled quartz oscillator. This provides an accuracy of 250 Hz at 972 nm and thus 1 kHz at 243 nm.

For a more complete description and discussion of the 1S-2S hardware setup, read Steve Armstrong Jones' Ph.D. thesis [60].

2.8.2 Protocol of 1S-2S measurements

Spectroscopy of antihydrogen is a destructive process, in that the spectroscopy signal is antiproton annihilation. The 1S-2S transition is a double photon excitation process, where counter propagating 243 nm photons are absorbed such that the combined absorption spectrum is Doppler free. The transition is observed either from a third 243 nm photon causing photo-ionisation and then the free antiproton collides with the inner apparatus surface, or the excited atom relaxes by photon emission to a untrappable state (positron spin flip). The absolute laser frequencies to be used during a spectroscopy measurement are informed by hydrogen physics calculations, which estimate the shift from the centroid frequency [31] due to the central magnetic field in the ALPHA apparatus. Known hydrogen physics is used within Monte Carlo simulations to determine the expected corresponding antihydrogen spectra within the ALPHA-2 magnetic trap. The simulation uses a magnetic field map that is calibrated using magnetometry measurements at the central field obtained using an electron cyclotron resonance method [38] and the off-axis fields consider the known geometry of conductors. The simulations also use the measured 243 nm laser parameters, such as beam waist and beam intensity. Further details of related simulations can be found in Chris Ørum Rasmussen's Ph.D. thesis [62].

2.9 Conclusion

Penning traps serve as versatile instruments in numerous types of trapped-ion research. Within the context of the ALPHA experiment, these traps are used to manipulate antiproton and positron plasmas to facilitate antihydrogen production. The techniques employed for plasma manipulation and diagnosis are derived from the standard methods used in low-energy trapped plasma research, referenced in [63], and are shared among various other low-energy plasma groups. While these methods have been customised for specific applications in antimatter research, the Penning trap apparatus, in essence, offers the potential to manipulate any type of low-energy ions, utilising the same techniques.

The application of research within ALPHA using other ion types is primarily constrained by the feasibility of integrating the ion sources into the existing apparatus. Manipulation and diagnostic techniques have the potential to be easily adapted to other ion species with minimal hardware modifications. An example of such adaptability is the introduction of a beryllium ion source into the ALPHA-2 trap. This addition allowed beryllium ions to sympathetically cool the plasma of positrons, a modification expected to improve antihydrogen trapping [64, 65].

The ALPHA-2 trap, a combined Penning trap and neutral atom trap, theoretically has the capability to trap neutral hydrogen, thus enabling a direct CPT test

under the same experimental conditions. However, the primary technical hurdle lies in the integration of a proton source. Should protons be present in the ALPHA-2 apparatus, similar or equivalent manipulations as those applied to antiprotons can be conducted, such as sympathetic cooling with leptons, i.e., positrons/electrons.

The focus of this research is to establish a proton source that does not necessitate the installation of an external proton source or significant irreversible changes to the ALPHA traps. Chapter 4 will explore the electron impact ionisation process, enabling the production of hydrogen ions from the residual gas present in one of the ALPHA's Penning traps, the Catching Trap. Furthermore, Chapter 5 will discuss the process of isolating protons from a mixed plasma of positive hydrogen ions.

In summary, the ALPHA apparatus presents immense potential for various plasma experiments. These could potentially incorporate existing techniques into antihydrogen experimental protocols, thereby enhancing various facets of antihydrogen research. Some possibilities include improved antihydrogen production via sympathetic positron cooling with laser-cooled beryllium ions, studies of systematic errors. For example, electrode patch potential diagnostics [66], magnetometry through enhanced ECR techniques [38] and magnetometry via electron spin flip in beryllium ions also remains an intriguing possibility.

CHAPTER 3

ION PRODUCTION

The purpose of anion hydrogen production within the ALPHA experiment is twofold. Firstly, it serves as a hydrogen source through the photodetachment of the secondary electron. In the context of ALPHA's antihydrogen studies, a technique that generates trappable hydrogen within the neutral trap volume could facilitate in situ atom-antiatom spectroscopy schemes. Direct CPT comparisons can eliminate the need to extrapolate low-magnetic field spectroscopy measurements to high-magnetic fields, which is currently required for antihydrogen spectroscopy comparisons with hydrogen. However, this necessitates a measurement scheme that is applicable to both species, such as fluorescence detection using silicon photomultipliers (SiPM) or the detection of photoionised protons and antiprotons using a charge-sensitive device using a micro-channel plate (MCP). A suitable SiPM device is currently being investigated within ALPHA, specifically for this application. It is important to note that the current charged-pion detection method for antiproton annihilation in ALPHA is not applicable to hydrogen.

The second objective is to utilize ion studies for optimizing antiproton experiments. Negative hydrogen has the same total charge as an antiproton and a similar charge-to-mass ratio. This characteristic makes it a suitable substitute for studies that have been limited due to the restricted antiproton delivery schedule of CERN's AD complex. The proton is useful in this context since its charge-to-mass ratio is nearly identical to that of an antiproton, especially when considering the degree of experimental uncertainty involved in the studies of interest.

3.1 Anion hydrogen production study

A study was conducted, similar to Kabanstev *et al.* [67], into the production of the anion hydrogen atom H^- by dissociative electron attachment (DEA) of electrons to molecular hydrogen. This involved experiments using trapped electrons to ionise

residual hydrogen gas within the vacuum of the Catching Trap apparatus. This process can be written as two steps:

$$\mathrm{e}^- + \mathrm{H}_2(\nu, J) \rightarrow \mathrm{H}_2^- \rightarrow \mathrm{H}^- + \mathrm{H} \tag{3.1}$$
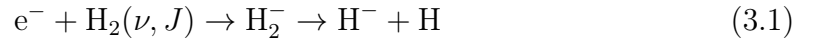
where ν and J are the vibrational and rotational quantum numbers of the hydrogen molecule, respectively. The anion hydrogen atom H^- is a hydrogen atom with a second bound electron, this atom has a single bound state and thus no excited states. At the beginning of this study it was assumed that the residual gas of the Catching Trap vacuum would be partially composed of hydrogen, as stainless steel walls of vacuum apparatus are known to outgas hydrogen [68].

The combined cross section of both processes, described by Equation 3.1, has an onset threshold of electron energy is between 3.5 to 4 eV. The magnitude of the cross section is significantly affected by the quantum state of the target hydrogen molecule. As the peak cross section for dissociative electron attachment of electrons to ground state molecular hydrogen is on the order of 10^{-21} cm^2 [69]. Electrons within the Catching Trap have a cyclotron cooling time of sub-seconds, this results in the trapped electrons having energies below the onset threshold for the DEA process. Trapped electrons must be driven to higher energies for this DEA process to occur. To achieve this, the electron axial motion was driven with an external electric drive. The drive signal was generated by a SRS DS345 waveform generator. The applied drive signal was white-noise, for further details regarding the response of trapped electrons to the applied signal type see Section 4.1. The waveform generator output was connected to a single electrode, via a feedthrough connection, involved in producing the trap electric potential to improve coupling to the axial motion of trapped electrons, as described later in Section 4.1. The driven electrons were observed to expand radially leading to electron losses. This was corrected by using a rotating wall to improve radial confinement, as described in Section 2.2.1. The experimental sequence to study the production of anion hydrogen within the Catching Trap is the following:

1. Inject and capture electrons (ranging from $10^8 - 10^9$ electrons), as described in Section 2.3.1.

2. Change the applied voltages on trap electrodes to expand the axial length of the electron trapping well, such that the electrons are distributed across a large volume of the trap, including one of the segmented electrodes within the trapping region.

3. Apply a rotating wall signal to radially compress the trapped electrons.

4. Drive the electron axial motion with an external electric drive.

5. Wait a fixed duration (up to 3 hours), while both the rotating wall signal and external electric drive signal are continuously active.

6. (Optional) Remove all or a fraction of the electron population by using the electron kick method, described in Section 2.2.2.

7. Measure the remaining population with a Faraday Cup, as described in Section 2.5.1, or image the axially integrated radial profile using a MCP instrument, as described in Section 2.5.2.

This study resulted in no observation of anion hydrogen production by axial driven electrons.

To explain why this study did not produce anion hydrogen it must be understood that the DEA cross section increases for rovibrationally excited molecular hydrogen. A 4 orders of magnitude increase in the DEA cross section was observed by Allan *et al.* [70] for hydrogen gas in excited ro-vibrational states ($\nu = 0 - 5$ and $J = 0 - 7$). The temperature of the hydrogen gas will define the rovibrational quantum state distribution, as increased temperatures will have an increased occupancy of larger J and ν quantum numbers.

Thermal rovibrational state distributions can be estimated assuming a Boltzmann energy distribution defined by the temperature of the gas and the rovibrational spectra of molecular hydrogen found in Table 1 of Komasa *et al.* [71]. The molecular hydrogen gas in the Catching Trap vacuum will be in thermal equilibrium with the interior trap surfaces, which are cooled to 7 K, for details Section 2.7.1. The fraction of rovibrationally excited states of a thermal distribution of molecular hydrogen at 7 K was calculated to be practically non existent, such that the entire gas can be considered to occupy their ground state. Contrary to this, the Kabenstev study involved a room temperature Penning Trap. A room temperature hydrogen gas is estimated to have active rotationally excited states ($J = 1, 2$), though no excited vibrational states. This means that this study using the Catching Trap is performed in a cryogenic environment which is unsuitable to expect appreciable anion hydrogen production.

During the anion hydrogen experiments the production of positive ions was observed. The ions were later identified as H^+, H_2^+ and H_3^+.

3.2   Proton source development

The work presented here aims to produce and study proton plasmas in ALPHA apparatus. The intention is to use preexisting hardware with no further modification to the interior electronics of the Penning Trap. The discussion begins with a brief overview of historical studies on protons and the development of proton sources to

enable a deeper understanding of the processes and outcomes involved in subsequent proton studies performed in the ALPHA experiment. The production of protons and other hydrogen ions from molecular hydrogen via electron impact ionisation will be discussed. In the ALPHA experiment it is not desired to introduce hydrogen gas to the trap vacuum system. The residual gas inside the trap is mostly composed of the molecular hydrogen, therefore a method was proposed to ionise the hydrogen gas already present in the trap by using an electron plasma. The feasibility of this approach and estimated rates for the protons and other hydrogen ions generation in the ALPHA apparatus will be discussed. Trapped protons and other hydrogen ions could contribute to further ionisation of the residual gas, the rate at which those processes happen can be understood by looking at the collision frequencies between different ion species. This section will be summarised by possible prospects of a proton plasma study, similar to antiproton plasma in ALPHA experiment, and with remarks about possible differences in diagnostics methods between both proton and antiproton plasma.

3.2.1 Basic processes and raw material of choice

Most modern proton sources utilize mechanisms to ionize molecular hydrogen, as it has a relatively small dissociation energy of 15.4 eV [72]. Monatomic hydrogen, with its smaller ionisation energy of 13.6 eV, is highly reactive at laboratory temperatures below 25 °C due to the possibility of hydride formations. This reactivity causes hydrogen atoms to deplete within cyrogenic environments by reacting with interior vacuum surfaces unless they are spatially confined. Therefore, it is expected that monatomic hydrogen would not survive within the Catching Trap vacuum, as it is a cryogenic trap.

Alternative methods for producing hydrogen atom sources include matrix isolation sublimation [73] and photo-detachment of heavy molecular ions [74, 75, 76]. Both of these methods have been suggested as potential candidates within the ALPHA apparatus. However, the former approach necessitates the integration of a dedicated magnetic field guide for injection into the trapping region, while the latter has not yet been demonstrated in a laboratory setting.

Hydrogen can be ionized through various mechanisms, including electron impact, ion impact, field ionisation, and laser absorption.

Field ionisation is disregarded due to its requirement for extreme electric field strengths, considering that the hydrogen molecular bond length is approximately 10^{-10}m and the associated electron binding energies are on the order of 10 eV. Photo ionisation is also ruled out because it would require ultraviolet light at 91.2 nm. Ultraviolet light can generate photo-electrons on the inner surfaces of the Penning trap, which in turn leads to electrostatic patch potentials [66]. These patch

potentials complicate plasma manipulation and thus make laser absorption an undesirable method for ionising hydrogen.

3.2.2 Electron impact ionisation

The most accessible mechanism for ionising hydrogen in the Catching Trap is via electron collisions. Electron trapped within the Catching Trap will stochastically collide with residual gas. However, the 3 T magnetic field strength of the Catching Trap solenoid will cause the electrons to cool via cyclotron radiation, and they are observed to thermally equilibrate in a few seconds to temperatures below 1000 K. Electrons at corresponding energies cannot cause observable ionisation of the residual gas. The energies of trapped electrons must be increased before ionisation is observed. In practise this can be done by coupling the electron axial motion to an external electric drive, as described in Section 3.1. The induced energies must be above the ionisation potentials for ion production to be observed. Ionisation is an endothermic process whereby the accelerated electrons lose energy. To sustain the hydrogen ionisation process either power must be continually coupled into the electrons or newly accelerated electrons must be introduced.

3.2.3 Early studies of molecular hydrogen

Ionisation of molecular hydrogen by electron impact has been studied for over a century. These early works [77] measured both the ionisation potentials of electron impact processes and the kinetic energies of the hydrogen ions that are produced. The molecular hydrogen within the cyrogenic trap is predicted to be in its rovibrational ground state. Three electron impact channels are observed for ground state molecular hydrogen with onset electron energy thresholds below 30 eV. These processes are listed below, in order of increasing impact electron energy based on literature are:

$$\mathrm{e^-} + \mathrm{H_2} \rightarrow \mathrm{H_2^+}(\mathrm{X}^1\Sigma_g^+) + 2\,\mathrm{e^-} \qquad\qquad 15.426\,\mathrm{eV}\,[78] \qquad (3.2)$$

$$\mathrm{e^-} + \mathrm{H_2} \rightarrow \mathrm{e^-} + \mathrm{H_2^+}(\mathrm{X}^1\Sigma_g^+) + \mathrm{e^-} \rightarrow \mathrm{H} + \mathrm{H^+} + 2\,\mathrm{e^-} \qquad 18.1\,\mathrm{eV}\,[78] \qquad (3.3)$$

$$\mathrm{e^-} + \mathrm{H_2} \rightarrow \mathrm{e^-} + \mathrm{H_2^+}(\mathrm{X}^1\Sigma_u^+) + \mathrm{e^-} \rightarrow \mathrm{H} + \mathrm{H^+} + 2\,\mathrm{e^-} \qquad 26 \pm 1\,\mathrm{eV}\,[79] \qquad (3.4)$$
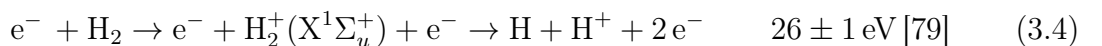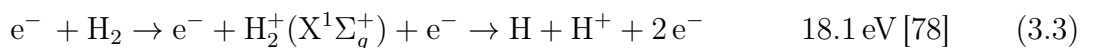
The first observed channel is the dissociative attachment of molecular hydrogen by electron impact to a positively charged hydrogen molecule ($\mathrm{H_2^+}$), the second and third channels are both dissociative ionisation of molecular hydrogen by electron impact to monatomic hydrogen (H) and a proton ($\mathrm{H^+}$). The second and third channels have an intermediary process of producing a $\mathrm{H_2^+}$. The second channel produces a $\mathrm{H_2^+}$ in its electronic ground state, while the third channel process a $\mathrm{H_2^+}$ in its lowest electronic excited state.

At higher electron impact energies a total ionisation process can occur:

$$e^- + H_2 \rightarrow 2H^+ + 3e^-, \; 46 - 56\,\text{eV} \tag{3.5}$$
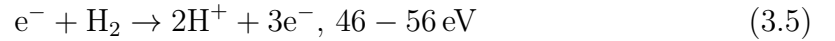
Though this process is not ideal as the protons will be produced with a non-zero lower bound kinetic energy, due to their repulsive Coulomb potential. Without a cooling mechanism those energetic protons would be difficult to capture in the Catching Trap without suffering from evaporative losses.

The protons produced via channel 3 are produced with a non-zero kinetic energy. The binding energy between hydrogen atom and proton in the $H_2^+(X^1\Sigma_u^+)$ state is negative, therefore proton experiences a repulsive force. For example protons produced from ro-vibrational ground-state molecular hydrogen are predicted to have energies of a least 5 eV [77]. However, H_2^+ does not experience such a repulsion and can in theory be produced with low kinetic energies. This disregards excited ro-vibrational states, which one may expect allow for lower energy protons. In the context of this study, if the trap residual molecular hydrogen gas is in thermal equilibrium with the cryogenic trap material, such molecular hydrogen gas will be in the rovibrational ground state.

3.2.4 Ion Impact Ionisation

A concern that may arise within the context of proton production and trapping studies is whether trapped protons could cause further ionisation of residual gas. Readers interested in collisional dynamics of low temperature hydrogen plasmas are directed towards a review by Janev, Reiter and Samm [80]. An ion-atom collision that causes an electron to transfer between the two is referred to as charge-exchange or charge-transfer collision. This process occurs when the ion's relative speed is similar in magnitude to the outer electron's orbital speed of the atom. Due to the mass difference of atomic ion compared to an electron, such a charge-exchange collision requires ion energies on order of keV scale. Unfortunately there is a lack of theoretical predictions and measurements for the energy ranges within the context of this study. Taking the cross-section for a proton-monatomic-hydrogen ionisation collision from literature [81] a back of the envelope calculation predicts this process to occur at a negligible rate, though the available cross-section only has predictions down to 100 eV.

3.2.5 Proton sources

Many ion sources in scientific research and industry are devices that rely upon electron-impact ionisation of a specific gas followed by some charge and mass selective techniques [82]. Typically, these devices direct electrons into a confinement

region, where microwaves coupled into this region drive the electron motion. Gas is injected into the heated electrons causing the gas and electrons to collide. By tuning the coupled microwave signal, electrons can be driven to energies greater than the gas's ionisation threshold causing electron-impact ionisation. The product ions are then filtered through to a secondary region for extraction. An alternative method, is to create a DC discharge in the gas and to apply an accelerating voltage across the generated plasma to extract ions. Both of these methods were previously investigated by the GBAR collaboration to be used in commissioning an antiproton beamline [83].

3.2.6 Protons in traps

Within one year of Dehmelt's initial demonstration of electron trapping in a Penning trap [84] he had trapped protons[85]. The protons were suspected of being produced by the injected electron beam ionising residual molecular hydrogen. In more modern Penning trap experiments [86, 25], a common technique for loading protons is to direct a kilo-volt electron beam to strike a metal surface adjacent to the trap entrance. Since the trap is cryogenic, hydrogen gas freezes on the metal surface. The electrons sputter hydrogen atoms outwards from the surface, and those atoms that intersect the path of the electron beam may undergo electron impact ionisation. This process can allow one to load 1 to 10^4 protons, though it is not clear how long this takes.

3.3 Conversion Rates

To effectively study a positive hydrogen ion plasma, it is ideal that the ion interaction rates with the residual gas during the timescales of the experiments, typically on the order of minutes, are sufficiently low to ensure an approximately constant composition. This section investigates how the temperature of the ion plasma impacts the collision frequencies of processes that may alter the composition and subsequently estimates the timescale for experiments.

Due to the absence of quantitative data regarding the residual gas composition within the Catching Trap and the lack of a pressure gauge, only approximations of the upper limits of collision frequencies can be deduced. As the trap operates under cryogenic conditions, it is expected that the composition of the residual gas is predominantly molecular hydrogen. For the purpose of these calculations, it is assumed that the entire composition of the residual gas consists of molecular hydrogen. Furthermore, without knowledge of the energy distribution of the residual gas, it is postulated that the residual gas is in thermal equilibrium with the internal trap surfaces, having temperatures ranging between 4-8 K, with molecular hydrogen at a temperature of 8 K.

The operational pressure within the Catching Trap has previously been evaluated as a function of time since the last thermal cycle of the trap, as detailed in Section 2.7.2. This was inferred from a series of previous ALPHA studies on antiproton lifetimes within the Catching Trap, which measured up to two weeks after a trap thermal cycle. However, these measurements did not establish whether the operational pressure reached a steady state. It is anticipated that the trap pressure would increase during these extended periods as a result of the further degradation of cryopumping facilitated by the cold trap surfaces. The Catching Trap vacuum must be degraded to generate positive ions at a feasible rate. To approximate collision rates, a third assumption is made: the degraded Catching Trap vacuum has a pressure equal to the highest value calculated from the lifetime study, which is $(3.24 \pm 0.51) \times 10^{-13}$ mbar.

The first assumption restricts possible reactions to that of hydrogen ion interactions with molecular hydrogen. The second and third assumption sets the density of molecular hydrogen within the trap, following from the ideal gas law. I use a rate constant that has been averaged over a Maxwellian distribution defined by the plasma temperature T_{ion}, such that for a process with a cross-section, σ, and an ion velocity, v_{ion}, the rate constant is given by

$$\langle \sigma \cdot v_{ion} \rangle = \sqrt{\frac{8}{\pi \mu}} \left(\frac{1}{k_B T_{ion}} \right)^{\frac{3}{2}} \int_0^\infty \sigma(E_{ion}) E_{ion} \exp \left[-\frac{E_{ion}}{k_B T_{ion}} \right] \mathrm{d}E_{ion}, \qquad (3.6)$$

where E_{ion} is the ion kinetic energy, μ is the reduced mass of the colliding bodies and k_B is the Boltzmann constant. The collision frequency, ν, of a process is the product of the rate constant and the gas density. Thus we have

$$\nu = \langle \sigma \cdot v_{ion} \rangle \frac{P_{H_2}}{k_B T_{H_2}}, \qquad (3.7)$$

where P_{H_2} and T_{H_2} are the residual molecular hydrogen pressure and temperature, respectively. Figure 3.1 shows calculated collision frequencies for each the hydrogen ions, (a) H$^+$, (b) H$_2^+$ and (c) H$_3^+$, with a molecular hydrogen gas of temperature and pressure 8 K and $(3.24 \pm 0.51) \times 10^{-13}$ mbar, respectively. These calculations only consider reaction processes with ion products and energetic processes that conserve the initial ion. In Figure 3.1 processes that either conserve a proton or produce one is shown by a black line, this is similar for H$_2^+$ with a red line and H$_3^+$ with a blue line. In Figure 3.1(a) the solid black line is the proton impact dissociation process [80]:

$$\mathrm{H}^+ + \mathrm{H}_2 \rightarrow \mathrm{H}^+ + \mathrm{H} + \mathrm{H}. \qquad (3.8)$$
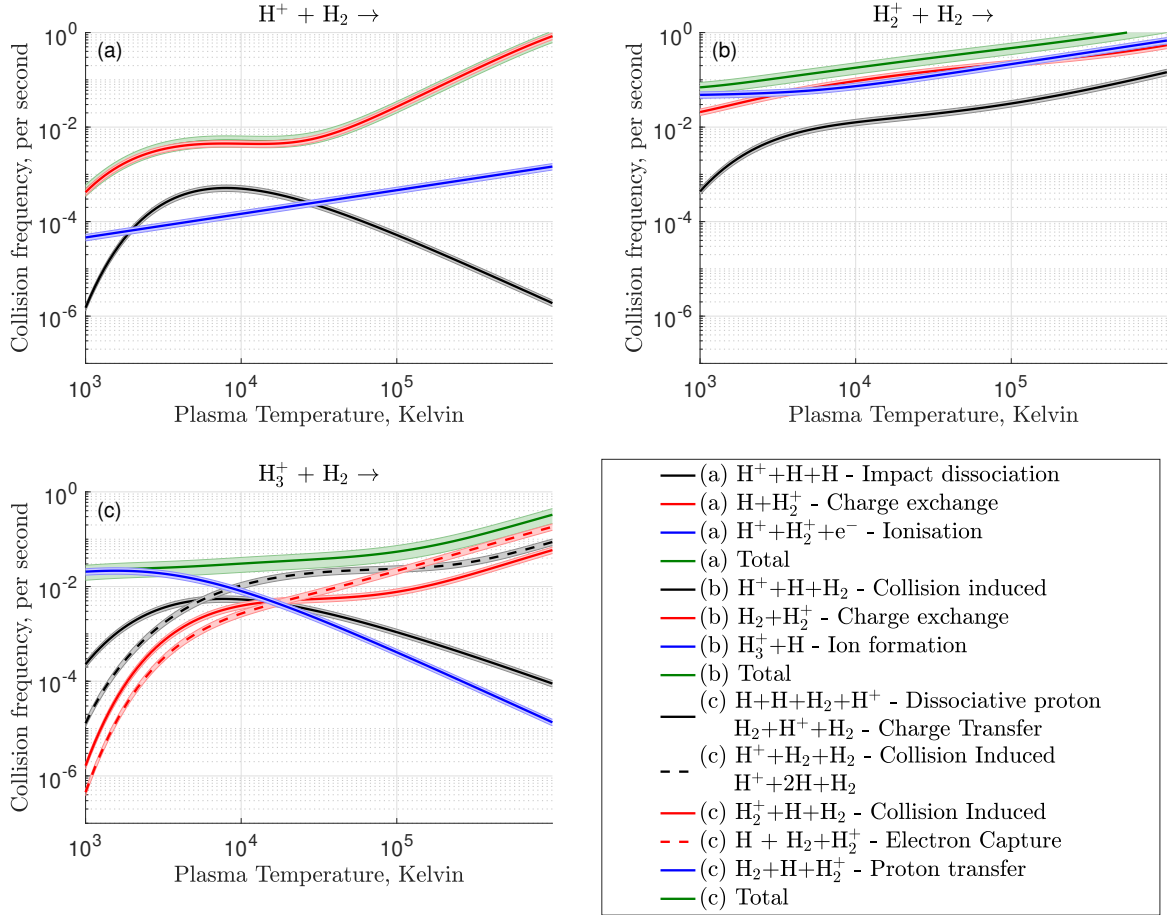
Figure 3.1: The collision frequencies for some channels of reactions of hydrogen ions interacting with residual molecular hydrogen gas is plotted against the ion temperature. The H_2 gas is assumed to have a temperature and pressure of 8 K and $(3.24 \pm 0.51) \times 10^{-13}$ mbar respectively. The green lines correspond to the total summed collision frequencies shown in each subplot. (a) Proton collision with H_2, (b) H_2^+ collision with H_2 and (c) H_3^+ collision with H_2. The shaded regions correspond to single standard deviation uncertainties, due to the systematic uncertainty of the calculated residual gas pressure.

The solid red line is the charge exchange process [80]:

$$H^+ + H_2 \rightarrow H + H_2^+.$$ (3.9)

The solid blue line is the ionisation process [80]:

$$H^+ + H_2 \rightarrow H^+ + H_2^+ + e^-.$$ (3.10)
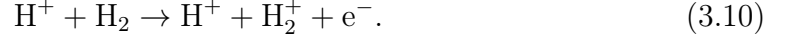
The last process does not have available cross-section data, though below 200 eV values smaller than 10^{-18} cm^2 have been measured. Following this detail I assumed the ionisation cross-section to be energy independent with a constant value of 10^{-18} cm^2. The dominant process is charge exchange across the ion plasma temperature range considered, whereby the proton population converts into H_2^+. In Figure 3.1(b) the solid black line is a collision induced process [80], where

$$H_2^+ + H_2 \rightarrow H^+ + H + H_2.$$ (3.11)

The solid red line is a charge exchange process [80], where

$$H_2^+ + H_2 \rightarrow H_2 + H_2^+.$$ (3.12)

The solid blue line is an ion formation process [87], where

$$H_2^+ + H_2 \rightarrow H_3^+ + H.$$ (3.13)

In Figure 3.1(c) the solid black line is the dissociative proton/charge transfer reaction [80] that producing a slow proton which is composed of multiple channels:

$$H_3^+ + H_2 \rightarrow H + H_2 + H^+ + H$$ (3.14)
$$\rightarrow H_2^+ + H^+ + H_2$$ (3.15)
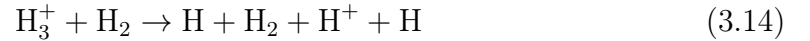
Both channels produce a slow proton, while only one retains the H_3^+ ion though this channel is relatively weak below energies of 30 eV. The dashed black line is the collision induced fast proton [80] which is also composed of multiple channels,

$$H_3^+ + H_2 \rightarrow H^+ + H_2 + H_2$$ (3.16)
$$\rightarrow H^+ + 2H + H_2$$ (3.17)

where the H_3^+ has dissociated into a proton and other neutral products. The solid red line is the collision induced fast H_2^+ process [80], where similarly the H_3^+ has

dissociated into a H_2^+ and a neutral hydrogen atom, i.e.

$$H_3^+ + H_2 \rightarrow H_2^+ + H + H_2. \tag{3.18}$$

This is a gross simplification of both fast ion producing processes as unstable intermediate excited states or composite systems can be formed leading to those end products. The dashed red line is an electron capture process [80]:

$$H_3^+ + H_2 \rightarrow H + H_2 + H_2^+. \tag{3.19}$$

The solid blue line is a proton transfer exchange process [80]:

$$H_3^+ + H_2 \rightarrow H_2 + H + H_2^+. \tag{3.20}$$

The relative errors are the same across all of calculated collision rates, as the only error consider within these calculations is from the vacuum pressure of molecular hydrogen gas. This is why the shaded errors on the log-scale have nearly constant widths. The collision frequencies of each initial ion were summed, assuming they are mutually independent processes, and are shown as green lines in Figure 3.1.

Upon detailed examination of the hydrogen ion cloud's interaction with residual molecular hydrogen gas, we can glean insights into the dominant processes driving the composition dynamics.

As demonstrated in Figure 3.1 (a), the charge exchange process predominates across the entire range of proton temperatures considered. For an initially produced cloud at 10^5 K, the timescales fall within seconds, but these timescales extend to minutes for a cooled proton cloud. This suggests that if a cooled proton cloud is achieved, it could maintain a single ion species for timescales sufficiently long for extraction to a secondary trap.

Figure 3.1 (b) depicts the dual competing processes of H_2^+. While the charge exchange process does not alter the ion composition, the H_3^+ formation process continually depletes its population, resulting in an increasing accumulation of H_3^+.

In contrast, Figure 3.1 (c) presents multiple competing processes across the temperature range considered. At lower temperatures, less than 10^4 K, a proton transfer reaction primarily governs the collisions, gradually depleting the H_3^+ population into H_2^+. At higher temperatures, both H^+ and H_2^+ ions can be generated via an endothermic reaction, acting simultaneously as a heat source and a channel for depleting the H_3^+ population.

In summary, a hydrogen ion cloud at high temperatures will exhibit dynamic composition changes. These changes act as a heat source, further accelerating the rate of dynamics. On the other hand, at low temperatures, the proton population remains relatively stable. However, the H_2^+ population will continually deplete into H_3^+, and

the H_3^+ population will slowly decrease into the H_2^+ population. These shifts lead to a net increase in the H_3^+ population and a net decrease in the H_2^+ population.

3.4   Proton source for ALPHA Experiment

The main limitation for the proton source is to not disturb present vacuum conditions in ALPHA apparatus. A vacuum quality of below 10^{-9} mbar within the Penning traps is essential for long lifetimes of trapped plasma, where a poor vacuum quality can introduce drag forces that lead to radial expansion. Ultra-high vacuum (UHV) conditions are also essential for storing antimatter particles. Therefore, a source that operates on injected gas must be separated from the primary UHV volume with a stage or multiple stages of differential pumping. Depending upon the size of such systems, physical space can become a concern. Ideally the residual gas composition of the Penning trap should be left unchanged, as increasing vacuum pressure would cause the annihilation rates to increase leading to reduced antiproton lifetime.

Protons loaded into the ALPHA trap can be confined in the same manner as antiprotons, but with opposite electric potentials. Similarly, plasma manipulation techniques like rotating wall compression, sympathetic cooling, and the same diagnostics methods can be applied. A proton source could benefit further low energy plasma study, during the periods when antiproton beam is not available due to CERN's accelerators shut downs. Proton plasma could serve as a mock-up for antiproton plasma to study particles transport and develop non-destructive diagnostic methods based on the plasma modes dynamics. Although one should be careful, since results with protons might not be directly translatable to antiprotons, by only reversing the instrument electric potentials. For example, the voltage applied to the electrodes of the Penning trap may have an offset that would contribute in an opposite manner when comparing differently signed electrical charged particles. Another possible issue can arise when analysing measurements from one of the available MCPs, due to the fact that the magnitude of electron amplification is dependent on the species that are measured and this affects the gain of the device. Additionally a technical flaw in the assembly of the MCPs exist, which is a positively biased electric field emanating from multiple points outside of the active surface (high voltage tabs that connect the MCP plates to the voltage source). This generates a non-symmetric distortion of imaged particles and can produce a radial electrostatic aperture that acts as a potential barrier for particles approaching MCP at trajectories further away from the trap axis.

3.5   Conclusion

The residual gas within the ALPHA traps consists mainly of molecular hydrogen. A potential electron impact process could result in a variety of hydrogen ion species, driven by a trapped electron plasma of 10^8.

Electrons with kinetic energies sufficient to ionise hydrogen molecules were obtained by increasing their axial kinetic energy. This increase was achieved by applying white noise to one of the Penning trap electrodes.

The initial concept was to generate anion hydrogen, which possesses a charge-to-mass ratio remarkably similar to that of the antiproton. This approach could be used to commission particle-transfer and plasma diagnostic techniques during periods when antiprotons are unavailable at CERN.

However, studies conducted in the Catching Trap showed no indication of anion hydrogen production. Given the temperatures of molecular hydrogen present under the cryogenic conditions of the Catching Trap, the expected production cross section for anion hydrogen is practically too small to generate a significant number of ions or to be detected by existing diagnostic instruments. However, this unsuccessful study led to an alternative idea: the generation and isolation of protons that could be used to develop plasma temperature diagnostic techniques through passive detection of electrostatic plasma modes [88, 89] and to produce hydrogen within the ALPHA apparatus.

The electron impact ionisation process is anticipated to primarily produce H^+, H_2^+, and H_3^+. Isolating H^+ from the mixed positive hydrogen plasma can be achieved using the autoresonance technique, which will be discussed in Chapter 5. The initial step in this study will involve the production of a reproducible mixed positive ions plasma, in which the species composition remains consistent. As positive hydrogen ions could ionise the residual gas via proton impact ionisation, akin to electrons, the trapped plasma of positive hydrogen ions needs to be cooled to temperatures below 10^4 K. The forthcoming chapter will delve into positive ion production and sympathetic cooling using positrons.

PRODUCTION OF POSITIVE HYDROGEN IONS

This chapter presents a study on positive-ion production within the Catching Trap apparatus, which is based on methods developed during a previous unsuccessful anion-hydrogen study mentioned in Chapter 3. The earlier study found that when a constant power spectral density (white-noise) signal was applied to one of the electrodes involved in trapping an electron plasma with roughly 10^8 electrons, excessive amounts of electrons were generated. Within 2 minutes of continuously applying white-noise, the electron population increased to 10^9 electrons, indicating significant ionisation and positive ion production within the trap.

The current study serves as a preliminary step towards developing a proton production scheme within the ALPHA apparatus. The chapter focuses on three essential steps:

1. The first step presents a method for producing positive ions by inducing electron impact ionisation of residual gas through driven electron motion within a trapped electron plasma. This chapter will demonstrate that tuning systematic parameters was necessary to achieve practical cycle times. Long-term measurements of cycle times for producing a specific quantity of positive ions reveal the stability of the degraded vacuum quality, which is necessary for long term operation without repetitive calibrations.

2. The second step involves introducing positrons into the positive ion plasma to adjust the mixture's shape and temperature.

3. The third step identifies the species present within the positive ion plasma by conducting time-of-flight measurements. This is done by releasing the trapped mixed plasma from the Catching Trap and simultaneously measuring the time of arrival for all species.

This study had many alternative solutions attempted for each individual step,

and therefore only the noteworthy and eventual solutions will be discussed.

4.1 Ion production

The trapping and manipulation of charged particles within the Penning trap are conducted using the programmatic method described in Section 2.1.7. This method involves writing experiments as sequential actions in multiple files, which are then read out and executed by National Instruments hardware. Sequentially altering the applied voltages on each electrode of the entire trap enables the trapping of charged particles injected into the inner volume of the electrodes This manipulation of electrode voltages is used to axially guide the plasma.

Electrons were injected into the Catching Trap by an electron-gun and then trapped using the previously described suck load method, see Section 2.3.1. The number of electrons suck loaded into the trap was tuned to 1.3×10^8 electrons, with the number of electrons measured by ejecting the electrons onto the antiproton degrader foil, see Section 2.5.1 for further details of Faraday Cup measurements. The precise number of electrons loaded did not significantly impact the ionisation rates, as secondary electrons produced were trapped and accumulated within the initial electron load, resulting in a steady-state space-charge limited electron population. The electric potentials that trapped the electrons were adjusted to create potential wells suitable for trapping positively-charged particles, as shown in Figure 4.1. The initial radial
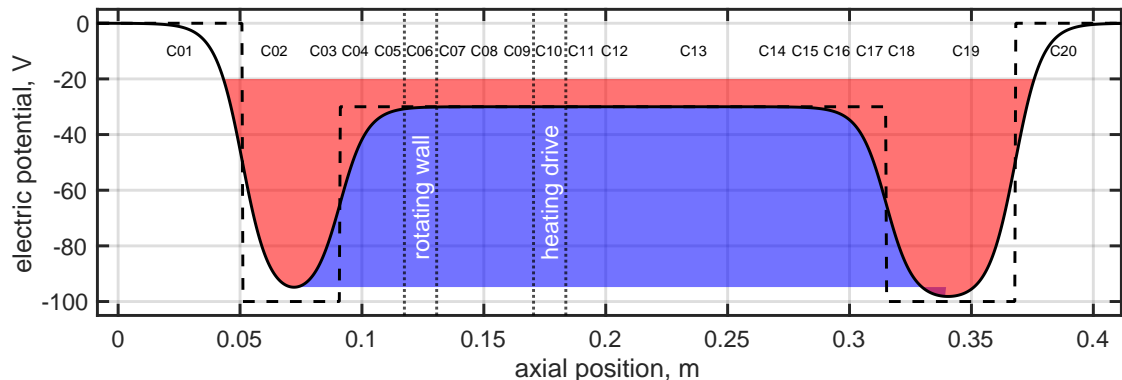
Figure 4.1: The electrostatic potential well used for producing and trapping positive ions, space-charge is neglected. The on-axis electric potential and the applied electric potential are given by a black solid line and a black dashed line respectively. The red region indicates the axial extent for trapping positive ions and the blue region indicates the trapping region of the heated electrons, the coloured regions are not accurate depictions of the energies involved.

size of the loaded electrons was large compared to the detection region of the MCP diagnostic. When the electron population was heated, it would radially expand. The rotating wall compression method, described in Section 2.2.1, was employed

to reduce the electron population's radial size. Additionally, it reduced the radial extent of the ion production region.

Radio frequency signals were injected into the Penning trap via a high-pass filter connected to each electrode. A high-pass filter superimposes the trap DC electric field with a radio frequency signal. The electron's axial motion can be driven by applying oscillatory signals onto a single electrode involved in the electric well that traps the electron. Radio frequency signals was produced by a SRS DS345 waveform generator. This device was placed externally to the trap and was connected via a high-pass filter to a feed through connection of a single trap electrode. The electrode used during the final configuration was electrode C10, as indicated in Figure 4.1. The injected signal can increases the axial motion of the electrons, leading to a higher frequency of ionizing collisions between electrons and residual gas. This waveform generator signal is referred to as the 'heating drive'.

The experimental sequence for ion generation is shown in Figure 4.2, the sequence steps are:

1. Trap electrons within a nested potential well surrounded by a positive ion potential well and apply rotating wall signal

2. Apply heating drive (positive ions will be trapped in surrounding well)

3. Eject electrons by smoothly and linearly changing electron trap well depth to zero

4. Axially shorten the positive ion potential well (increase trapping effectiveness of ions by increasing axial bounce frequencies)

5. Axially shorten the positive ion potential well and reduce the well depth

The trap electric potentials were static during the duration of the heating drive. The last step reduces the positive ion trap to two electrodes and was seen to improve the survival of the ions.

In the previous anion-hydrogen study 10^8 electrons were heated using the same hardware configuration, with the DS345, to cause electron production due to electron impact ionisation producing secondary electrons. By extending the axial length of the electric potential trap, the rate of electron production was observed to increase. This can be explained in a few steps: When the electrons are spread across a larger electric well volume, the electron density decreases, resulting in a decrease in the frequency of electron-electron scattering. This reduced scattering rate, in turn, increases the electron thermalisation time scale, causing the electrons accelerated by the electronic drive to undergo more collisions with the residual gas. This observation is why nearly every electrode of the Catching Trap is involved in the positive ion generation sequence.
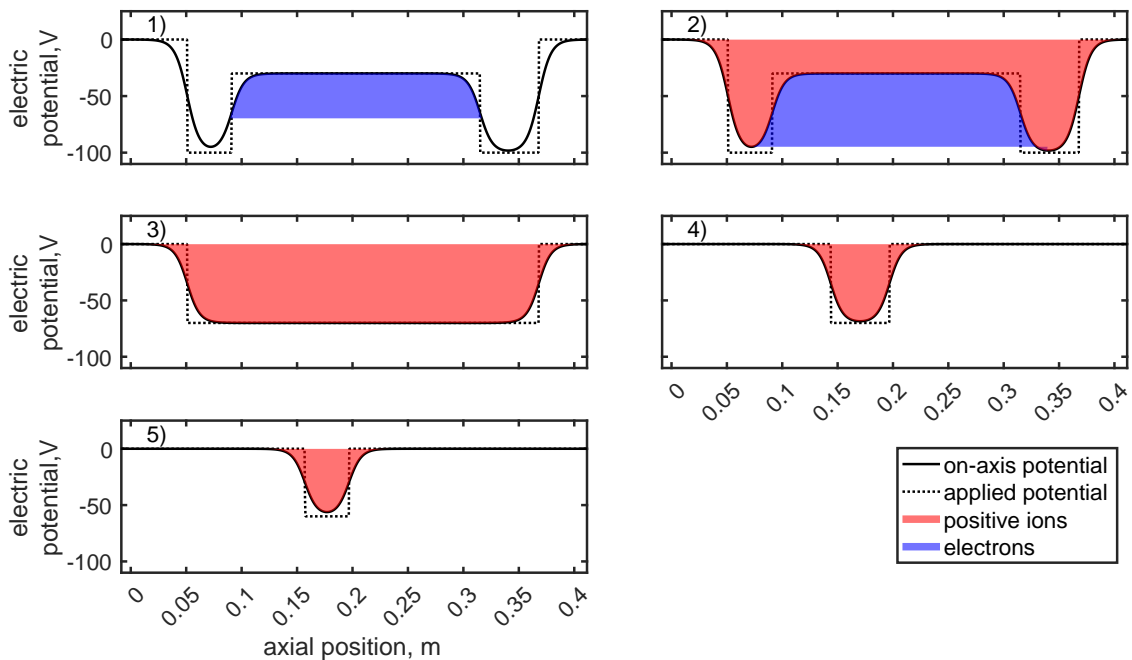
Figure 4.2: The Catching Trap electric potential sequence for generating positive ions. (1) Electron well depth: 70 V & positive ion well depth: 100 V. (2) Electron well depth: 70 V & positive ion well depth: 100 V. (3) Electron well depth: 0 V & positive ion well depth: 70 V. (4) Positive ion well depth: 70 V. (5) Positive ion well depth: 60 V.

During the experiment, a rotating wall compression was applied to the electrons in the trap by using a 1 MHz dipole mode at 0.5 V_{pp} as the rotating wall signal. Different rotating wall signals were also examined. The objective was to find a signal that could maintain a constant electron plasma radius for several minutes, have a plasma radius within the detection range of the MCP diagnostic, and cause minimal interference with the electron temperature.

After applying a heating drive for several minutes, the chosen rotating wall signal compressed the electron plasma radius to within 0.90-0.96 mm. To determine the best ion generation sequence, various factors were tested, such as different electron potential well depths, positive ion well depths, heating drive electrode positions, heating drive amplitude, and heating drive signal type. The performance of each sequence was measured by the positive ion production rate, which was determined by dividing the number of positive ions measured with a Faraday Cup (antiproton degrader foil) by the duration of the heating drive. The sequence with the highest positive ion production rate was selected, but further improvements could be made with more time for development.

Different signal types were studied to enhance the positive ion production rate, including fixed frequency, frequency sweep, and white-noise signals. Positive ion generation was not observed for signals below 1 MHz, but it was detected for signals

above 1 MHz. All three signal types produced positive ions at different rates, with the white-noise signal yielding the best results, surpassing the best frequency sweep signal by over 45%. The frequency sweep signal offered a range of configurable parameters, such as start and stop frequencies, sweep style, sweep rate, non-linear sweep rate, and waveform type.

Ion generation was observed for sweep rates of 100 Hz, 10 Hz, and 1 Hz, but not for sweep rates greater than 1 kHz. A triangular sweep style yielded 10% better results than a sawtooth sweep style, and there was no noticeable difference between using either sinusoidal or square waveforms. The white-noise signal was chosen as the heating drive for the rest of the study, although it is unclear why it was the optimal configuration. One possibility is that its composition of a spectrum of frequency components allows it to resonate with a larger number of electrons.

Figure 4.3 displays a collection of positive ion measurements with varied parameters. Positive ions were measured using the Catching Trap Faraday Cup. Although the heating drive duration stays constant in these measurements, the absolute values are not critical since the production rates vary according to the vacuum quality. Nevertheless, the relative response of the positive ion production rate to different parameter adjustments remained consistent over several days. Data for each parameter scan was gathered within a timeframe of tens of minutes. Baseline measurements were repeatedly taken during this period, no significant variations in production rates were observed in these baseline measurements. The finalised electric well con-
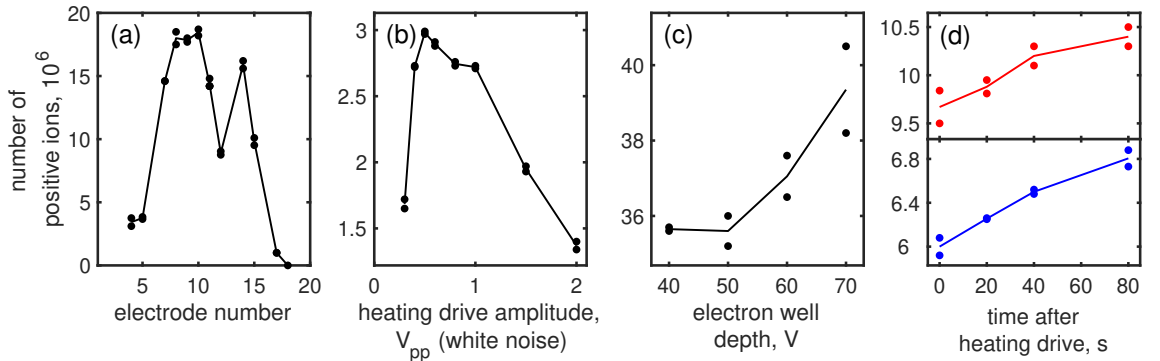
Figure 4.3: A collection of positive ion measures of various systematic scans to optimise the production of positive ions. The solid lines connect the mean value at each parameter value and are meant to only highlight trends. (a) The heating drive connected to each trap electrode individually. (b) The amplitude of the heating drive. (c) Electron potential well depth. (d) Hold time after the heating drive was turned off. The blue and red data have initial ion populations of 6×10^6 and 1×10^7 respectively.

figuration used during the positive ion generation sequence is shown in Figure 4.1. Positive ions are produced within the electron well volume, between electrodes C03 and C18, where the positive ion well depth is 30 V. The positive ions are expected to travel throughout the extended volume between electrodes C02 and C19 because of

the absence of a cooling mechanism within the two 70 V deep side wells, C02 to C03 and C18 to C19. Figure 4.3(c) shows a scan of the electron well depth. When the electron well depth was increased beyond a certain threshold, the number of positive ion produced started to increase, but fluctuations in the number of produced ions became more pronounced with increased well depths. The heating drive's position relative to the trap electric potentials was also considered, as shown in Figure 4.3 (a). Here, the heating drive was connected to one of twelve different electrodes. The optimal electrode positions are C08, C09, and C10, while the least effective positions are the electrodes at the end of the electron electric potential well. Electrode C13, one of the two specialised high-voltage electrodes, caused the heating drive to perform worse compared to neighbouring electrodes. The largest average number of produced positive ions was observed when using electrode C10, which is why it was chosen as the optimal heating drive position.

The production of positive ions does not consistently increase with the heating drive amplitude. Instead, there is a sharp increase to a peak value at 0.5 V_{pp}, after which it steadily decreases, as shown in Figure 4.3(b). The reason for this peak in production has not been investigated. One possible explanation is that the heating becomes significant compared to the cyclotron cooling rate of the electrons, which could then lead to electrons evaporating from the trap.

Positive ion production continued after the heating drive was powered off. This is shown in Figure 4.3(d) for positive ions held within the potential well shown in Figure 4.2 5). Positive ion production was observed up to 80 s after the heating drive was powered off, and measured with two different initial population sizes, 6×10^6 and 1×10^7 ions. The positive ion population was observed to increase by (0.25-0.50)% s^{-1}, and this rate began to decrease by 40 s.

While the heating drive is active, the rate of positive ions generated is expected to be proportional to the number of electrons loaded into the trap. As the ionisation process produces both positive ions and electrons, the electron population increases, contributing to further ionisation events. The positive ion production rate is expected to rise exponentially if no competing mechanisms reduce the ionisation rate or cause the loss of positive ions or electrons. However, basic population growth models can account for mechanisms that limit population size.

In ecology, population growth is often modelled using logistic equations, which include a growth factor (analogous to our ionisation rate), κ, and a carrying capacity (analogous to our space charge-limited capacity for the ion well, positive ion loss mechanisms, or mechanisms that suppress the ionisation rate), N_{max}^{ion}. A crudely applied logistic differential equation can be written as follows:

$$\frac{dN^{electron}}{dt} = \kappa N^{electron}(t) \left[1 - \frac{N^{electron}}{N_{max}^{ion}}\right]. \tag{4.1}$$

The solution to this equation is:

$$N^{\text{electron}}(t) = \frac{N_0^{\text{electron}} N_{max}^{\text{ion}} \exp\left(\kappa t\right)}{N_0^{\text{electron}} \left[\exp\left(\kappa t\right) - 1\right] + N_{max}^{\text{ion}}}, \tag{4.2}$$

where N^{electron} and N_0^{electron} are the number of electrons at a later time $t > 0$ and at the initial time $t = 0$ respectively. κ is the electron and ion generation rate due to a single heated electron. It is assumed that the number of ions generated, denoted N^{ion}, is equal to the number of newly generated electrons, which is justified by conservation of charge. The positive ion population can be expressed as:

$$N^{\text{ions}}(t) = N^{\text{electron}}(t) - N_0^{\text{electron}} \tag{4.3}$$

$$= N_0^{\text{electron}} \left[\frac{N_{max}^{\text{ion}} \exp\left(\kappa t\right)}{N_0^{\text{electron}} \left[\exp\left(\kappa t\right) - 1\right] + N_{max}^{\text{ion}}} - 1 \right]. \tag{4.4}$$

The number of positive ions generated for various heating drive durations is displayed as black dots in Figure 4.4. Each duration includes two samples. Measurements were taken for durations from 10 to 90 s over a 40-minute span, while the 120 s duration was measured two hours after the last measurement in that set. This delay raises concerns about potential fluctuations in vacuum quality between separate measurements.

An alternative form of Equation 4.4 is the limiting case for N_{max}^{ion} tending to infinity:

$$N^{\text{ions}}(t) = N_0^{\text{electron}} \left[\exp\left(\kappa t\right) - 1\right]. \tag{4.5}$$

This equation describes an exponentially growing population with no upper limit. Upon inspection, it was found that Equation 4.5 fits the measurements from 10 s to 90 s, excluding the 120 s data points. This fit is shown as a blue curve in Figure 4.4.

The fit coefficients N_0^{electron} and κ errors are from least-square fitting errors. The fit value of N_0^{electron} is $(4.7 \pm 0.2) \times 10^6$, a fraction of the initially loaded 1.3×10^8 electrons. This is somewhat expected, as the heating drive only encompassing a fraction of the total electron well. The fit value of κ is $(3.03 \pm 0.04) \times 10^{-2}$ Hz, this value is likely related to the present vacuum quality. This suggests that the ionisation rate per one electron is approximately 30 mHz. This fit will not perform well if the 120 s measurements are included.

Alternative, Equation 4.4 was fit to all of the data and is shown as a red curve in Figure 4.4. This fit performs well across all measured durations. The fit values of N_0^{electron} and κ are $(2.4 \pm 0.7) \times 10^6$ and $(4.4 \pm 0.4) \times 10^{-2}$ respectively,. This values are roughly similar to the previous fit, though the discrepancy could be due to the 90 s duration measurements exhibiting non-exponential growth. However, with this fit, the maximum number of trapped positive ions N_{max}^{ion} is predicted to be

$(158 \pm 13) \times 10^6$. Both fits have good R^2 values of 0.9995 and 0.99997 for the first and second respectively.

Since the data was collected over a 2-hour period and the fitted curves seem appropriate, it could be suggested that the electron ionisation rate remains relatively constant over time spans ranging from minutes to hours. However, the choice to use a logistic differential equation was based on intuition rather than a systematic process, so this analysis should not be considered a definitive explanation.
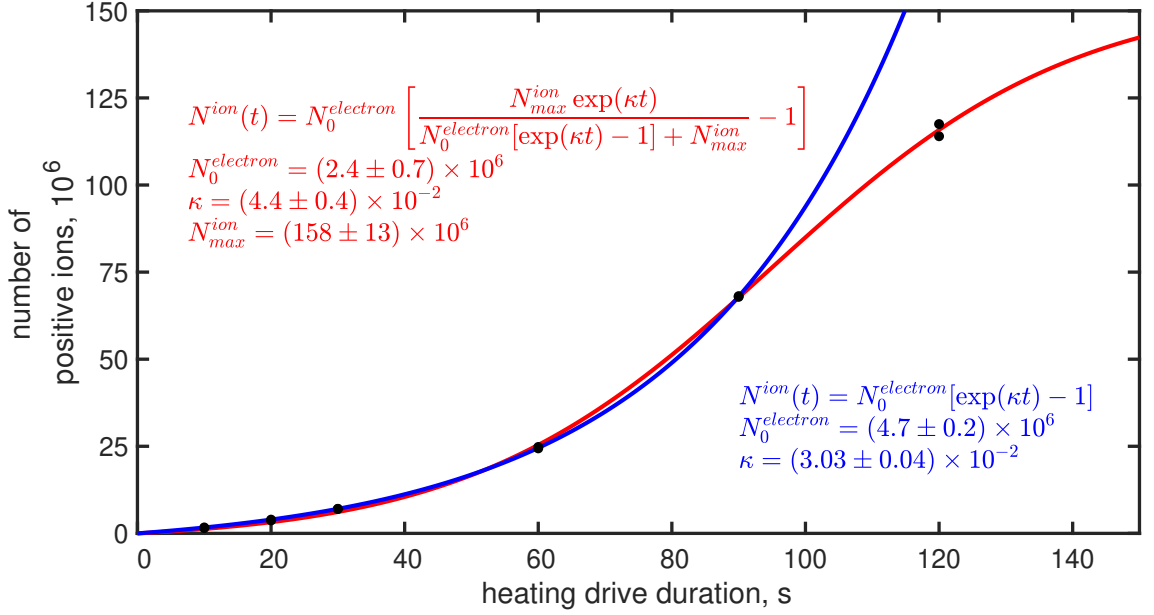
Figure 4.4: The number of positive ions produced versus the duration of the heating drive. The red line (Equation 4.4) and blue line (Equation 4.5) fits shown in the top left corner and bottom right corner respectively. The blue curve excludes the 120 s data points and the red curve is fitted to all data points.

The Catching Trap's UHV quality degrades over time resulting in decreased antiproton lifetimes within one week. Over longer periods positive ion generation is observed in high-gain MCP measurements. This degradation occurs due to the accumulation of absorbed gas layers, which cause the cryogenic trap's pump rate to decrease over time.

For experiments that require antiprotons, this degradation is mitigated by periodically thermal cycling the trap, effectively 'cleaning' the cold surfaces of adsorbed gases. The trap is cooled using a cryo-head compressor, and any disruption to its electrical power supply causes the surfaces to heat up. This can occur intentionally by powering off the compressor or unexpectedly due to a power cut.

Positive ion generation rates relevant in this study are on the order of 10^5 ions s^{-1}, which takes place within months if the trap is not thermal cycled. The Catching Trap was designed to operate at cryogenic temperatures and within an UHV environment, limiting the present study from operating in a non-cryogenic mode. As a result, there was a need for a method to quickly degrade the cryopumping speed.

This could be achieved by exposing the cold trap to higher vacuum pressures for a certain duration, leading to the method used in this study.

The Catching Trap UHV volume was isolated from the remaining ALPHA-2 and ALPHA-g apparatus UHV volumes by closing a gate valve. Then, the Catching Trap's UHV ion pump was powered off while the system remained cold and cryopumping. From imitial attempts, it was not clear how long this process needed to be carried out. It was also uncertain whether a steady-state vacuum could be achieved, which would enable consistent positive ion production. During the first positive ion run, the Catching Trap UHV ion pump was powered off at the end of the workday and powered on at the beginning of the following workday. The period
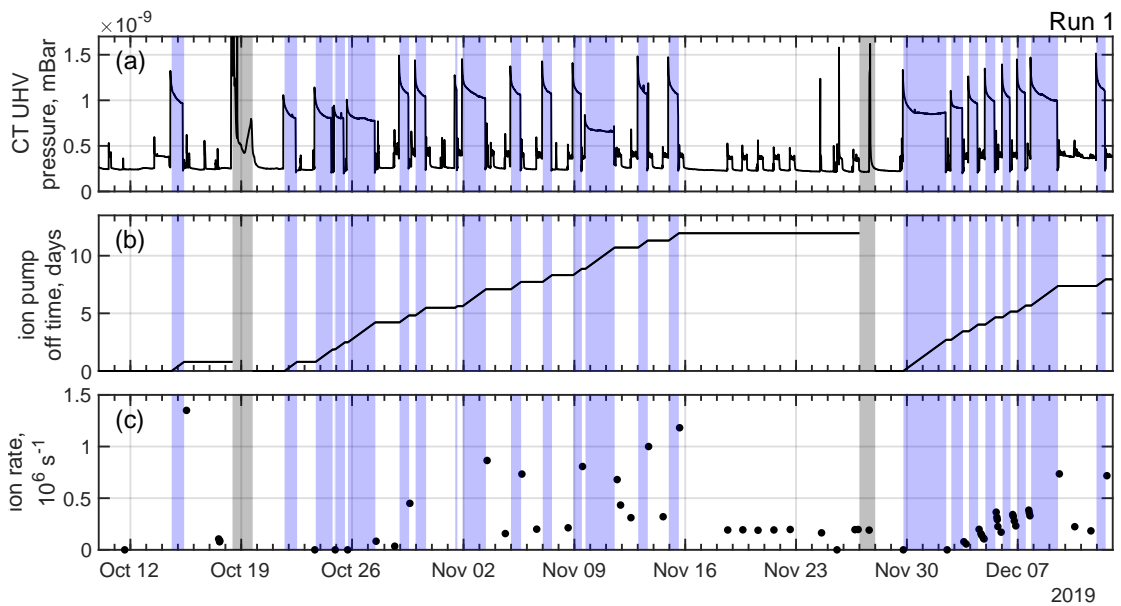
Figure 4.5: These three plots show information from across the first positive ion run, ranging from 10th of October until 13th of December 2019. The blue bands indicate when the Catching Trap UHV ion pump was intentionally turned off. The grey bands indicate unexpected power cuts occurred. (a) Catching Trap UHV pressure. (b) Cumulative duration that the ion pump was turned off, and reset to zero after unexpected power cuts. (c) Positive ion generation rate baseline as black dots.

when the UHV ion pump was intentionally powered off are shown as blue bands in Figure 4.5. When ion pump is off, the trap pressure increases, as shown in Figure 4.5(a). The vacuum gauge, a cold-cathode positioned downstream from the Penning trap, indicates this increase. After turning the ion pump back on, the positive ion production rate increased significantly but continually decreased to levels similar to initial production rates. This trend can be seen in Figure 4.5(c), where the initial positive ion production rates after each ion pump off period are consistently high and decrease monotonically until the next ion pump off period. Grey bands indicate power failures in the facility, causing unintentional trap thermal cycles. Figure 4.5(b) shows the cumulative ion pump off duration since the previous thermal cycle.

The positive ion generation rate would decrease by an order of magnitude after 8 hours. At the beginning of the daily shift, hundreds of millions of ions could be produced within one minute, but by the end, it might take two minutes to produce 10^7. The heating drive duration needed to be recalibrated multiple times a day to obtain consistent positive ion loads. A workday might have to end early due impractically low positive ion rates, after which the ion pump would be manually powered off. After 12 cumulative days with the ion pumps powered off, a steady-state positive
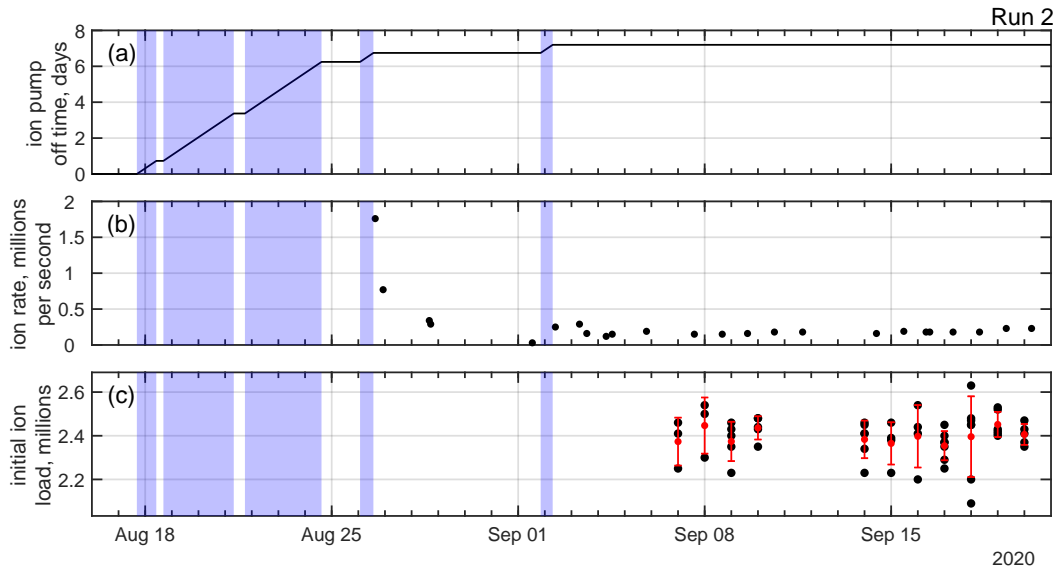
Figure 4.6: These three plots show information from across the second positive ion run, ranging from 16th of August until 20th of September 2020. The blue bands indicate when the Catching Trap UHV ion was turned off. (a) is the total duration the ion pump has been turned off. (b) shows the ion generation rate of a baseline as black dots. (c) is the number of ions generated using a common daily calibrated heating time, aiming for 2.4×10^6 ions. The black dots are individual ion generation measurements, with the mean value indicated by red dots and the statistical standard deviation shown as red lines.

ion rate of $(1.9 \pm 0.1) \times 10^5$ positive ions produced per second was observed, as shown in Figure 4.5 (b) and (c) from November 16th onwards. This condition was lost due to an unexpected power failure. Consequently, a different approach was adopted during the second positive ion run in August and September of 2020, with the ion pump being turned for longer durations, also indicated as blue bands in Figure 4.6. This second run required a cumulative ion pump off duration of 7 days 5 hours before achieving a steady-state positive ion rate. The aim during the second run was to achieve an initial positive ion load of 2.4×10^6. Figure 4.6(c) shows fluctuations of up to 1.85×10^5 positive ions from the targeted 2.4×10^6 ions. On the last day of the second run, September 20th, one of the smallest fluctuations of 4.8×10^4 positive ions was observed. The reason for the decrease in fluctuations is unknown. The autoresonance amplitude and start frequency measurements shown in Sections 5.4 and 5.5 were collected on September the 19th and 20th. These small

initial positive ion population fluctuation are ideal for systematic studies.

A significant issue with this method of generating positive ions is the observed hysteresis behaviour in the positive ion production rate. The heating drive duration for producing the target number of positive ions varies daily, this duration is scanned to determine the optimal value. However, the duration and time delay between successive positive ion generation experiments affect the production rate, resulting in apparent inconsistencies between heating drive duration and the number of positive ions generated. This issue was present throughout the first study, and a potential solution was discovered during the second study.

The hysteresis behaviour was eliminated by using clearing voltages, a procedure that employs the trap electrodes to create electric fields that remove stray charged particles. Images captured by the Catching Trap MCP of the positive ions soon after the heating drive ended appeared diffusive, suggesting that the ion population was distributed over a wide radial range.

4.2 Initial positive ion temperatures

A reliable calibration for the temperature diagnostic of positive ions proved to be challenging. The first and second positive ion runs used different potential well manipulations for the temperature diagnostic. In, the first run, the temperature diagnostic was determined by searching for an appropriate exponentially increasing signal, as expected from these measurements, see Section 2.5.2. In contrast, the second run additionally utilised positrons to identify suitable potential well manipulations. This approached assumed that all components of a mixture of positive ions and positrons are in thermal equilibrium, with the lightest component (positrons) being the majority of the initially extracted particles. If all components of a positive
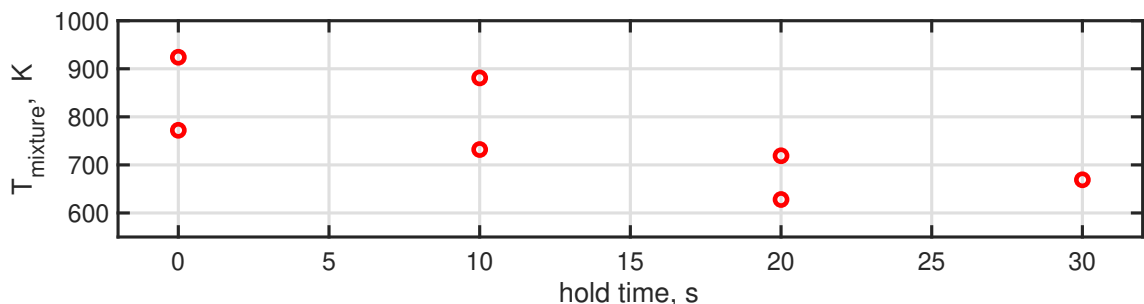
Figure 4.7: Temperature evolution of positive ion and positron mixture trapped in a static potential well.

ion and positron mixture reach thermal equilibrium, then the temperature diagnostic measurement will correspond to the mixture temperature. Since positrons will undergo cyclotron cooling, It is expected that they would sympathetically cool the mixture, resulting in a decreasing temperature with increasing hold times. The po-

tential well manipulations involved in the temperature diagnostic were repeatedly adjusted until this cooling effect was observed in the mixture, as shown in Figure 4.7. The corresponding temperature diagnostic configuration was then applied to positive ions without positrons, as only the MCP gain needed to be increased for the comparatively weaker ion signal.

This change in temperature diagnostic configuration means that temperature measurements of similar positive ion populations are not consistent across the two runs. During this second run, the initial temperature of the 2.4×10^6 positive ions was measured to be $(3.2 \pm 0.4) \times 10^5$ K.

4.3 Catching Positrons

The positive ions generated maintain a high temperature of $(3.2 \pm 0.4) \times 10^5$ K, due to the lack of efficient cooling mechanisms, see Section 2.4. Evaporative cooling was not used because it decreases the population size and leads to radial expansion. To address this issue, positrons were introduced to sympathetically cool the positive ions, as demonstrated in the prior Section 4.2. In the presence of the 3 T magnetic field generated by the Catching Trap's solenoid magnet, cyclotron radiation of positrons is significant. The time it takes for a positron to reduce its kinetic energy by a factor of e (Euler number) is 287 ms, known as the e-folding time.

To implement this solution, positrons were first transferred to the ALPHA-2 trap. Inside the ALPHA-2 trap, the rotating wall method was used to compress the positrons radially, counteracting the radial expansion that occurred during the initial transfer. Once prepared, the positrons were moved from the ALPHA-2 trap to the Catching Trap. This two-step transfer process was necessary due to the substantial losses experienced when transporting positrons directly from the positron accumulator to the Catching Trap. Positrons were moved from the ALPHA-2 trap to the Catching Trap with an ejection energy of 90 eV.

The groups of positrons transferred between Penning traps are called bunches. These bunches have a specific physical distribution that can change during transit. The positron bunch's full-width-half-maximum in the Catching Trap was measured to range between 497-525 ns, corresponding to a physical positron bunch length of 280-295 cm. This length is significantly longer than the electrode stack, so the maximum trap length (C02-C20) was used. The axial distance between the centers of electrodes C02 and C20 is 36 cm (see Figure 4.1). Accounting for the positron bunch's reflection onto itself, the maximum bunch length that can be trapped is 72 cm. Consequently, the maximum percentage of the positron population transferred from ALPHA-2 to the Catching Trap is estimated to be between 24.6-25.9%.

The experimental sequence for capturing positrons within a nested positive ion potential well is shown in Figure 4.8. The sequence steps are as follows:
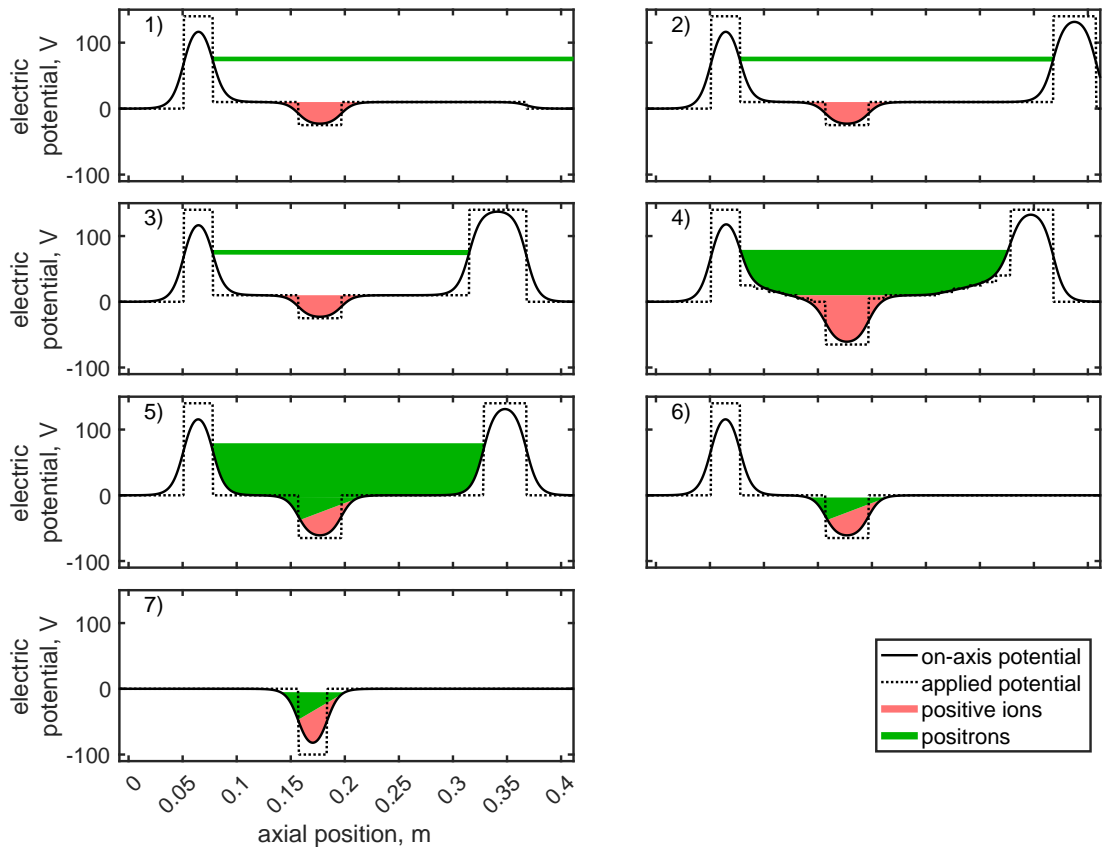
Figure 4.8: The Catching Trap electric potential sequence for catching positrons with a nested positive ion well. (1) Inject positrons into the Catching Trap. (2) Trap in the positrons. (3) Change trapping to electrically quieter electrodes. (4) Bias electric fields to guide positrons towards the nested positive ions and wait 12 seconds. (5) Ground interior electrodes. (6) Release 'hot' positrons. (7) Ground remaining unnecessary electrodes.

1. Incoming positrons are axially reflected by a 140 V barrier on C02, and a 10 V electric potential plateau is created by the remaining trap electrodes.

2. The high-voltage switch on electrode C20 is raised to axially trap the positrons. The trapping electrode is changed from C20 to C18 and C19, due to the lack of an electrical filter on the high-voltage electrode C20 causing electrical noise to couple into the trap.

3. The inner trap electrodes are biased to generate an electric field directed inwards to the nested positive ion well. This is held for 12 seconds as positrons cyclotron radiate and mix with positive ions.

4. The inner trap electrodes are grounded.

5. The trapping electrodes C18 and C19 are grounded to release 'hot' positrons from the Penning trap volume, a process referred to as a 'hot dump.'

6. The remaining potential barrier is grounded, increasing the positron-ion well depth and reducing the well axial length from three electrodes to two electrodes.

The catching efficiency was measured as the number of positrons caught from this sequence relative to the total number of positrons ejected from the ALPHA-2 trap towards the Catching Trap. The total number of positrons transferred was measured by grounding all Catching Trap electrodes and measuring the number of positrons on the antiproton degrader foil, as a Faraday Cup. A catching efficiency of $6 \pm 1\%$ was obtained, which is poor compared to the previous estimate. This poor performance is not understood. Lower positron ejection energies were measured to have longer bunch lengths. Therefore, the shorter bunch length, with positron ejection energy of 90 eV, was used throughout this study. The fast switching power supply on C20 raises a positive high voltage from ground to the target voltage within nanoseconds. Both catching electric potentials are the maximum, $+140$ V, outputs of the electrode power supplies. This value was chosen as it ensures the axial electric potentials are greater than the positron ejection energy. The trapping efficiency was optimised by scanning the delay time between ejecting the positrons towards the Catching Trap and triggering the fast switching power supply. A plateau of positively biased electrodes were used to further aid the trapping by reducing the positron bunch kinetic energy, and hence reduce the positron bunch length. A bias of 10 V was chosen as it improved the mean number of positrons caught by 10% compared to no bias. The plateau bias was not closely studied, as a value closer to the positron ejection energy is expected to produce greater catching efficiencies.

The inclusion of a nested well within the catching potentials changed the performance of catching positrons. If no positive ions were loaded into the nested well, a negligible quantity of positrons were caught. Similarly, if positive ions were loaded and the nested well depth was greater than 50 V, then the positron catching efficiency would greatly reduce. This meant that the well depth of the nested well had to be calibrated for the chosen initial positive ion load. The nested well depth could not be too shallow otherwise positive ions would be unintentionally ejected from the trap, restricting any well depth scans to be greater than a space charge limited one. The space charge limited well depth is dependent upon the number of electrodes involved in the nested well, the more electrodes the shallower the well depth could be. For 2.4×10^6 positive ions a 35 V deep three electrode well on C09, C10 and C11 was optimal, and the well depth was optimised within 5 V. Alternative positron catching sequences without a nested well had similar catching efficiencies to the optimal sequences with a nested well. Since the space charge of a plasma distributes itself axially to minimise the axial electric field, then a space charge limited nested well will appear to be shielded from the captured positrons.

During the catching sequence, the positrons are cooled and axially centered onto the nested well position. The depth of the nested well is increased from its initially space-charge limited depth, due to the presence of positive ions, to a greater depth that allow the caught positrons to also occupy the nested well. It has been found that both the action of the axially inward electric fields and their duration are important for improving the catching efficiency. Without this waiting period, the resulting MCP images of the positrons were sparse and exhibited annular density and shape. The annular shape can be attributed to various apparatus errors, such as a misalignment between the Catching Trap solenoid magnet axis and the Penning trap axis, causing segments of the bunch to be caught off axis. A potential solution to this problem is simply to wait, as the positrons will experience diocotron damping, a process also observed in electrons captured by the TITAN experiment [90]. During this waiting period, the positrons will move radially inward toward the trap axis and cool down due to cyclotron radiation. The necessary waiting time was empirically determined. For instance, in cases where positrons are captured without any nested positive ions, a waiting time of 6 seconds has proven sufficient. However, when 2.4 million nested positive ions are present, the positrons were observed to form a dense annulus instead of being dispersed after a 6-second wait. After waiting for 12 seconds, the positrons and positive ion mixture aligned with the trap axis, showing no annular features. The diocotron damping also appeared to cause a radial compression of the initial positive ions sympathetically. This led to an increase in positive ion density and a reduction in their radial size, as evidenced by MCP images. As a result, a 12-second waiting time was employed for the rest of the study.

After the 12 s cooling period is completed, the downstream potential barrier is grounded. This ejects 'hot' particles that have not been trapped inside the deepened nested well. These ejected particles can be imaged on the MCP since the 12 s wait is sufficient time for voltage ramping of the MCP instrument power supply. Imaging this step validates its performance by demonstrating minimal particle loss, which is helping when examining the cooling time. The remaining population in the trap consists of mixed species within a single potential well. An MCP image of the resulting mixture can be seen in Figure 4.9 (a). Positrons and positive ions are observed at separate locations on the MCP and the positive ions appear elliptical, an explanation for this separation and distortion is provided in Section 4.4. This elliptical shape of the positive ions is thought to be an consequence of the MCP device. It is currently unknown if this distortion is a reshaping of the their radial distribution or a process that clips the profile, similar to an aperture.

To obtain information from this radial distribution an assumption had to be made. The semimajor axis of the positive ions elliptical shape appears to be of similar length positron plasma radius. Therefore, the positive ions are assumed to have been distorted along one axis parallel to the plane of the MCP front surface, which
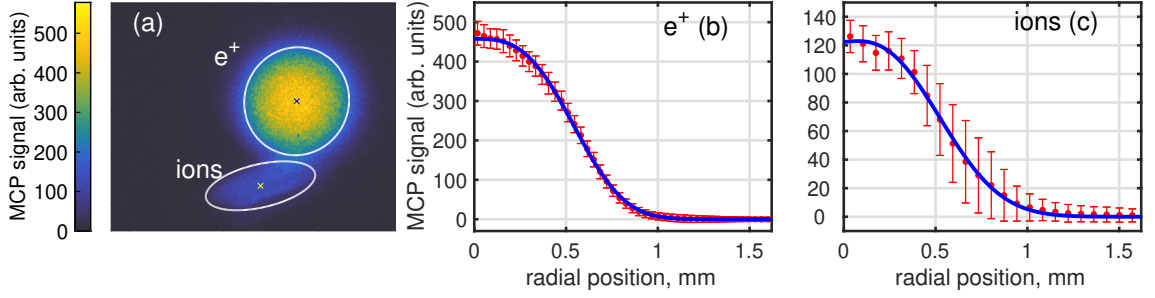
Figure 4.9: (a) A MCP image of positrons caught within 2.4×10^6 positive ions, using the sequence shown in Figure 4.8. The white circle and ellipse are identified components of the ejected mixture. Azimuthal average pixel intensities with respect to a scaled distance from the component center for positrons (b) and positive ions (c), the error bars correspond to statistical standard deviations. Pixel radial positions were adjusted to transform the ellipse fitted around each component into a circle with a radius equal to the ellipse semimajor axis. The blue curves are fitted Gaussian-power curves (equation 2.17).

is apparent semiminor axis.

The positions of the image pixels were transformed such that an ellipse fitted to the positive ions became a circle of radius equal to the semimajor axis. The average pixel intensities with respect to the scaled radial distance from the center of each identified component are shown in (b), positrons, and (c), positive ions. The distances of the MCP image were scaled from units of pixels to length inside of the Catching Trap. A Gaussian-power curve was fitted to both scaled radial distributions. The fitted radius of the positive ions is interpreted as a reasonable approximation of its radius prior to ejection from the trap.

The daily performance of positron catching was primarily assessed using Faraday cup measurements, as shown in Figure 4.10. Consequently, there is limited data regarding the spatial reproducibility across different days. However, on a single

Repeat #	positrons				ions			
	Peak Intensity	Plasma Radius, mm	Gaussian-Power	NNI	Peak Intensity	Plasma Radius, mm	Gaussian-Power	NNI
1	458	0.624	3.01	4.33E+6	123	0.643	2.66	1.27E+6
2	487	0.595	2.81	4.23E+6	130	0.620	2.58	1.25E+6
3	483	0.601	3.05	4.24E+6	127	0.578	2.48	1.07E+6
4	480	0.613	3.06	4.38E+6	127	0.617	2.60	1.20E+6

Table 4.1: Radial fit parameters of repeated measurements of positron capture with 2.4 million nested ions. The first row corresponds to the MCP image shown in Figure 4.9.

day, four repeated MCP image measurements of the positron catching sequence were performed, the analysis results shown in Table 4.1. The positrons radius and positive ions radius within the Catching Trap are approximately 0.61 mm and 0.62 mm, respectively, with variations on the scale of 0.03 mm and 0.06 mm, respectively. Both radii are in agreement, but this relies upon the previous assumption.

The magnitude of the MCP signal associated with each identified component is quantified by the normalised net intensity (NNI), this is the total integral of the fitted radial profile curve. The NNI of the positrons peak and positive ions peak varied on the scale of 2% and 8%, respectively.
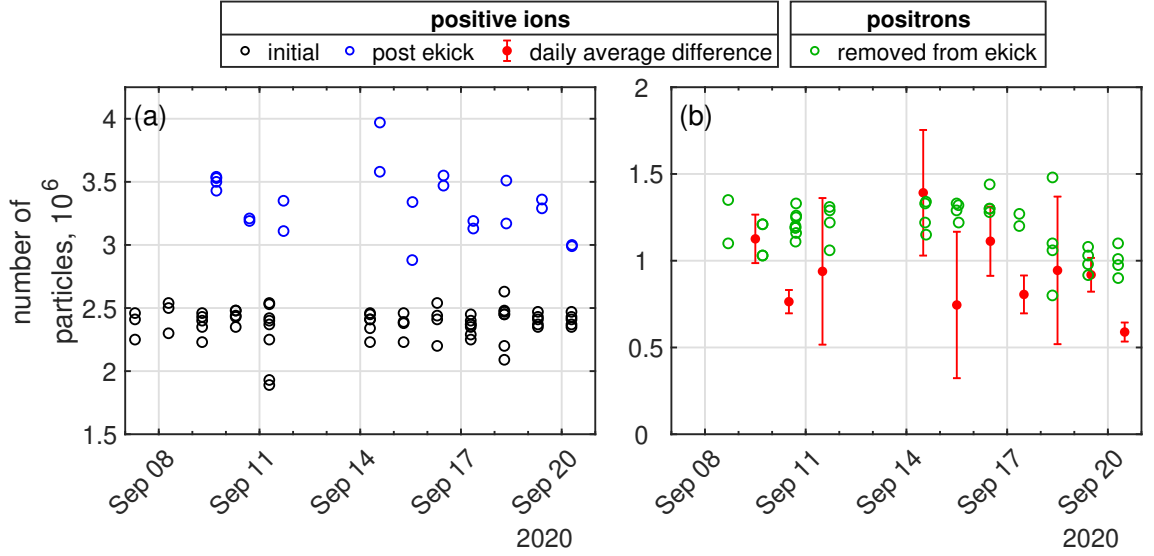
Figure 4.10: Daily baseline Faraday cup measurements from the second positive ion study. (a) The number of initially generated positive ions (black circles) and the number of positive ions after the positron catch, tailoring and ejection of positrons (blue circles). (b) The number of positrons ejected using the electron kicking method (green circles). The difference between the daily average number of positive ions after removing the positrons and the initially generated ions (red dots), the red bars are the statistical errors.

Ideally, the number of positrons mixed with the positive ions would be consistent. This could have been possible using the strong drive regime evaporative cooling technique (SDREVC) [37], but it was not feasible within the scope of this time limited study. As a result, a fixed positron accumulation time of 70 s was used within the positron accumulator, which is primary source of inconsistent catching efficiencies. The Na-22 positron source's sublimated neon moderation efficiency changes on a time scale of days, requiring a new neon moderator to be regrown every one to two weeks. More details on this can be found in Sections 2.1.3 and 2.3.2.

In ALPHA, a known phenomenon is that ions can be generated when charged particles are transferred between Penning traps. These ions are thought to be primarily produced within the targeted Penning trap during the catching phase of the transfer. Charged particles are caught with excess kinetic energy, and the time scales for cooling mechanisms within the trap are much longer than the time of flight between Penning traps. In this study, it was observed that the positive ion population increases when catching positrons. This was confirmed by using methods

later described in Section 4.6.

Daily Faraday cup measurements are shown in Figure 4.10 (a). These measurements include the number of initially generated positive ions, which targeted 2.4×10^6 ions, and the total number of positive ions after catching positrons. Daily measurements of the number of positrons caught are shown in (b). The values vary within a range of $(1.0 - 1.3) \times 10^6$ positrons. However, the variation between each catch on a given day was at most 10%. The number of positrons were measured by electron kicking (ekick) the mixture, see Section 2.2.2, and directing the ejected positrons onto a Faraday cup. The remaining positive ions were measured by a Faraday cup or other diagnostic instruments. No correlation was observed between the number of positrons and positive ions extracted from the same mixture.

The presence of positive ions at high radii cannot be dismissed, but one observation can be made. The maximum radii at which positrons can be detected using the MCP image diagnostic with respect to the Penning trap axisymmetric axis is within $1.3 - 1.6$ mm. This limitation is seen in Figure 4.11, as there is an apparent aperture unique to each species, which is discussed further in Section 4.4. When performing rotating wall compression on the positron and positive ion mixture, discussed later in Section 4.5, no sparse cloud of particles was observed surrounding the compressed mixture. This increases confidence in the effectiveness of the sympathetic diocotron damping during positron catching. However, this relies on there being no significant difference between the positron density during initial moments of the positron catch and during this rotating wall compression, as this could affect coupling between species.

The positive ion temperature after ejecting the caught positrons is $(4.4 \pm 0.8) \times 10^4$ K As a reminder, the initial positive ion temperature is roughly $(3.2 \pm 0.4) \times 10^5$ K. All temperature measurements attempted with the entire mixture were below 10^3 K, which is most likely the positron temperature as discussed previously in Section 4.2.

4.4   MCP diagnostic issue

Previous studies of antiproton and electron mixtures within the Catching Trap by other ALPHA Collaborators have shown an oddity with regards to measurements on the MCP diagnostic. When two negatively charged species are imaged simultaneously they will be displaced from one another, see Figure B.1. Similarly the individual positive ion species and positrons will be displaced from one another, but additionally the radial profile will be misshapen and apertured, see Figure 4.11. Two MCP signals are shown, the left (a) is a radially compressed mixture of positive ions and positrons, with displaced centers. The MCP phosphor screen is outlined by a yellow circle. The right (b) is a radially large distribution of positive ions. Multiple

MCP measurements were taken with increased number of positive ions and waiting minutes for the positive ions to radially drift, however, no positive ions are measured outside of the region outlined by a white curve. Similarly, the is a MCP region that positrons are not detected outside of, this is outlined by a red curve in (a) and (b). The MCP instrument can be moved along an axis perpendicular to the direction
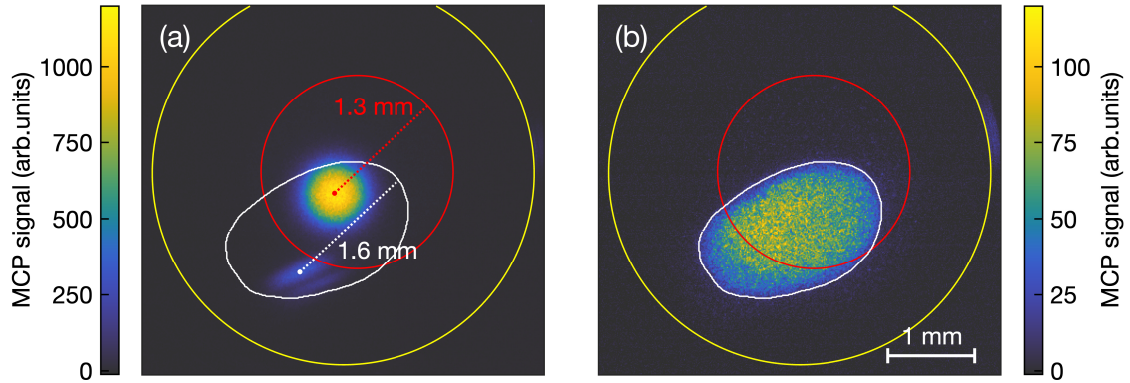
Figure 4.11: Background subtracted MCP images of a compressed positron and positive ion mixture in (a) and a radially large positive ion mixture in (b). The yellow curve outlines the MCP phosphor screen, the red curve outlines the apparent positron aperture and the white curve outlines the apparent positive-ion aperture. The red dot and white dot in (a) indicate the profile centers of the positrons and positive ions. The length scale in (b) indicates corresponding distances within the Catching Trap, as discussed in Section 2.5.2. The dashed lines and values indicate the largest measurable radius of each species' from their central point and their aperture outline. (a) and (b) do not share a common colour scale, this is to improve the colour contrast between the positive ions and background level.

of the Penning trap's axis, this allowed for the positive ion mixture to be imaged at various MCP instrument positions along its movable axis. The MCP instrument was moved between -15 mm and +2 mm from its normal operational position with -100 V, +750 V and +4700 V on the MCP front surface, MCP back surface and Phosphor component respectively. The positive ion mixture consistently impacted a specific region of the front surface, although the -100 V on the front surface is intended to produce a guiding electric field to the surface and the ideal guiding electric field would be homogeneous. Another ALPHA Ph.D. student, Jack Jones investigated the electrostatic potential map of an MCP instrument's geometry [36] within the COMSOL Multiphysics ® software [91]. It was found that the MCP instrument voltage tabs, which protrude radially away from the MCP body, are the most probable source of non-homogeneous electric potentials extending centimetres from the front surface. Such electric potentials were calculated to be comparable to the ejection energies used when extracting charged particles onto the MCP instrument. Introducing a shield onto the Catching Trap MCP is a difficult decision as

it halts experimental measurements and requires the entire stick instrument to be removed and modified in an external lab. Instead a temporary solution was used, which is increasing the particle ejection energies, though this is presently limited by electrode power supplies. This reduces the displacement between the mixed plasma components, and the shape of the positive ion appeared to be less distorted as it became more oval. The MCP image diagnostics of the positive-ions allowed for confirmation of expected qualitative effects, such as sympathetic compression with positrons. However efforts to obtain quantitative information from MCP images were abandoned due to the ever present aperture, which would require greater effort in understanding.

4.5   Sympathetic Radial Compression of Ions

The positron-ion mixture was then transported upstream by sequentially adjusting the applied voltages on the electrodes, also referred to as shuffling. It was moved towards the segmented electrode C06 to perform further radial compression using the rotating wall method, as described in Section 2.2.1. This method was ineffective when applied to the initially hot positive hydrogen ions (without positrons), which could be due it being without a cooling mechanism and its hotter initial temperature causing poor coupling to the rotating dipole electric field. However, it is more appropriate to apply this method to the cooled positive-ion mixture. ALPHA has previously demonstrated the sympathetic compression of antiprotons by using the rotating wall method to compress an electron component of an antiproton-electron mixture [92]. Our situation is nearly the matter-antimatter counterpart, as it is a mixture of positrons and positive hydrogen ions, that includes the proton. The positron-ion mixture was observed to radially expand when held in the trap, which can be halted with this radial compression method. The rotating wall compression is performed within a well formed by electrodes C04, C05 and C06 all biased to -80 V. This well shape was obtained from previously optimised ALPHA experiments that compress electron-antiproton mixtures. The mixture was heated by large rotating wall amplitudes, as the drive amplitude of 5 V_{pp} has a linear response of roughly 1,000 K per 100 kHz, shown in Figure 4.12 (a). The frequency-temperature response was not observed at lower rotating wall amplitudes, as shown by the data at 1 V_{pp} drive amplitude. Although a reduced rotating wall amplitude was less effective in compressing the mixture, it was not studied in detail due to the distortion of the MCP images of the ion mixture's radial profiles.

As a side note, the most compressed mixture observed during this study was achieved using a 1 MHz and 5 V_{pp} drive for 30 s, which resulted in the positron component shrinking by 40% to an estimated radial size of 0.36 mm.

A decision was made to use a 900 kHz at 0.5 V_{pp} rotating wall, as its reduced am-
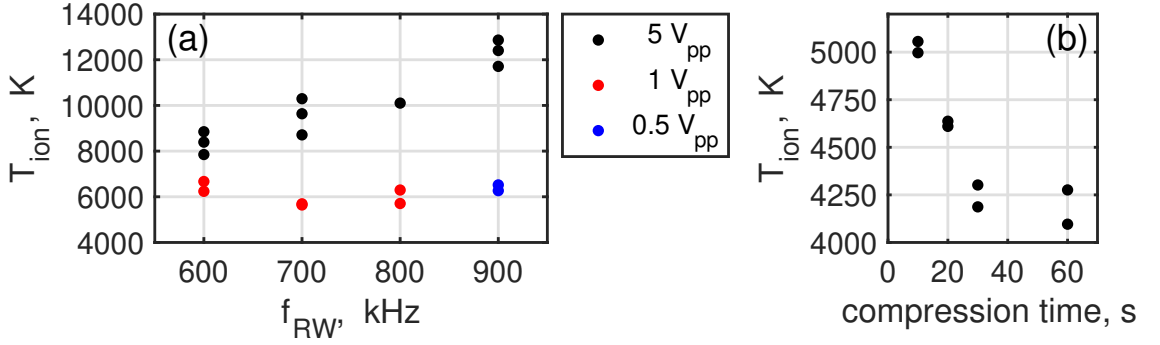
Figure 4.12: The final positive ion temperature after applying a rotating wall compression on a positron-ion mixture. (a) The rotating dipole field amplitude and frequency ω_{RW} is specified by the dot colour and x-axis respectively. (b) various hold times during a 900 kHz 0.5 V_{pp} rotating wall compression.

plitude minimised heating and provided sufficient compression for imaging the entire mixture on an MCP. The ion temperature was found to plateau during the rotating wall compression using the 900 kHz at 0.5 V_{pp} configuration, as shown in Figure 4.12 (b). It is important to notice that the ion temperature prior to the rotating wall was $(4.4 \pm 0.8) \times 10^4$ K, so the absolute cooling rate decreases significantly 30 s into the compression. This might be due to the heating induced by the rotating wall being in near equilibrium with the cooling power of the positrons. Consequently, it was decided to use this rotating wall drive for 10 s for the remainder of this study, resulting in a positive ion temperature of $(4.7 \pm 0.2) \times 10^3$ K. Figure 4.13 (b) and (c) show the radial compression before and after using a 900 kHz, 0.5 V_{pp} drive for 10 s, respectively. Colder temperatures were observed when the mixture was
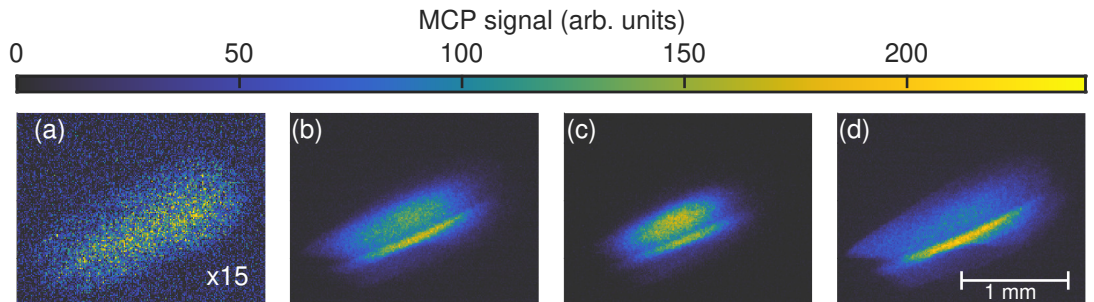
Figure 4.13: Chronologically ordered images of positive ions throughout the sequence leading up until autoresonance, (b), (c) and (d) are after removing positrons from the mixture. The same MCP signal color scale, defined above the images, is used across the four images, but the MCP signals in (a) have been increased by a factor of 15. The length scale in (d) is the same across all four images, this indicates corresponding distances within the Catching Trap, as discussed in Section 2.5.2. (a) Initial 2.4×10^6 positive ions generated. (b) After positron catch. (c) After applying a 900 kHz 0.5 V_{pp} rotating wall for 10 s. (d) After holding mixture for 10 s in electrode C4 biased to -140 V.

axially compressed into an axially short and deep potential well on C04 biased to -140 V. This was intended to allow for further positron cyclotron cooling. Axially

longer wells were tested, though the cooling rate was slower and a similar amount of radial expansion was observed for the same hold times. By holding within the single electrode C04 for 10 s the positive ion temperature was further reduced to $(1.5 \pm 0.1) \times 10^3$ K.

Positrons were removed from the mixture, as the presence of positrons with the positive ions was found to cause the later described purification method to be ineffective. Positron removal was performed using the electron kick technique, by applying a 62 ns pulse at 110 V to pull down a barrier potential. The effectiveness of this step was validated by using caesium iodide scintillation detectors, which are sensitive to the gamma ray products of positron annihilation. Both the potential well shape and the amplitude of the kick voltage was varied until no visual signature of positrons were seen on MCP images and no positrons annihilation signal was observed from a caesium iodide scintillation detector placed outside the same vacuum cross that the MCP instrument is positioned within. The noise level on the detector corresponded to about 4×10^3 positrons. Depending upon how the kick is performed it can introduce heat, which would undermine the ion temperature measurements. So the kick voltage was scanned until the ion temperature was unaffected. The character-

Measured values		Calculated values		
T(K)	1500 ± 100	$n_0(\text{cm}^{-3})$	average $(1.1 - 1.3) \times 10^8$	peak $(1.6 - 1.8) \times 10^8$
N	$(3.0 - 3.8) \times 10^6$	$\lambda_D(\text{mm})$	average 0.23 - 0.26	minimum 0.19 - 0.22
r(mm)	1.6	L(mm)	2.9 - 3.3 *	3.4 - 3.8 **

Table 4.2: Total plasma temperature T, number of particles N, and plasma radius r. Particle densities n_0 calculated from a closed form cylindrical Poisson solver, using the left hand side measured values as input parameters. *calculated using $\exp(-1)$ of peak density. **calculated using 10% of peak density.

istics of the prepared positive hydrogen ions up to this state in the experiment is shown on the left hand side of Table 4.2. The particle densities of the ion-mixture were calculated using a closed form cylindrical Poisson solver. This solver requires an initial guess of the ion mixture's radial distribution but the ion's radial profile was distortion on the MCP. Instead I resorted to using the positron radial profile. Positron radial profiles were extracted from MCP images of the positron-ion mixture, and in theory since the temperature of the mixture is relatively hot then both the positron radial profile and the ion radial profile should be identical. A closed form Poisson solver can be found in [47] and the numerical implementation that reduces the calculation complexity by using the system's cylindrical symmetry can be found in [93]. The calculated Debye length λ_D is much smaller than the plasma length L indicating that this ion mixture is in the plasma regime.

4.6 Identification of Ions

Validating the identity of the ions is essential for any future studies involving these particles. Charge-to-mass spectrometry measurements have previously been conducted within ALPHA [94, 95], using either an autoresonance method or a time-of-flight method. Obtaining absolute charge-to-mass values from autoresonance requires modelling the system, which is a separate study. Therefore, I chose to perform time-of-flight measurements.

A positron-ion mixture was prepared as described up to Section 4.5 and extracted from the Catching Trap towards the downstream Atom Trap MCP instrument. The MCP instrument was operated as a Faraday cup by measuring high-frequency components of the phosphor screen voltage using a high-pass-filter in parallel. The measured Faraday cup signal is convoluted with the MCP gain, this was not calibrated to obtain absolute number of charge information, rather its use it intended to obtain relative species information. Comparing the signals obtained with and without positrons confirmed the earliest peak as being from positrons. A Faraday cup measurement of the positron-ion mixture is shown in Figure 4.14(a). The signal exhibits an exponential decay over time scales that are longer than the particles' arrival times and eventually shows an undershoot. The undershoot occurs because the particle signal is measured via a high-pass filter. No attempt has been made to suitably suppress these features, as my goal is only to estimate the mass-to-charge ratios. If we consider the signal as being dominated by its capacitive behaviour then
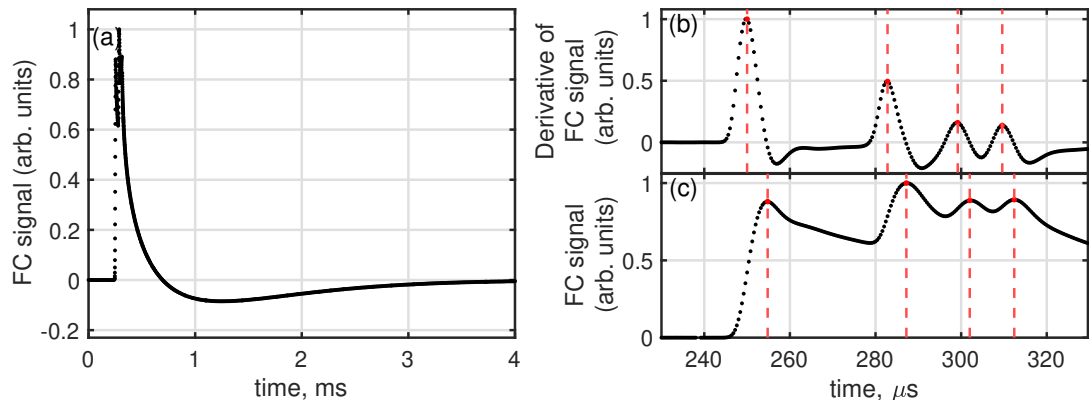
Figure 4.14: A Faraday cup (FC) measurement of a positron-ion mixture ejected from the Catching Trap onto the atom trap downstream MCP. (a) is the measured time series. (b) is the time derivative of the time series. (c) is (a) zoomed in to the region of interest. (b) and (c) have dashed red lines to indicate each peak maxima.

the peak particle-current density will occur at the peak maxima in the time derivative of the signal, this is shown in Figure 4.14(b). The times of the peak maxima in both the signal and the time derivative of the signal are shown as dashed red lines in Figure 4.14(b,c), and whose values are given in Table 4.3. Using the peak times, mass ratios of the ion species can be estimated. A simple ballistic time-of-flight

Species	Peak time, μs	
Label	*time derivative*	*raw*
positron	250.0	254.8
Ion 1	282.8	287.2
Ion 2	299.2	302.0
Ion 3	309.6	312.4

Table 4.3: The times of the four peak maxima shown in Figure 4.14(b,c). The times are in units of μs and the labels are in order of appearance.

model is used, assuming that the entire population is released simultaneously at an unknown time, τ, travels the same path distance, l_path, and acquires the same ejection energy, U. The ith species' time of flight, t_i, can be written as:

$$t_i = \frac{l_\text{path}}{\sqrt{2U}}\sqrt{\frac{M_i}{q_i}} + \tau, \tag{4.6}$$

where M_i and q_i denote the ith species' mass and electric charge, respectively. Let the subscript e represent the properties associated with positrons. Absolute mass-to-charge ratio values can be obtained by considering the time delay between the peak detection time of each ion species and positrons. The ion mass-to-charge ratio can be estimated as:

$$\frac{M_i}{q_i} = \left(\frac{\sqrt{2U}}{l_\text{path}}(t_i - t_e) + \sqrt{\frac{M_e}{q_e}}\right)^2. \tag{4.7}$$

The path distance was measured using CAD models of the apparatus, and the uncertainty in the length was estimated from the Catching Trap electrode-only electric potentials. By considering the potential manipulation during the dump and an electrostatic map of the trap, both the particle ejection positions and ejection electric potential energies were calculated. This calculation provided estimates for both the uppermost and lowermost values of the ejection energy (108.2 eV - 123.5 eV) and the path distance (5.080 m - 5.091 m). The resulting bounds on the absolute

Species	Mass-to-charge ratio *(Method)*	
label	*time derivative*	*raw*
Ion 1	0.90 - 1.03	0.88 - 1.01
Ion 2	2.00 - 2.29	1.84 - 2.11
Ion 3	2.92 - 3.34	2.73 - 3.13

Table 4.4: Estimates for the bounds of absolute mass-to-charge ratio of each ion peak in units of proton mass per unit elementary electric charge.

mass-to-charge ratios can be found in Table 4.4, with units in proton mass per unit elementary electric charge. Assuming all these ions have a unit charge, these bounds suggest that the first and third ions are positive hydrogen ions (H^+ and H_3^+), while

the second ion could be either H_2^+ or He^{2+}. Helium boil-off from cryogenic volumes potentially contaminate the trap's UHV volume. However, following Occam's razor principle, the second ion is more likely the positive hydrogen ion H_2^+, and will labelled as such in subsequent discussions.

The results of the previous calculations using both the raw signal and the time derivative are too similar to distinguish which one is more appropriate to use. To address this, an alternative analysis has been conducted that is independent of ejection energy and path distance, and only considers the peak times shown in Table 4.3.

The time delay between any two peak times is independent of the release time τ. and depends linearly on the path distance. Therefore, the ratio of any of these time delays is independent of the path distance. Using Eq. 4.6, the ratios of delays between observed peaks can be expressed as:

$$\frac{(t_i - t_j)}{(t_m - t_n)} = \frac{(\sqrt{M_i/q_i} - \sqrt{M_j/q_j})}{(\sqrt{M_m/q_m} - \sqrt{M_n/q_n})}, \tag{4.8}$$

where i, j, m and n are subscripts corresponding to any of the observed peak times provided in Table 4.3. Equation 4.8 relates the species mass-to-charge ratios to the observed time delays between peaks. By hypothesising the species corresponding to each peak, the right-hand side of Equation 4.8 can be calculated for various combination of indices (time delays). This approach allows the testing of any proposed set of species and determines if either the peaks extracted from the raw signal and the time derivative signal correspond to a specific hypothesis. The measurement signal consists of charge accumulation accompanied by a capacitive decay. If the capacitive effect is negligible, then the peak positions in the raw signal should be accurate. However, if the capacitive effect cannot be neglected, then the time derivative signal should be a good approximation to the true actual incoming particle signal.

The list of potential candidates is limited to ions with ionisation energies within the trap's energy scale (less than 100 eV), which means highly charged ions can be disregarded. Additionally, by considering the mass-to-charge ratio values provided in Table 4.3, the candidate list can be further refined. The list of candidates, ordered by increasing mass-to-charge ratios, includes $\{H^+, He^{2+}, H_2^+, H_3^+, He^+\}$, with corresponding values $\{1, 1.99, 2, 3, 3.98\}$ proton mass units per elementary electric charge. If He^{2+} is hypothesised to exist, then He^+ should also be considered since it has a lower ionisation energy threshold. As a result,the potential species' identities are limited to the following three hypotheses, listed in the order they appearance in the signal:

First hypothesis : $\{H^+, H_2^+, H_3^+\}$

Second hypothesis : $\{H^+, H_2^+ \text{ or } He^{2+}, He^+\}$

Third hypothesis : $\{H^+, H_3^+, He^+\}$

It should be noted that, regardless of the chosen hypothesis, the first peak is known to be positrons. Let $Y_{i,j,m,n}^{\textbf{exp.}}$ and $Y_{i,j,m,n}^{\textbf{theory}}$ denote the left hand side and right hand side of Equation 4.8 respectively, such that

$$Y_{i,j,m,n}^{\textbf{exp.}} := \frac{(t_i - t_j)}{(t_m - t_n)} \tag{4.9}$$

$$Y_{i,j,m,n}^{\textbf{theory}} := \frac{(\sqrt{M_i/q_i} - \sqrt{M_j/q_j})}{(\sqrt{M_m/q_m} - \sqrt{M_n/q_n})}. \tag{4.10}$$

Here $Y_{i,j,m,n}^{\textbf{exp.}}$ is calculated using Table 4.3 and $Y_{i,j,m,n}^{\textbf{theory}}$ is calculated using the physical characteristics of the hypothesised set of species. There are 256 unique combinations of i, j, m and n to compare measurements to a hypothesis. Note that both $Y_{i,j,m,n}^{\textbf{exp.}}$ and $Y_{i,j,m,n}^{\textbf{theory}}$ are antisymmetric with respect to i and j and similarly with respect to m and n. Thus, $Y_{i,j,m,n} = -Y_{j,i,m,n}$ and $Y_{i,j,m,n} = -Y_{i,j,n,m}$. With these antisymmetries, the information contained in the total number (256) of combinations of i, j, m and n can be reduced to a set of 30 unique combinations, shown in Figure 4.15, which correspond to two sets of 15 combinations that are reciprocals of one another. A
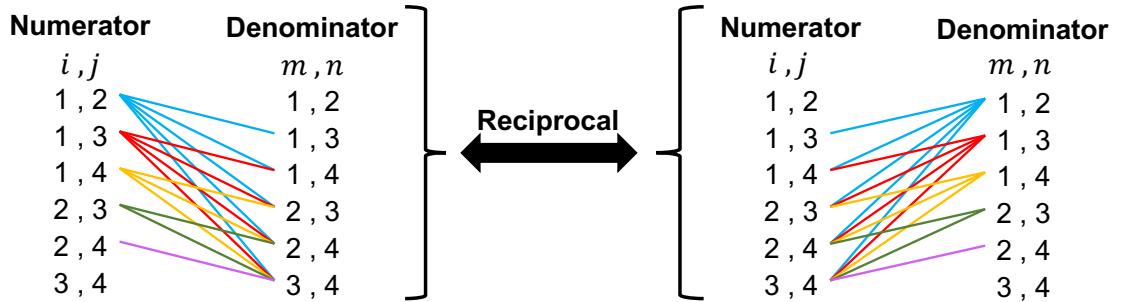
Figure 4.15: The combinations of i, j, m and n that correspond to unique values of $Y_{i,j,m,n}^{\textbf{exp.}}$ and $Y_{i,j,m,n}^{\textbf{theory}}$, excluding values equal to unity, zero and infinity. In the left hand side each set of coloured lines corresponds to a specific i and j combination, and similarly, on the right hand side for m and n combinations.

quantitative measure to compare the set of calculated values of $Y_{i,j,m,n}^{\textbf{exp.}}$ and $Y_{i,j,m,n}^{\textbf{theory}}$ is not provided due to the author's limited knowledge in the subject. Instead, a quantitative data visualization approach was employed. The raw signal peak times from Table 4.3 were used to calculate the values of $Y_{i,j,m,n}^{\textbf{exp.}}$ for the set of indices shown in Figure 4.15 and are displayed as black squares in Figure 4.16 (a). Within the same plot, the theoretical values $Y_{i,j,m,n}^{\textbf{theory}}$ are represented as green, blue and red solid dots corresponding to the first, second and third hypotheses, respectively. The x-axis of Figure 4.16 (a) is a categorical axis, with each unique combination of i, j, m and n uniformly spaced. The first hypothesis has the strongest agreement with the measured peak times, as seen by the green dots overlapping more of the black

squares. The absolute relative difference, denoted as $|\Delta_{i,j,m,n}|$, was calculated to compare the accuracy of each hypothesis with the measurements:

$$|\Delta_{i,j,m,n}| = \left| \frac{Y_{i,j,m,n}^{\textbf{exp.}} - Y_{i,j,m,n}^{\textbf{theory}}}{Y_{i,j,m,n}^{\textbf{theory}}} \right| . \tag{4.11}$$

$|\Delta_{i,j,m,n}|$ was calculated using both the raw signal peak times (S) and time derivative peak times (dS). These values were binned and depicted as histograms in Figure 4.16 (b) and (c), respectively.
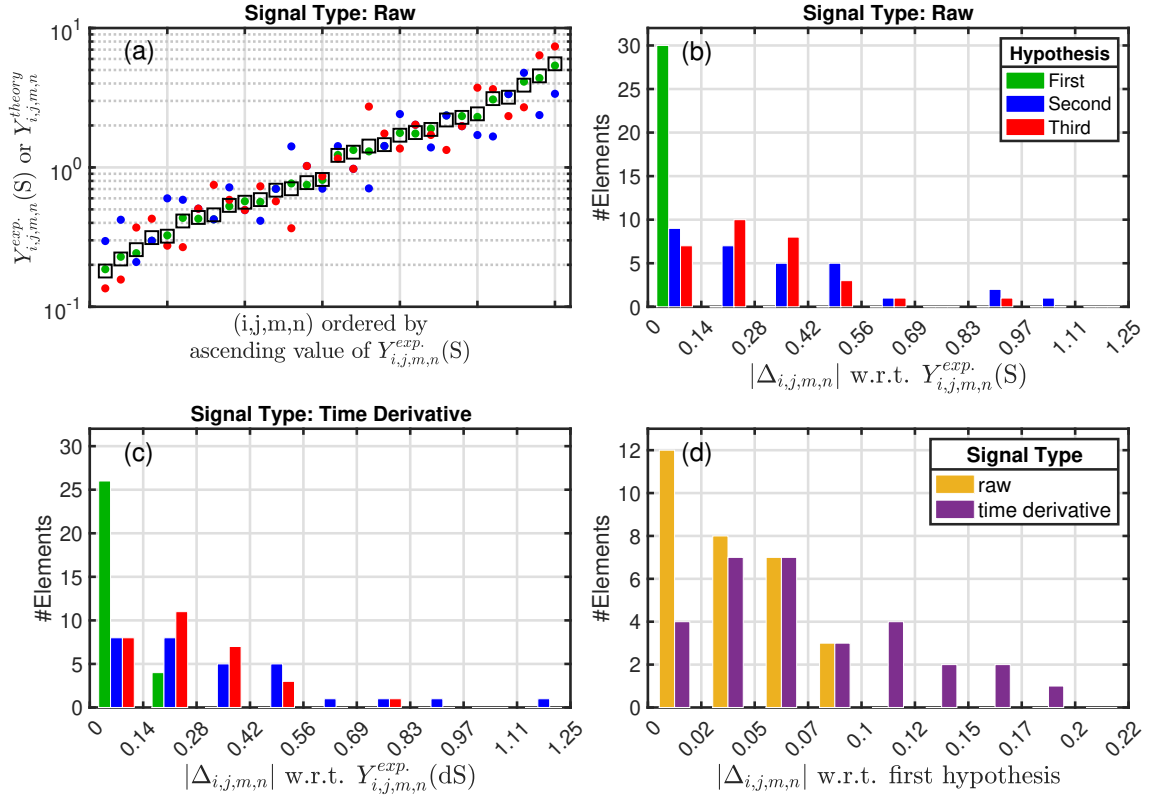
Figure 4.16: In these plots, the green , blue and red data points correspond to the first, second and third hypotheses, respectively. (a) The experimental values $Y_{i,j,m,n}^{\textbf{exp.}}$(S) (raw) and theoretical values $Y_{i,j,m,n}^{\textbf{theory}}$ for each hypothesis are represented by black hollow squares and coloured dots, respectively. The y-axis scale is logarithmic, and the x-axis is non-numeric. Each uniformly spaced position on the x-axis corresponds to specific indices (i, j, m, n), arranged in ascending order based on the values of $Y_{i,j,m,n}^{\textbf{exp.}}$(S). (b) and (c) display histograms of the absolute relative errors $|\Delta_{i,j,m,n}|$, calculated using $Y_{i,j,m,n}^{\textbf{exp.}}$(S) and $Y_{i,j,m,n}^{\textbf{exp.}}$(dS) respectively. (d) A comparison of the first hypothesis data from both (b) and (c) as yellow and purple bars, respectively. However, these bars are binned across a narrower range of values.

In both plots (b) and (c), the first hypothesis (green) demonstrates the highest agreement among all three hypotheses. Conversely, the second (blue) and third (red) hypotheses have a greater number of elements of larger absolute relative errors. Though both show qualitatively similar distributions of values. It seems more appropriate to reframe the current question from "which hypothesis best aligns with

the measurements?" to the alternative question "which set of peak times, presented in Table 4.3, is closest to the predictions of the first hypothesis?".

Figure 4.16 (d) displays the binned relative errors for both $Y_{i,j,m,n}^{\textbf{exp.}}(\text{S})$ and $Y_{i,j,m,n}^{\textbf{exp.}}(\text{dS})$ with respect to the first hypothesis, represented as yellow and purple, respectively. The $Y_{i,j,m,n}^{\textbf{exp.}}(\text{S})$ (yellow) values are frequently smaller, indicating that the first hypothesis agrees more with them. The summed relative error $|\Delta_{i,j,m,n}|$ of $Y_{i,j,m,n}^{\textbf{exp.}}(\text{S})$ is four times smaller than $Y_{i,j,m,n}^{\textbf{exp.}}(\text{dS})$. This may suggest that the peak times observed in the raw signal are closer to the 'real' time of flight signal.

From both of these analyses, it can be stated with reasonable confidence that the ion particles observed in the time of flight measurements are the first hypothesised particles $\{\text{H}^+, \text{H}_2^+, \text{H}_3^+\}$, and importantly for this work, this is considered evidence for the presence of protons within the produced ion mixture.

4.7   Conclusion

The vacuum quality of the Catching Trap is maintained at 10^{-13} mbar by a combination of ion pumps and cryopumping, a necessity for the storage of antiprotons. Under such stringent vacuum conditions, the production of positive hydrogen ions is not observed. To overcome this, the vacuum was intentionally degraded by disabling the ion pumps for durations ranging from several hours to multiple days. This action increased the trap vacuum pressure and degraded the cryogenic surfaces, consequently reducing the efficiency of cryopumping even after the ion pumps were reactivated.

As a result of the reduced cryopumping, the Catching Trap began to achieve higher baseline densities of residual gas, allowing the production of 2.4×10^6 positive hydrogen ions via electron impact ionisation within a minute. Positive ions produced in this manner exhibited a temperature of $(3.2 \pm 0.4) \times 10^5$ K and were radially sparse.

To prevent ion impact ionisation of the residual gas, which could alter the relative composition of the mixture, the temperature of the positive hydrogen ions was subsequently reduced. This cooling was achieved through interactions with positrons, which, in a high magnetic field (3 T in the Catching Trap), emit energy as cyclotron radiation. Positrons were transported from the positron accumulator to the Catching Trap, transiting through the ALPHA-2 trap. This marked the first instance of positrons being captured and stored within the Catching Trap. Due to the misalignment between the central axes of the ALPHA-2 Penning trap and the Catching Trap, the positron bunch was injected and captured off-axis, causing the bunch to spiral radially inward towards the central axis of the trap (a phenomenon known as diocotron damping).

The positron loading took place after the generation and trapping of positive hydro-

gen ions in the Catching Trap, causing the diocotron damping to radially compress the positive-ion plasma. Subsequently, the mixed positron and positive-ion plasma was compressed axially, and the trapping electric field was increased. The rotating wall technique was used to further radially compress the mixture.

When the preparation stage was completed, the positrons were extracted from the mixture. The composition of the mixed positive ion plasma was studied through time-of-flight measurements, identifying the components as H^+, H_2^+, and H_3^+.

This preparation sequence allows for the reproducible generation of positive hydrogen ion plasma samples with known temperature, radial size, and total ion numbers. In the collected data, the fractional composition of H^+, H_2^+, and H_3^+ proved reproducible, although this was not quantified. The isolation of protons from this positive hydrogen ion plasma using an autoresonance technique will be discussed in the following chapter.

PROTON PLASMA ISOLATION

This chapter discusses an autoresonance (AR) study of positive ions, which were prepared as described in Chapter 4. The initial Section 5.1 provides a brief introduction to autoresonance, which is essential for understanding the experimental results. Section 5.2 describes the Catching Trap AR potential well and presents calculations estimating the relationship between the axial energy and axial frequency of each positive ion species within this AR potential well.

Section 5.3 outlines the steps involved in the AR experiment sequence and provides additional notes into its development. The isolation process consists of two main stages. First, the axial motion of ions is energised via an autoresonant process, which involves coupling their movement to a sinusoidal electric field with a frequency that gradually changes over time. This frequency variation, called chirp, causes a minor proportion of the coupled ions to be expelled from the trap. Second, following this autoresonant frequency chirp, the depth of the trap's electric well is lessened. This causes the ejection of the remaining coupled ions, completing the isolation process. Section 5.4 presents measurements of particles ejected during both an AR frequency chirp and a reduction of the trap electric well depth, as described in Section 5.3.

Section 5.5 presents time-of-flight measurements of the remaining trapped positive ions. An analysis of these time-of-flight measurements is provided in Section 5.6 to quantify changes in the positive ion composition. Section 5.7 presents MCP images of the remaining positive ions. Measurements of isolated protons are presented in Section 5.8, obtained using the developed method involving autoresonance.

5.1 Theory of autoresonance

The natural frequency of an ideal harmonic oscillator is determined by its inertia and the proportionality of its restoring force. When a force is applied at a frequency close to this natural frequency, the total energy of the oscillator increases, leading

to larger oscillatory movements. However, consider a situation where the oscillator typically only moves across small distances, experiencing harmonic motion. As the amplitude of this motion increases, the oscillator interacts with an anharmonic potential, altering its motional frequency as its energy increases. If the oscillator's motional frequency decreases with larger oscillation amplitudes, the externally applied force, oscillating at its own rate, becomes too rapid to maintain resonance with the oscillator. This discrepancy results in an energy exchange that dampens the oscillator's motion. As a result, the amplitude of the oscillator's motion reduces, causing its frequency to revert towards the original harmonic value. At this point, the external force can once again stimulate the oscillator motion, initiating a repeating cycle of these events.

To maintain near resonance, the external drive frequency can be slowly swept, following the changing oscillator frequency. This process, called autoresonance [96, 97], allows control over the oscillator's energy, provided the potential-well shape causes the oscillator's frequency to decrease monotonically with increasing energy. By sweeping the external drive to lower frequencies and ensuring a slow enough sweep rate, the oscillator's instantaneous frequency can follow the external drive frequency.

Autoresonance has been used to excite the axial energy of trapped charges particles by applying an oscillating voltage, generated by a waveform generator, to one of the electrodes involved in particle trapped. This technique has been used in the Atom Trap to control the mixing energies of antiprotons and positrons for antihydrogen production [98], and to perform mass-spectroscopy of ionised residual gas [94, 99]. However, the later study did not extend its techniques for producing specific or single species plasma, though this work has been inspired by it.

The oscillating electrical signal is called a chirp, as it sweeps through many frequencies. It starts at an initial frequency ω_i and linearly decreases at a sweep rate α, turning off once it reaches the final frequency ω_f. A linearly frequency chirp can be expressed as $\omega(t) = \omega_i - \alpha t$. The chirp peak-to-peak voltage initially increases from zero to its maximum set value, $\bar{\epsilon}$, during the initial oscillation cycles and decreases to zero later during the final oscillation cycles. In this work the peak-to-peak voltage is referred to as the chirp amplitude. Autoresonance occurs when the chirp frequency pass through the oscillator's axial frequency, ω_0, and its amplitude must be larger than a threshold value $\bar{\epsilon}_c$.

A scaling law of $\bar{\epsilon}_c$ can be derived for non-neutral plasma [97], and is proportional to $\alpha^{3/4}$. However a detailed discussion of this scaling law is beyond the scope of this work. If the chirp amplitude is below the threshold $\bar{\epsilon}_c$, the oscillator will not lock onto the chirp signal. The range of chirp amplitudes for transitioning from not driving particles to driving particles is narrow. Autoresonance can occur when the the drive frequency passes through a harmonic of the oscillator frequency, referred

to as subharmonics ω_0/n, where n is an integer [100]. The scaling laws for their corresponding amplitude thresholds become weaker power laws for larger values of n, scaling proportionally to $\alpha^{3/(4n)}$ [100].

5.2 Autoresonance potential well and axial frequency-energy curves

The autoresonance (AR) chirp generation hardware primarily consisted of National Instruments hardware. A PXI-8101 embedded controller was programmed to control a PXI-5421 waveform generator. The AR signal was configured using LabVIEW on a desktop computer, and the PXI controller transferred the waveform file to the waveform generator. The waveform generator was configured to wait for a trigger signal before outputting the loaded waveforms.

The sequencer hardware, as mentioned in Section 2.1.7, served as the trigger source, ensuring the chirp was output at the appropriate time. The experimental sequence was programmed to wait for the AR signal to end before proceeding with the remainder of the sequence. The waveform generator provided an end trigger signal, which simplified the programming of the experiment.

Figure 5.1 shows the potential well used for performing AR, where the trapped ion mixture center is located at electrode C08. The AR trapping potential is set for electrodes C05 through C11 with the following voltages values: [140, 140, 140, -70, 120, 120, 50] Volts. All other electrodes are electrically grounded. The output of
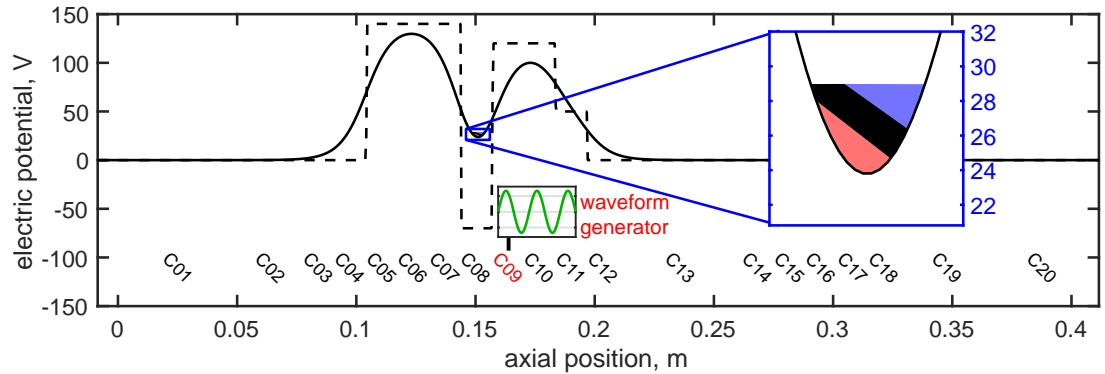
Figure 5.1: The electric potential well for trapping positive ions and performing AR studies, space-charge is neglected. The on-axis electric potential and the applied electric potential are given by the black full line and black dashed line respectively. The black, blue and red band regions indicates the axial extent for trapping the positive ions and the range of energies are approximations informed from temperature diagnostic measurements.

the waveform generator was connected to electrode C09 through a high-pass filter circuit with a cut off frequency of 170 kHz. Then, a DC voltage was then applied

to electrode C09 via a low-pass filter circuit with a cut off frequency of 25 kHz. This configuration allowed electrode C09 to be involved in generating the electric potential trap. This meant that a negative voltage could be applied to C09 for producing large axial electric fields experienced by the ion mixture. During the development of the AR trap potentials, values similar to those shown in Figure 5.1 were used, with a positive voltage applied to C09 that was lower than the voltages on C08 and C10, to create small trap electric fields. However, poor coupling was observed between the ion species and the AR chirp. To enhance coupling, the trap electric fields were increased by applying a negative voltage to C09 while maintaining positive voltages on the neighbouring electrodes.

Moreover, using a low-pass filter allowed the DC voltage to ramp up to a positive value, ejecting particles from the trap. The trap electric potential was axially skewed to direct ejected particles downstream towards the MCP instrument. Operating the MCP instrument in high gain mode enabled small currents of ejected particles to be observed both during and after the AR chirp.

The axial bounce frequency, which refers to the oscillation frequency of trapped charged particles along the trap axial axis, was calculated for both vacuum trapping electric potentials and various electric potentials generated by space charge distributions. The latter were determined using a closed Poisson solver, a numerical implementation was developed during this work, as mentioned earlier in Section 4.5. These calculations and related details are available in Appendix E. Figure 5.2 shows the calculation results, where blue, red and green correspond to protons, H_2^+ and H_3^+, respectively. The three positive ions exhibit unique axial frequency-to-axial energy curves due to their unique charge-to-mass ratio. These curves were calculated for two different radial positions with respect to the trap axis, on the trap axis and at a radius of 1.6 mm from the trap axis. The axial frequencies of the vacuum trapping potential are shown as dashed lines and dotted lines, corresponding to the trap axis and plasma radius from the trap axis (1.6 mm, see Table 4.2 for plasma parameters), respectively. The calculated on-axis, 0 mm, and plasma radius, 1.6 mm, axial frequencies are stated to indicate the range of axial frequencies across most of the positive ion plasma. The thermally averaged axial frequency was calculated for each species. The initial axial frequencies of protons range from 1.723 to 1.744 MHz, and those of H_2^+ range from 1.218 to 1.233 MHz, and those of H_3^+ range from 0.9952 to 1.007 MHz. The broadening of the axial frequency due to the 100 K accuracy of the ion temperature, mentioned in Table 4.2, can be neglected as they are on the order of 10 Hz. When the space charge electric potential is included in the calculations, the shape of the axial frequency-energy curve changes significant, as shown in Figure 5.2. These axial frequency-energy curves are non-monotonic, leading to degenerate axial. At low axial energies, the axial frequency increases monotonically until it reaches some maximum axial frequency, after which the relationship becomes monotonically
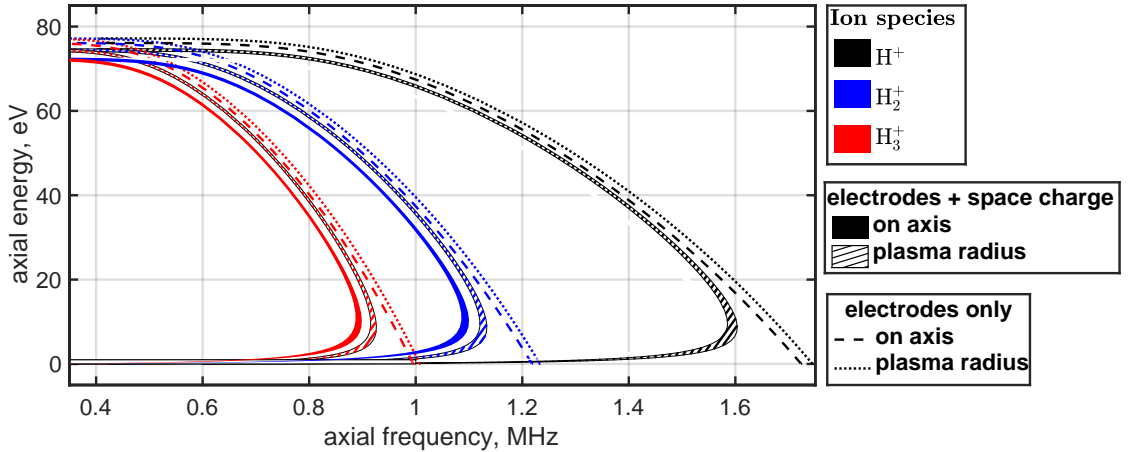
Figure 5.2: Calculated single particle axial frequency to axial energy curves. Calculations related to H^+ is black, H_2^+ is blue and H_3^+ is red. The filled and hatched regions were calculated using both the trapping electrodes' electric potentials and the positive ion space charge. The dashed lines and dotted lines were calculated only using the trapping electrodes' electric potentials.

decreasing. The thermally averaged initial axial frequencies for space charge corrected curves range from 0.3643 to 0.8515 MHz for protons, 0.2575 to 0.6019 MHz for H_2^+, and 0.2104 to 0.4918 MHz for H_3^+. These space charge corrected curves have a much broader range of thermally averaged axial frequencies.

These calculations were performed after the data collection for this thesis was completed. Similar calculations by Siara Fabbri, a colleague, were used during this study to guide the choice of configurations of the AR chirp, although those calculations only considered the trapping electric potentials.

5.3 Autoresonance experiment sequence and development notes

The coupling between trapped particles and the chirp was observed, but the method's effectiveness was evaluated based on the removal of the target species and minimizing the impact on the non-target population. The ejection process is not guaranteed, as an excited target species can decouple from the chirp near escape energies and stochastically eject. Particles driven to high axial energies but not ejected will thermalise with the remaining population, causing heating and radial expansion. Decreasing the final chirp frequency, which corresponds to increasing the final axial energy, did not improve particle ejection.

The estimated average time between collisions within the plasma, based on temperature and density, is 3 ms. Hypothetically, this allows the trapping well to be reshaped, by changing the applied voltages to each electrode, before thermalisation

occurs. By reducing the well depth after the chirp has ended, the axially driven particles can be removed, a process later referred to as a "well depth cut." An appropriate well depth cut value was determined by performing a typical temperature dump from the AR well. Since the temperature dump is a sequence of thousands of known incremental voltages changes to the electrodes, the initial particle ejection signal time can be converted to a well depth. This measured value is considered the minimum well depth at which non-targeted species will remain trapped. The well depth cut value was measured daily and updated in the working sequence due to variations in the space charge of the prepared positive ion plasma. Without considering space charge effects, the AR well's depth is 76.1 V, and a typical well depth cut would reduce this by 52 - 56 V. This procedure is illustrated in Figure 5.3, with
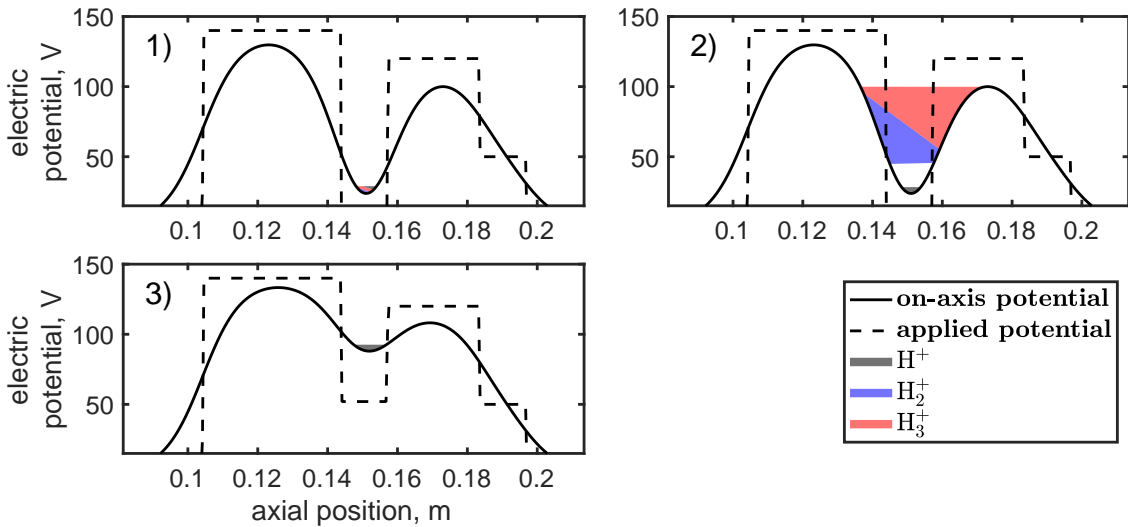
Figure 5.3: The Catching Trap electric potential sequence for autoresonance of the tailored and cooled positive ions discussed in Section 4.5. The coloured patches indicate estimates of the particle energy and axial distributions. (1) Positive ions trapped within a static AR potential well. (2) Apply AR chirp signal, in this example H_2^+ and H_3^+ (the heaviest ions) were targeted, causing ions to be driven to larger axial kinetic energies. (3) Reduce well depth to eject remaining driven ions.

the following sequence steps:

1. Trap the positive ion mixture in the previously defined AR potential well.

2. Apply a preconfigured chirp signal onto electrode C09, and wait until the chirp stops.

3. Reduce the potential well depth to eject the remaining driven particles.

Once the chirp has finished, the targeted species will have axial energies in the tens of electron volts. A fixed 1 ms time delay between the end of the chirp signal and the well depth cut was used throughout this study, as it was shorter than the estimated 3

ms collisional time scale, and the time scale for the stochastic ejection of the positive ions is unclear. The well depth cut ejects the heavier axially excited positive ions. The AR scan measurements were performed in one of two modes. In the first mode, the CT stick at its MCP instrument position, where ejected positive ions are measured using a voltage readout. The same instrument can be used to measure the remaining population's radial profile, temperature or particle count. In the second mode the CT stick is at its pass-through position, so that no ejected particles can be measured. Instead, the remaining population can be transported approximately 5 m to the downstream AT stick MCP instrument within milliseconds, allowing for a measurement of its time-of-flight structure, similar to Section 4.6.

During development, initial testing was conducted with a shallower AR well. Chirp signals were found to be more effective at ejecting particles than in the deeper AR well. The initial axial frequencies of each species appeared to be similar; removing all of the H_3^+ population would remove a significant amount of protons. Attempts to perform AR with a small population of positrons within the positive ion plasma were made, but no response to applied chirps was observed.

Initial AR development was carried out on samples of 1.2×10^7 positive ions, similar to the previously described samples of 3×10^6 positive ions previously in Chapter 4. No distinct subharmonic series were observed in the ejection signal of 1.2×10^7 populations, while the 3×10^6 populations did show subharmonic series, see the previous Section 5.1 for details on subharmonics. The ejection signals from both populations were reproducible.

During the initial development with 1.2×10^7 positive ions, a sequence that successfully purified the plasma into just protons was found. However, days after the initial measurements of the successful sequence repeated measurements became inconsistent and was eventually abandoned. This inconsistency might have been due to the vacuum quality degrading, causing positive ion generation to be more sensitive to residual heating. A possible solution to this heating was to reduce the space charge involved in the study, which could be achieved by reducing the density of the positive ion plasma or the positive ions population. Reducing the density would require redeveloping most of the experimental sequence to trap the plasma across a larger volume. Therefore, the latter option was attempted, reducing the positive ion population to 3×10^6 positive ions, which improved the reproducibility of measurements. During the development of this more consistent reduced population, a method of calibrating the AR well depth cut with a temperature dump was implemented, improving the consistency of AR experiments. Though this development was not implemented to larger positive ion population.

In order to better understand the plasma's response and increase confidence in the resulting isolated protons from this study, the AR chirp parameters were scanned. The chirp final frequency was fixed to 100 kHz, as reducing it yielded

negligible results. The chirp sweep rate was fixed to 200 MHz s^{-1}, chosen because it is close to the hardware limitations for signal generation, and slower sweep rates, such as 75 MHz s^{-1}, performed worse at ejecting particles. This faster sweep rate also minimises the time available for driven particles that were not ejected to thermalise. The following sections involve two parameter scans: the chirp start frequency with a fixed amplitude of 5 V$_{pp}$ and the chirp amplitude with a fixed start frequency of 1.5 MHz. As previously mentioned, two measurement methods were available for obtaining information from the chirped plasma, either on the Catching Trap stick or downstream Atom Trap stick MCP-phosphor instrument. These measurements are presented in separate sub-sections, as the former gives greater details about when the AR phenomena occurs to the bulk of the plasma, while the latter offers information about the resulting effect on individual species within the plasma.

5.4 Particle ejection during frequency chirp and well depth cut

This section presents measurements from both an AR chirp amplitude scan and start frequency scan. Positive ions ejected from the trap during the AR chirp and well depth cut were detected using the Catching Trap stick MCP-phosphor instrument and a SiPM, as described in Section 2.5.3. The positive ion plasma involved in these measurements was prepared using the methods outlined in Chapter 4, and its characteristics can be found in Section 4.5, specifically in Table 4.2. As a reminder, the positive ion plasma contains approximately 3×10^6 positive ions, has a plasma radius of 1.6 mm, and is at a temperature of 1500 ± 100 K. The purpose of these measurements is to demonstrate the AR response of the positive ions and quantify the performance of the AR sequence during each step. However, they were not used to determine optimal AR chirp configurations for isolating protons; that was the focus of the measurements presented in the following Section 5.5.

The SiPM signal was connected to a preamplifier, which was then digitized by a National Instruments PCI-6132 at a sample rate of 2.5 MS/s (million samples per second). This configuration is designed to resolve features with durations shorter than the time-of-flight separation between ejected species. The Catching Trap stick located 1.2 m away from the trap. Neglecting space charge effects, the ejection energy of the AR potential well is 100 eV. The ballistic time-of-flight for a proton is approximately 8.7 μs. The arrival delay time between a proton and H$_2^+$ ion is 3.6 μs, and between a proton and H$_3^+$ ion is 6.3 μs. During the AR chirp, positive ions are ejected from the trap and can be observed with the SiPM. These ejection signals are visible in both the chirp amplitude scan measurements in Figure 5.4 (b) and the chirp start frequency scan measurements in Figure 5.6 (a). Multiple peaks

are observed in the ejection signal, indicating that particles are ejected in bunches with some structure. The time scale of delay between these peaks ranges from tens to hundreds of microseconds. This delay is not considered to be due to species separating during the time of flight, as estimates of separation are on the order of $3.6 - 6.3\,\mu$s. Instead, the peak structure should be considered as a combination of various autoresonances and possibly subharmonics.

The scan of the AR chirp amplitude modifies the peak-to-peak voltage of the chirp while maintaining all other chirp parameters constant: the initial frequency ω_i at 1.5 MHz, the final frequency ω_f at 0.1 MHz, and the chirp rate α at 200 MHz s^{-1}. Figure 5.4 presents the SiPM particle ejection signals recorded during both the AR chirp and the subsequent reduction in the well depth. Figure 5.4 (a) presents the
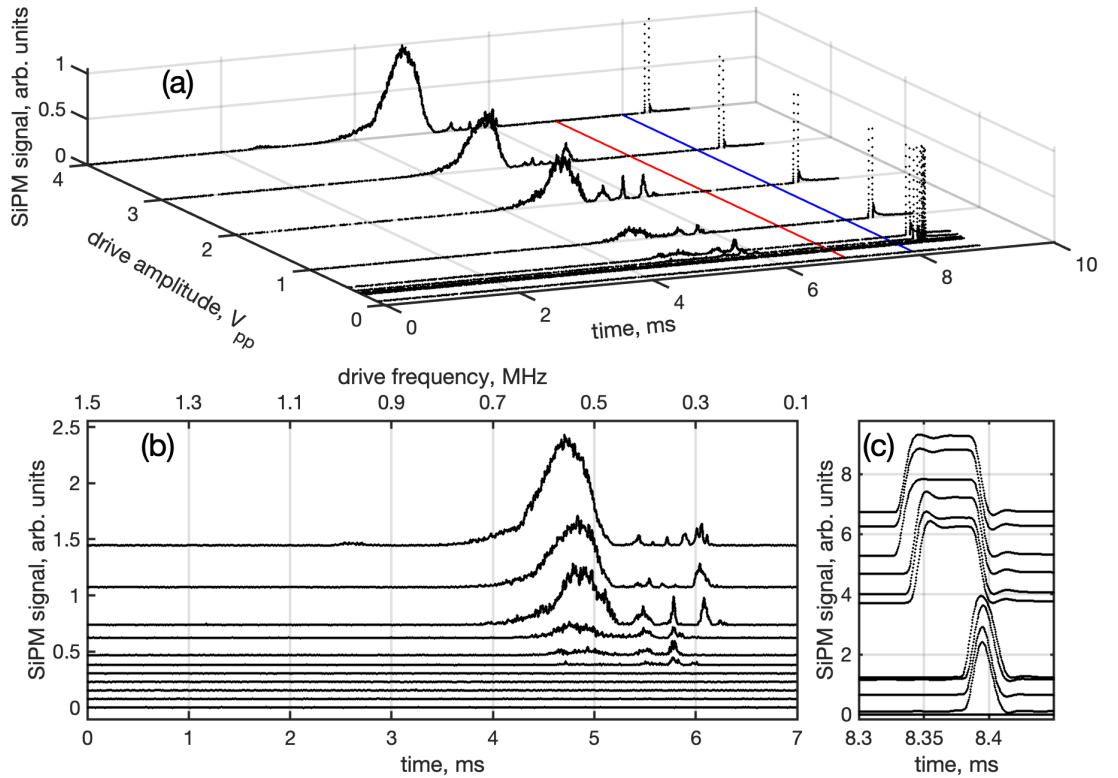
Figure 5.4: Particle ejection signals with varying AR chirp amplitudes, while other AR chirp parameters remain constant. (a) Full particle ejection signal measured from the Catching Trap SiPM. The red line indicates the end of the AR chirp and the blue line indicates the start of the well depth cut. (b) Signal segment during the AR chirp. The top x axis in (b) shows the corresponding frequency of the AR chirp. (c) Signal segment during well depth cut. Fixed chirp parameters: $\omega_i = 1.5$ MHz, $\omega_f = 0.1$ MHz and $\alpha = 200$ MHz s^{-1}. AR chirp amplitudes {0.1, 0.3, 0.31, 0.325, 0.35, 0.4, 0.5, 1, 2, 3, 4} V$_{\mathrm{pp}}$. Within (b) and (c), signals are arranged vertically in ascending order of AR chirp amplitude.

complete SiPM signals of the chirp amplitude scan measurements during both the

AR chirp and the well depth cut. A red line indicates when the chirp signal ends, and a blue line marks when the well depth cut starts. In plots (b) and (c), signals share a common vertical scale and are vertically stacked in order of increasing chirp amplitude. However, the common vertical scale factors in (b) and (c) differ because the signal amplitudes are larger in (c). Initially, measurements of these signals used a lower amplification gain, resulting in a single peak of varying width during the well depth cut with no additional structure. To resolve weak peaks during the AR chirp in (b), the amplifier gain was increased. This higher amplifier gain was applied to all measurements shown in Figure 5.4, causing the well depth cut signal in (c) to saturate in voltage, as observed as plateaus following the peak maximum.

Two distinct thresholds for ejected particles appear during the AR chirp and the well depth cut, as seen in Figure 5.4 (b) and (c). The AR coupling threshold first appears in the well depth cut, limiting the amplitude threshold to between 0.1 and 0.3 Vpp. The particle ejection signal during the AR chirp emerges at 0.4 Vpp, and within this signal, the ejection signal during the well depth cut significantly broadens and its voltage saturates the data acquisition hardware.

The signal strength measured my the SiPM is expected to be directly proportional to the current of ejected particles, so the integral value of the SiPM signal above the background level is proportional to the amount of ejected particles. The integral above the background level was separately calculated for the two periods, during the AR chirp and during the well depth cut. Figure 5.5 (a) and (b) display the integrated signal value, proportional to the number of ejected particles, for the AR chirp (in red) and the well depth cut (in blue).
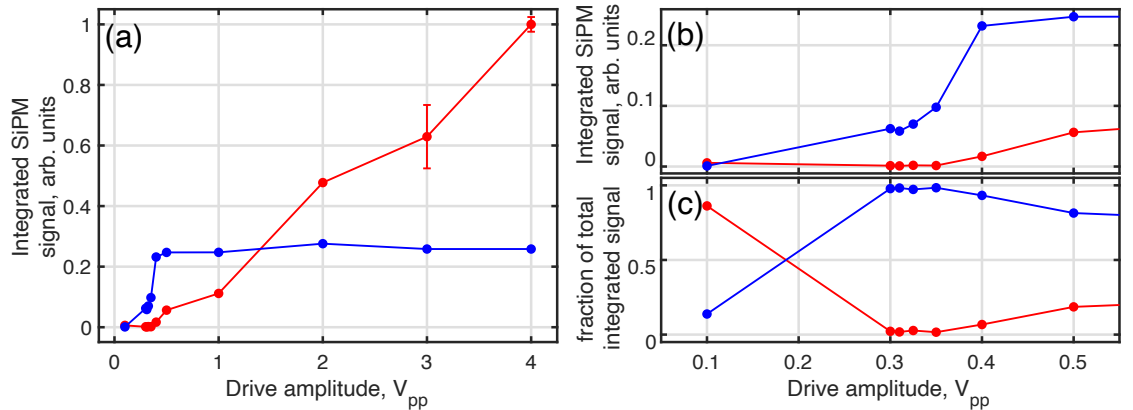
Figure 5.5: (a) The integrated particle ejection signals of various AR chirp amplitudes, with other AR chirp parameters fixed. SiPM signals taken from Figure 5.4. Red dots are during the AR chirp and the blue dots are during the well depth cut. (b) A magnified view of (a) to better see the onset of ejected particles. (c) The fraction of the total integrated signal measured during either of the specified periods of time.

In Figure 5.5 (a), a plateau is observed, indicating saturation of the well depth cut signals. The integrated signal during the AR chirp increases almost linearly up

to 4 V_{pp}. The AR chirp amplitude threshold during both durations is more evident in Figure 5.5 (b).

The fraction of the total integrated ejection signal within each of the two durations of the signal is shown in Figure 5.5 (c), using the same corresponding colours. The fraction of the total integrated ejection signal from a chirp signal with an amplitude of 0.1 V_{pp} is dominated by systematic noise. The integrated ejection signal for chirp amplitudes between 0.3 V_{pp} and 0.35 V_{pp} remained approximately constant, with 2% during the AR chirp and the remaining 98% during the well depth cut. The signal saturates during the well depth cut for chirp amplitudes larger than 0.4 V_{pp}, ending the previous constant fraction behaviour. Consequently, the fraction of the total signal starts to increase during the AR chirp. As the ejected particles are correlated across the two durations, extrapolation of this constant fraction behaviour beyond a chirp amplitude of 0.35 V_{pp} is not possible.
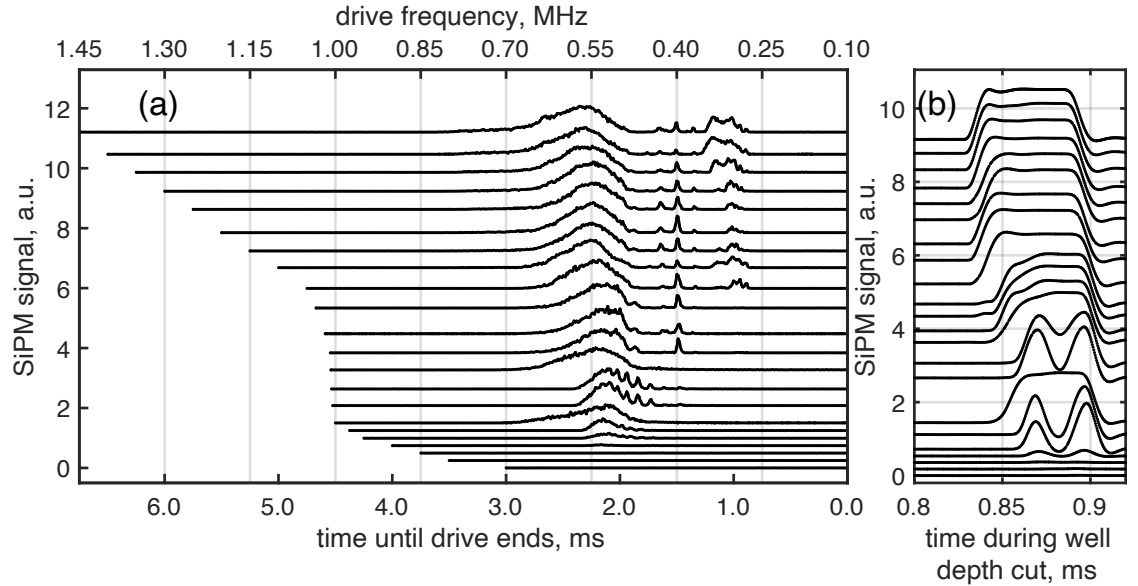
Figure 5.6: Particle ejection signals for various AR chirp start frequencies, with other AR chirp parameters fixed. (a) Signal segment during AR chirp. The top x axis in (a) indicates the corresponding frequency of the AR chirp. (b) Signal segment during well depth cut. Fixed chirp parameters: $\bar{\epsilon} = 5$ V_{pp}, $\omega_f = 0.1$ MHz and $\alpha = 200$ MHz s^{-1}. AR chirp start drive frequencies: {0.7, 0.8, 0.85, 0.9, 0.95, 0.975, 1, 1.005, 1.007, 1.008, 1.009, 1.018, 1.034, 1.05, 1.1, 1.15, 1.2, 1.25,1.3, 1.35, 1.4, 1.45} MHz. In (a) and (b), signals are arranged vertically in ascending order of AR chirp start frequency.

In Figure 5.6, the complete SiPM signals from the chirp start frequency scan measurements during both the AR chirp and the well depth cut are presented. The AR chirp start frequency scan varies the chirp start frequency while keeping the remaining chirp parameters constant, with $\bar{\epsilon} = 5$ V_{pp}, $\omega_f = 0.1$ MHz, and $\alpha = 200$ MHz s^{-1}. In both plots (a) and (b), the signals have a common vertical scale and are arranged vertically in ascending order of chirp start frequency. However,

the common vertical scale factors differ between (a) and (b) due to larger signal amplitudes in (b). Plot (a) displays the signal during the AR chirp, while plot (b) shows the signal during the well depth cut.

For a fixed chirp sweep rate α, adjusting the chirp start frequency ω_i changes the chirp duration. Consequently, the ejection signal's time axis is plotted with respect to the chirp signal's end time. This approach aligns the chirp frequencies across different signals and reveals a clear correlation between the peak structures of various AR chirps. Peaks appear at the same chirp frequency when the start frequency surpasses a threshold frequency.

For start frequencies larger than 0.95 MHz, a broad peak appears for a chirp frequency of 0.55 MHz. Beyond start frequencies of 1.008 MHz, a new series of peaks emerges, most prominently at a chirp frequency of 0.4 MHz. Finally, a third series of peaks appears around chirp frequencies of 0.3 MHz for a start frequency of 1.034 MHz. This structure seems to indicate the onset of each plasma species' coupling to the chirp, though this hypothesis is not confirmed by any prior or subsequent measurements. In Figure 5.6 (b), a two-peak structure during the well depth cut ultimately becomes a single broad saturated peak after a start frequency of 1.008 MHz. An inconsistency occurs at 1 MHz with a single broad saturated peak, possibly due to variations in the prepared positive ion plasma affecting the onset chirp start frequency for different species.

Similar to Figure 5.5, the SiPM signals were background subtracted and then integrated to quantify the relative change in the ejection signal, and the integrated signal was calculated for both the AR chirp duration and well depth cut duration. The integrated ejection signals for the AR chirp and well depth cut are shown in Figure 5.7 (a) as red and blue, respectively. The fraction of the total integrated ejection signal within each signal duration is shown in Figure 5.5 (b), using the same corresponding colours. The emergence of new series of peaks in the ejection signal during the chirp period appears as abrupt increasing steps, roughly observed around the 1 MHz cursor in (a). The amount of ejected particles plateaus after the appearance of the last series of peaks, but after approximately a 200 kHz increase, the signal starts to increase again. The first three data points in (b) are predominantly affected by systematic noise. Once particle ejection occurs, nearly equal amounts of particles are observed during both periods. The fractional amount of ejected particles during the chirp period increases with increasing start frequency, although this is exaggerated by the data acquisition hardware saturating during the well depth cut period.

The chirp amplitude scan reveals a distinct increase in autoresonantly coupled particles during the well depth cut, which is contrary to the appearance of peaks and their increasing amplitudes observed during the AR chirp. The chirp start frequency scan shows discrete appearances of a series of ejection peaks during the chirp period.
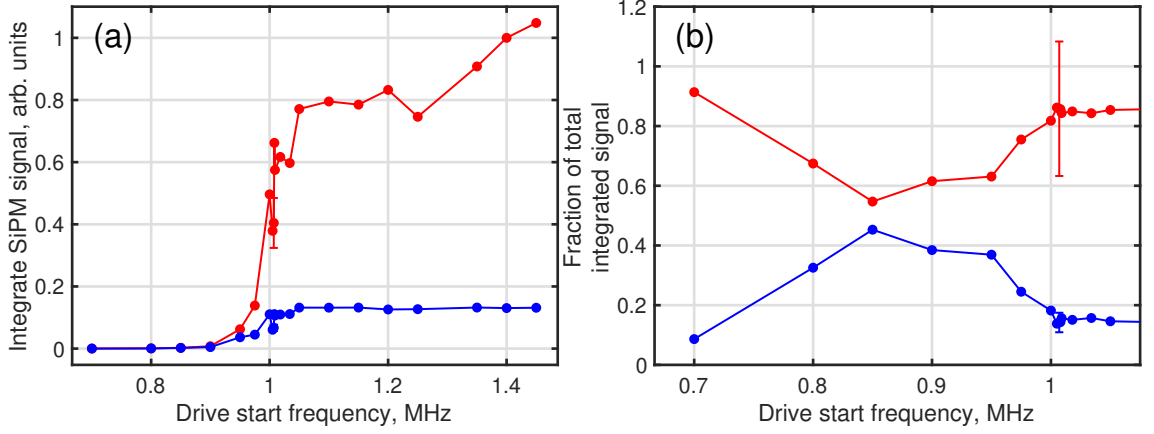
Figure 5.7: (a) Integrated particle ejection signals for various AR chirp start frequencies, with other AR chirp parameters fixed. SiPM signals are taken from Figure 5.6. Red dots show the integrated ejection signal during the AR chirp, and the blue dots show the integrated ejection signal during the well depth cut. (b) Fraction of the total integrated ejection signal measured during either of the specified periods of time.

Meanwhile, the well depth cut period exhibits both increasing peak magnitudes and sudden changes in features.

As a side note, the 1.2×10^7 positive ion plasma measurements have not been presented here. However, it is worth mentioning their contrasting particle ejection signals during an AR chirp. In those measurements, only one to three peaks of ejected particles were observed during an AR chirp, and these peaks were smoother and lacked minor features, unlike the ones shown in this section.

5.5 Time-of-flight of remaining particles

The composition of the ion mixture remaining after both the AR chirp and well depth cut was determined using the time-of-flight method mentioned in Section 4.6. However, these measurements were acquired using a SiPM, as detailed in Section 2.5.3.

Figure 5.8 shows the time-of-flight measurements, which complement the chirp parameter scans shown in Section 5.4. Except the chirp amplitude scan includes 5 V_{pp}, and the chirp start frequency scan includes 1.5 MHz. The signals in plots (a) and (b) have a common vertical scale and are stacked vertically by ascending chirp amplitude and chirp start frequency, respectively. The common vertical scale factors differ between (a) and (b) because (b) contains more signals.

After the AR chirp and well depth cut, the remaining positive ions were held for 50 ms before being ejected for a time-of-flight measurement. This waiting period allowed the remaining population to thermalise, removing the possibility of secondary peaks from non-ejected axially excited particles.
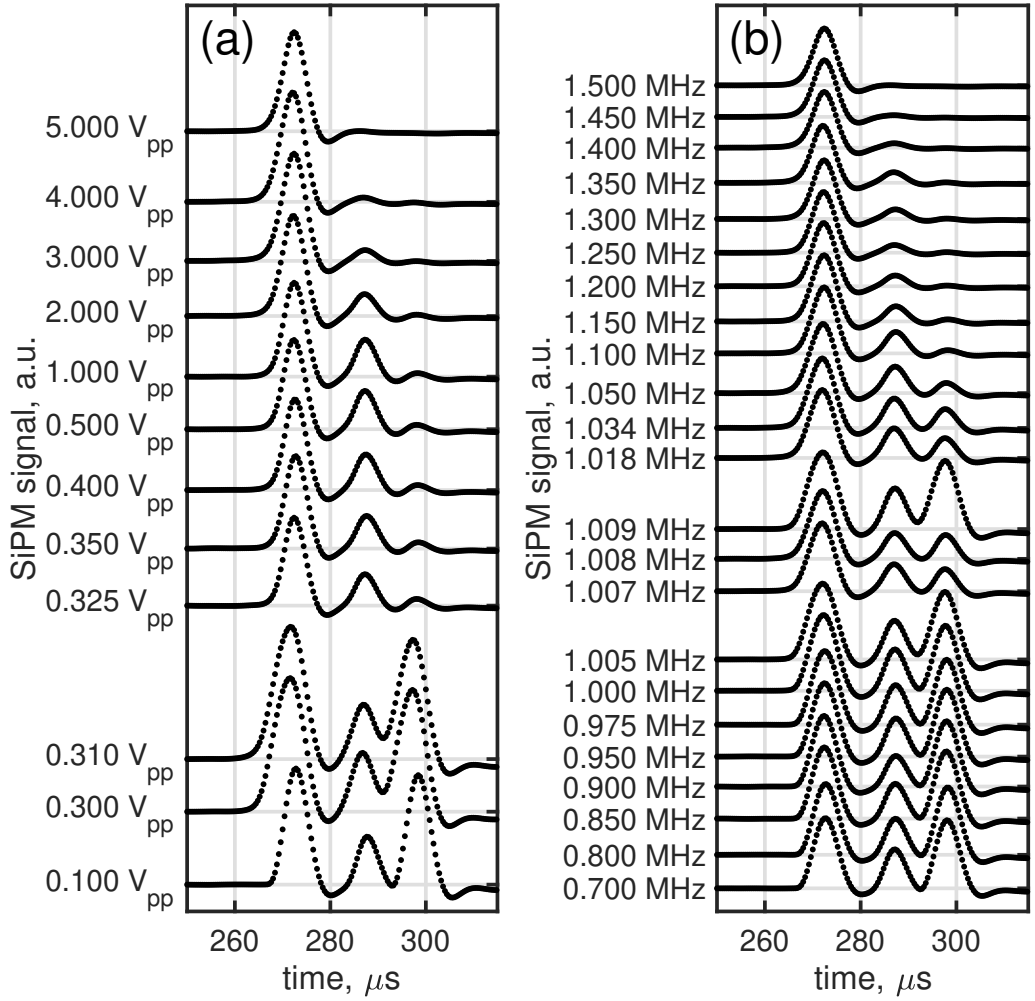
Figure 5.8: (a) Time-of-flight signals of various AR chirp amplitudes with fixed AR chirp parameters: $\omega_i = 1.5$ MHz $\omega_f = 0.1$ MHz and $\alpha = 200$ MHz s^{-1}. (b) Time-of-flight signals of various AR chirp start frequencies with fixed AR chirp parameters: $\bar{\epsilon} = 5$ V$_{\mathrm{pp}}$, $\omega_f = 0.1$ MHz and $\alpha = 200$ MHz s^{-1}. The labels adjacent to each signal correspond to its AR chirp parameter value.

As mentioned earlier, these measurements were acquired by measuring the phosphorescence light from the MCP instrument using a SiPM sensor. This sensor's electrical signal was amplified and filtered by the silicon photomultiplier hardware and further amplified and filtered by an SRS model SR560. The MCP operating voltages for these measurements were chosen to prevent voltage saturation of peaks. This electronics setup distorts the particle current signal, causing undershooting after the first peak at the 280 μs marker in both Figure 5.8 (a) and (b), as the amplitude decreases below the initial background level. This undershooting is noticeable after the first and third peaks.

It is difficult to obtain qualitative information from these signals due to the poorly characterised undershooting present in them. This has led to the use of a deconvolution method in the following section, which aims to eliminate this circuit response. The time scale of particle ejection is constrained by the electrode power supply elec-

tronics, measured to be around 10 μs. As a reminder, Section 4.6 identified the three positive ion peaks: protons, H_2^+, and H_3^+ (from left to right in Figure 5.8). The composition of positive ions evidently changes due to the AR chirp and well depth cut.

First, consider the chirp amplitude scan shown in Figure 5.8 (a). A single threshold is noticeable when the H3$^+$ peak nearly vanishes, occurring between 0.31 Vpp and 0.325 Vpp. This differs from the two chirp amplitude thresholds observed in Section 5.4 at 0.1-0.3 Vpp and 0.35-0.4 V_{pp} during the well depth cut and AR chirp, respectively. The reason for this discrepancy remains unclear.

Further increasing the chirp amplitude does not produce any similar effect on the H_2^+ peak. Instead, as the chirp amplitude increases, the H_2^+ peak gradually diminishes, and the residual H_3^+ peak decreases until both eventually disappear at 5 Vpp. The proton peak seems to decrease with increased chirp amplitude, suggesting some proton losses.

Next, examining the chirp start frequency scan in Figure 5.8 (b), the chirp begins to affect H_3^+ ions with a start frequency of 1.007 MHz, seen as its peak magnitude decreasing. However, the onset start frequency threshold is seen to vary on the order of 2 kHz. As an example the signal for a start frequency of 1.009 MHz did not show a response to the chirp, unlike the two signals of 1.007 MHz and 1.008 MHz. This could be due to variations in the prepared positive ion plasma. Increasing the chirp start frequency causes all three peaks to decrease smoothly, leaving only the proton peak after a start frequency of 1.5 MHz. In Section 5.4, three different chirp start frequency thresholds are observed: 0.95 MHz, 1.008 MHz, and 1.034 MHz. The previously observed 1.008 MHz threshold might correspond to the 1.009 MHz threshold seen in the time-of-flight measurements. Nonetheless, the differences in response between time-of-flight and previous ejection signals during the AR chirp and well depth cut have yet to be explained.

5.6 Time-of-flight analysis

5.6.1 Deconvolution Algorithm

The presence of undershooting in time-of-flight measurements during the chirp parameter scans makes it challenging to accurately quantify changes in the positive ion plasma composition due to the AR chirp, as previously discussed in Section 5.5 and observed in the raw measurements in Figure 5.8. If this undershooting represented a genuine particle signal, positive ions would have to accumulate on the detector phosphor surface, which is at a 5 kV DC. This high voltage barrier would clearly deflect positive ions, allowing only the electron avalanche to be collected.

An appropriate post processing method is needed to deconvolve the particle cur-

rent from the measured signals. Assuming that the total circuit behaves linearly the method of impulse response functions, as described in [101], can be used. This Fourier deconvolution algorithm expresses the measured signal s_m as a convolution of the unknown input signal s and a circuit specific impulse response function $H(t)$:

$$s_m(t) = H(t) \circledast s(t). \tag{5.1}$$

By Fourier transforming $s_m(t)$ from the time domain t into frequency domain f, the convolution operation $\circledast$ will function as a product operation:

$$\overline{s_m}(f) = \overline{H}(f) \times \overline{s}(f) \tag{5.2}$$

$$\overline{H}(f) = \frac{\overline{s_m}(f)}{\overline{s}(f)}, \tag{5.3}$$

where the overline denotes the Fourier transform of the function, i.e. $\overline{s_m}(f) = \mathcal{F}[s_m(t)]$. In practise, this method is used by injecting a narrow Gaussian electrical pulse, shorter than the response time of a circuit, into a circuit. The measured output signal is $\overline{H}(f)$. This method works because a narrow Gaussian pulse approximates a Dirac delta function, and the Fourier transform of a Dirac delta function is a normalised uniform distribution. However, in this work, both the input signal $s_i(t)$ and the circuit response $H(t)$ are unknown.

Technical specifications of the circuit were not obtainable, which was custom made, and access to the circuit was limited. To further this analysis, some informed guesses had to be made. The chosen approach involved selecting an appropriate functional form G as the input particle current, with a set of undetermined parameters $\{a_j\}$. An appropriate measure of error also had to be chosen. There are a total of 58 time-of-flight measurements, $s_m(t)$, within the chirp parameter scans.

An algorithm was needed determine the impulse function $H(t)$ for a chosen functional form G. First, a specific measured signal from the set $s_m(t)$ had to be chosen. The signals shown in Figure 5.8 are composed of one to three peaks. The functional form was chosen to be suitable for a single peak, with multi-peak curves formulated by summing the functional form multiple times, each with independent parameters. To reduce complexity and the dimensionality of the parameter space, a measurement with an apparent single peak structure was chosen. This chosen signal peak is from an AR chirp with an amplitude of 5 V_{pp} and a start frequency of 1.5 MHz, and the signal is denoted $s_1(t)$.

The deconvolution algorithm implemented is as follows:

Suitable initial guess values for $\{a_i\}$ were determined using the peak information from the chosen signal $s_1(t)$. A transfer function $H(t)$ was computed based both on the specified signal $s_1(t)$ and the guess curve $s_G(t; \{a_j\})$. This transfer function was used to deconvolve all 58 signals into a set of input signals. The parameters of

---

Algorithm 1: Fourier Decomposition

    Data: $s_m(t)$,G
    ;   // Measured output signal, $s_m(t)$ and input signal functional form, G.
1 Assign Threshold;
2 Calculate $\{\overline{s_m}(f)\} \leftarrow \mathcal{F}[\ \{\ s_m(t)\}\ ]$;   // Fourier transform of the set of measured signals
3 Assign $\{a_j\}$;   // Guess function G parameters
4 **while** *Error > Threshold* **do**
5   Calculate $s_G(t) \leftarrow G(\{a_j\};t)$;   // Guess input signal of $s_1(t)$
6   Calculate $s_G(t) \leftarrow \mathcal{F}[\ s_G(t)\ ]$;   // Fourier transform of $s_G(t)$
7   Calculate $\overline{H}(f) \leftarrow \overline{s_1}(f)/\overline{s_G}(f)$;
8   Calculate $\{\overline{s_{m,D}}(f)\} \leftarrow \{\overline{s_m}(f)\}\ /\overline{H}(f)$;   // Deconvolve set of measured signals
9   Calculate $\{s_{m,D}(t)\} \leftarrow \mathcal{F}^{-1}[\ \{\overline{s_{m,D}}(f)\}\ ]$;   // Inverse Fourier transform of the deconvolved signals
10   Calculate *Error* ;
11   **if** *Error < Threshold* **then**
12   Update $\{a_j\}$;   // Adjust function G parameters accordingly

---

the same functional form G were fitted to all calculated input signals, within the 260 - 330 μs signal time period during which all three peaks appear, using the least squares method. This restricted signal time period for the fit was done to improve computational time of the error calculation.

The three peak functional form of G was fitted to each of the deconvolved signals $s_{s,D}(t)$. The root-mean-square error of the fit and the deconvolved signal was calculated, and all 58 error values were summed into a single global error. This global error was used with a gradient descent method to obtain parameters $\{a_j\}$ that minimises the global error.

5.6.2   Maxwell-Boltzmann time-of-flight distribution function

Next, it is essential to determine an appropriate functional form for the input signal. It's structure should reflect the dynamics of particles ejected from the trap. These dynamics include thermal, electrostatic, magnetostatic, collisional, and trap electronic dynamics. However, considering all of these dynamics is beyond the scope of this thesis, so a simplified approach was to treat the ejected plasma as a charge-neutral gas. This charge-neutral gas travels a distance L from the trap region towards the detector, with a Maxwell-Boltzmann energy distribution offset by a common ejection energy U. The Maxwell-Boltzmann distribution in one-dimensional

velocity space v_T, with temperature T, is given by:

$$N(v_T)\mathrm{d}v_T = \sqrt{\frac{m}{2\pi k_B T}} \exp\left(-\frac{m v_T{}^2}{2k_B T}\right) \mathrm{d}v_T, \tag{5.4}$$

where $N(v_T)$ is the one-dimensional velocity probability density function, m is the species mass and k_B is Boltzmann's constant. A particle's arrival time t across a distance L is given by:

$$t = \frac{L}{v_T + v_{dump}} \tag{5.5}$$

Here, v_T is the thermal velocity component and v_{dump} is the electric potential ejection velocity component. This relationship maps the thermal velocity to arrival time. So the thermal velocity can be expressed as:

$$v_T = {}^{L}/_{t} - v_{dump} \tag{5.6}$$

$$\left|\frac{\mathrm{d}v_T}{\mathrm{d}t}\right| = \frac{L}{t^2}. \tag{5.7}$$

The temporal probability density distribution $N(t)$ is related to its one-dimensional velocity counterpart by the relationship

$$N(v_T)\mathrm{d}v_T = N(t)\mathrm{d}t. \tag{5.8}$$

Using Equations 5.4, 5.6, 5.7, and 5.8, $N(t)$ can be expressed as:

$$N(t; L, v_{\mathrm{dump}}, v_0) = \frac{L}{\pi v_0 t^2} \times \exp\left(-\left[\left(\frac{v_{\mathrm{dump}}}{v_0}\right) \times \left(\frac{L}{v_{\mathrm{dump}} t} - 1\right)\right]^2\right), \tag{5.9}$$

where the mean thermal velocity is $v_0 = \sqrt{\frac{m}{2k_B T}}$. This can also be expressed in the one-dimensional energy form:

$$N(t; L, U, T) = \sqrt{\frac{m}{2\pi k_B T}} \times \frac{L}{t^2} \times \exp\left(-\frac{qU}{k_B T}\left[\sqrt{\frac{m}{2qU}}\frac{L}{t} - 1\right]^2\right), \tag{5.10}$$

where the ejection electric potential $U = m \times v_{dump}^2/(2q)$. The maximum amplitude of $N(t; L, U, T)$ occurs at time:

$$t_{\mathrm{max}}(L, U, T) = \frac{L}{v_{\mathrm{dump}}} \times \frac{qU}{2k_B T} \times \left(\sqrt{\frac{4k_B T}{qU} + 1} - 1\right). \tag{5.11}$$

Since the average thermal energy of plasma within this work is smaller than the ejection energies, then the square-root in Equation 5.11 can be approximated as a

Taylor series, so that:

$$t_{\max}(L, U, T) \approx \frac{L}{v_{\text{dump}}} \times \left(1 - \frac{k_B T}{qU} + \cdots\right). \tag{5.12}$$

This form is clearly a perturbation series from a typical projectile time-of-flight L/v_{dump}, where any non-zero temperature will cause the peak arrival time to occur earlier.

The zero time in the measured time-of-flight signal does not correspond with the particle ejection from the trap and other time delays will influence this, such as ramping speeds of the electrode's power supply, the transit time for electric signals along control cables, and readout. To account for this, a time offset parameter t_{offset} is included in the fit. To fit the derived probability density function, Equation 5.10, to a signal its amplitude needs to be parametrised. This was done by normalising the distribution function with respect to its peak amplitude at $t_{\max}$, and multiplying it by an amplitude parameter N_{peak}. This gives us the Maxwell-Boltzmann time-of-flight (MB-ToF) distribution function,

$$N_{\text{fit}}(t; L, U, T, N_{\text{peak}}, t_{\text{offset}}) = N_{\text{peak}} \times \frac{N(t - t_{\text{offset}}; L, U, T)}{N(t_{\max}(L, U, T); L, U, T)}. \tag{5.13}$$

This is a single peak curve, in positive time ($t > 0$), and has 5 parameters. If the entire plasma is ejected from the trap simultaneously, all particles will share both a common time offset t_{offset} and a common ejection energy U. This reduces the three peak fit parameters from 15 down to 11. A fit that restricts all ions to one common temperature was attempted, though this produced poor fits and was abandoned. The reasons for the poor fitting is not entirely understood, as physical dynamics not captured in the model could be responsible. In order to proceed with the analysis, each ion species was given an independent temperature, leading to interesting properties discussed later in Section 5.6.3.

To reduce the computational times, bounds were applied during the fitting process. The ejection position of the particles was determined by calculating the electric potential barrier positions of the vacuum potential well experienced by the particles during ejection. These calculations yielded two extrema positions for ejection with respect to the Catching Trap electrode stack. These positions and available apparatus drawings were used to determine approximate bounds on the distance L traveled by the ejected particles. Similarly, the ejection energy U was bounded by the same calculations of the vacuum electric potentials. These constraints ensure that the fit parameters fall within physically reasonable values.

Without these constraints, the error-minimising fit ejection energies U would decrease to 100 eV, which is not physically reasonable. The other optimal parameters remain unchanged with or without these constraints. The parameter bounds used

for the later MB-ToF fits are shown in Table 5.6.2. The label '*i*' denotes parameters associated with one of the three peaks, while the 'lower' and 'upper' labels refer to the bounds applied to other parameters.

Parameter	L (m)	U (eV)	T_i (K)	$N_{\text{peak},i}$	t_{offset}
lower bound	5.080	108.2	1,000	0	$t_{\text{peak},i} - L_{\text{lower}}\sqrt{\frac{m_i}{2qU_{\text{upper}}}}$
upper bound	5.091	123.5	20,000	$1.5 \times N_{\text{max},i}$	$t_{\text{peak},i} - L_{\text{upper}}\sqrt{\frac{m_i}{2qU_{\text{lower}}}}$

Table 5.1: Maxwell-Boltzmann time-of-flight parameter fit bounds.

5.6.3 Deconvolution and fit analysis

Within the set of time-of-flight measurements, there are two extrema cases: signals with a single peak and signals with three peaks. The first row of Figure 5.9 (a,b) shows examples of these two extrema. Gaussian curves have been fitted to regions indicated by their length to each peak, this is to demonstrate how an analysis of these raw signals could be carried out. The later portion of each peak undershoots, which a Gaussian curve fails to fit, so this analysis rejected those later points. Although Gaussian curves are a good fit, they require a background level as a free parameter. This causes minor features of the undershooting to be misidentified as ion peaks. The remaining two lower rows of the Figure 5.9 display the results of the previously mentioned deconvolution algorithm (see Algorithm 1), separately using a Gaussian functional fit and a MB-ToF functional fit. As a reminder, the transfer function $H(t)$ is calculated from a single peak signal $s_1(t)$ and a guess input signal with the same functional form as the fit function. As a result, when signals similar to $s_1(t)$ are deconvolved, the guest input signal will be calculated. This means that the deconvolved signals in (d) and (f) are a forced condition by the use of this algorithm. Conversely, the triple peak signals will exhibit distortions different from the initial undershoot feature. The Gaussian deconvolution appears to remove the undershoot feature and instead distorts the signal prior to the peak, though to a lesser extent. The MB-ToF deconvolution exhibits more significant distortion than the Gaussian deconvolution for triple peak signals, comparing (e) and (c), respectively.

The same deconvolution and fitting method shown in Figure 5.9 was performed on all time-of-flight signals, specifically the two chirp parameter scan sets shown in Figure 5.8.

The parameters obtained using the Gaussian functional fit are shown in Figure 5.10 for various AR chirp start frequencies. As the triple fit function is simply the sum of three single peak fits, the contribution of each individual peak within the fit can
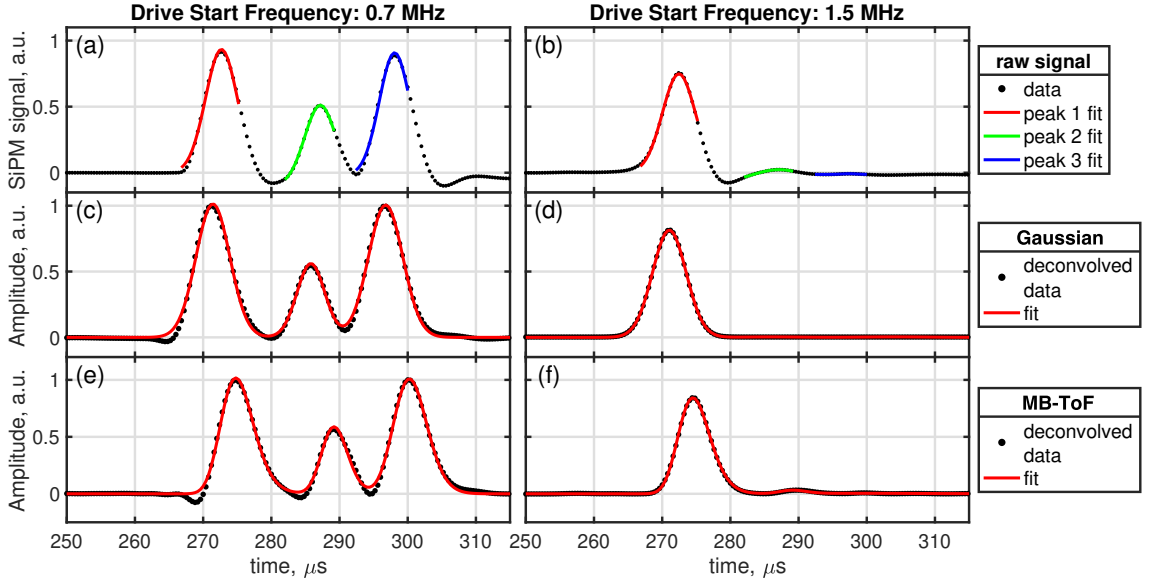
Figure 5.9: The extrema limits of the chirp start frequency scan time-of-flight measurements. The left column is the lower extreme (0.7 MHz) and the right column is the upper extreme (1.5 MHz). Each row presents examples from different analyses. (a) and (b) are the raw measured signals with three independently fitted background offset Gaussian distributions. (c) and (d) are post-processed signals with an assumed Gaussian impulse, shown as black dots. The residual minimising triple Gaussian distribution fit is shown as a red line. (e) and (f) are the post-processed signals with an assumed MB-ToF impulse, shown as black dots. The residual minimising triple MB-ToF distribution fit is shown as a red line.

be extracted. This allows for the integration of each peak and the calculation of the fractional contribution of each peak to the total signal. The integrated peaks and fractional contributions are shown in Figure 5.10 (d) and (e), respectively.

Both the amplitude (a) and integrated peaks (d) clearly show the threshold start frequency of the AR chirp, which begins to drive all three species, as previously discussed in Section 5.5. The H_3^+ ion peak decreased to 6-7% of both its initial amplitude and integrated peak value for a chirp start frequency of 1.1 MHz. In contrast, the H_2^+ ion peak does not decrease sharply but exhibits an near linearly decline. Similarly, the proton peak decreases linearly, but with a shallower gradient. As shown in (e), the signal becomes dominated by the proton peak as the chirp start frequency approaches 1.5 MHz.

The Gaussian centers in (b) are approximately 271 μs, 286 μs and 296 μs, with sub-microsecond variations. For frequencies below the start frequency threshold, both the proton and H_3^+ ion peaks have similar full-width-half-maxima (FWHM) as shown in (c), while the H_2^+ ion peak's FWHM is the narrowest. For frequencies larger than the start frequency threshold the H_3^+ FWHM changes to a value similar to H_2^+. This shared FWHM behaviour is not well understood. The FWHM of the proton peak near the threshold start frequency 1.1 MHz, increases sharply, which is also not understood, and results in a sharp feature appearing in the integrate peak

Figure 5.10: Gaussian fit parameters, obtained by a residual minimiser applied to the deconvolved start frequency scan data. Black, blue and red dots are the proton, H_2^+ and H_3^+ peaks, respectively. The Gaussian fit parameters: amplitude, center time, full-width-half-maxima (FWHM), are shown in (a), (b), and (c), respectively. The integrated intensity of each Gaussian fit is shown in (d). The fractional amount of each ion species is shown in (e), this is the ratio of the integrated intensity to the summed integrated intensity of all ion species.

value shown in (d).

The fit parameters obtained using the MB-ToF functional fit are plotted in Figure 5.11 versus the chirp start frequency. The behaviour in each peak's response to the chirp start frequency shown in (a) and (e) is the same as previously discussed for Figure 5.10. Instead, focus on the parameters unique to this fit, such as release time, dump energy, and temperature. The release time only varies by about 1 μs, which could suggest an alternative analysis that fixes its value. The dump energy varies significantly across the scan, as seen in (c). For frequencies larger than the start frequency threshold, it reaches the lower bound value. This may be due to the reduced space charge of the plasma caused by the removal of positive ions by the AR chirp. Each peak was fit with independent temperatures, as shown in (d). Both the H_2^+ ion and H_3^+ ion peaks share the same temperature, but the proton peak is almost three times larger. This seems to contradict the assumption that the plasma
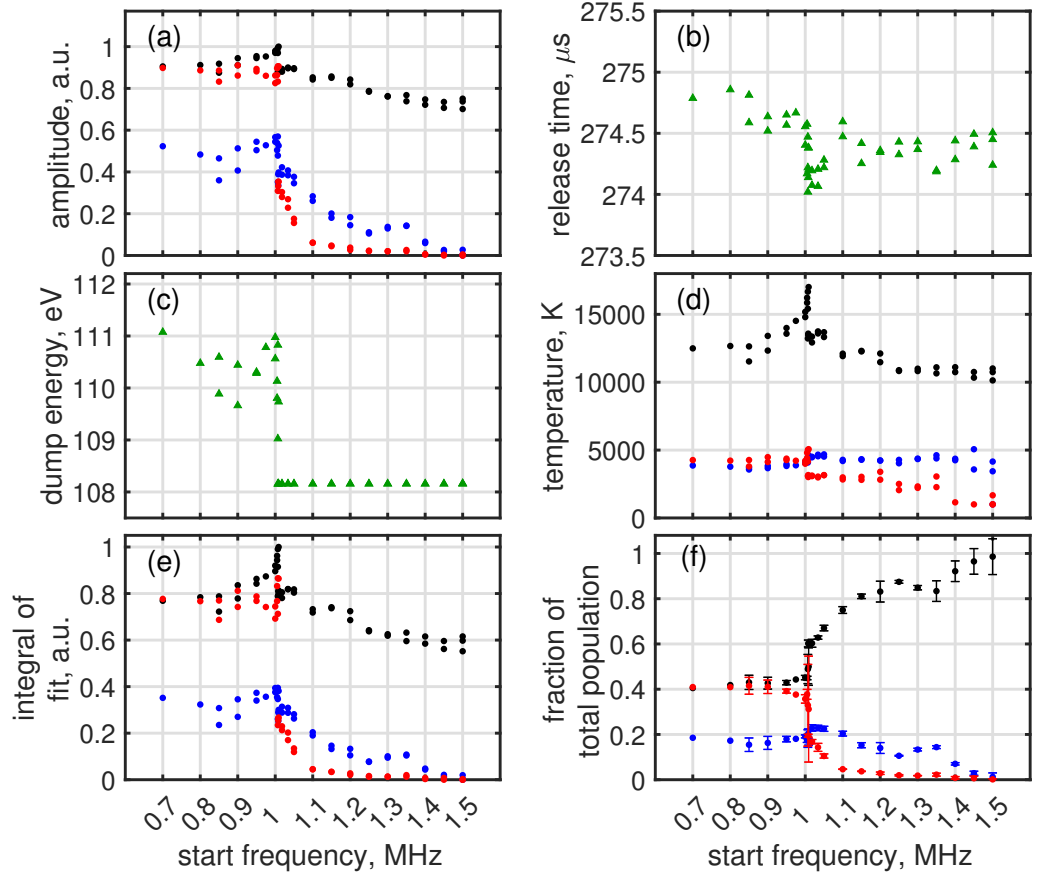
Figure 5.11: MB-ToF fit parameters, obtained by a residual minimizer applied to the deconvolved start frequency scan data. Black, blue, and red dots are the proton, H_2^+ ion, and H_3^+ ion peaks, respectively, while green triangles denote parameters shared by all three fits. The MB-ToF fit parameters: amplitude, release time, dump energy and temperature, are shown in (a), (b), (c), and (d), respectively. The integrated intensity of each MB-ToF fit is shown in (e). The fractional amount of each ion species is shown in (f), this is the ratio of the integrated intensity to the summed integrated intensity of all ion species.

is in thermal equilibrium.

The parameters obtained using the Gaussian functional fit are shown in Figure 5.12 against the chirp amplitude. The peak amplitude of the species does not change monotonically with the chirp amplitude, as seen in (a), (d), and (e). The particle signal initially increases with the chirp amplitude until it crosses the chirp amplitude threshold. After crossing the threshold, all three peaks decrease, and the H_3^+ ion peak decreases to 6-8% of its initial amplitude and integrated peak value. Following this threshold, the proton peak signal increases with the chirp amplitude, while the H_2^+ ions and H_3^+ ions signal monotonically decreases. The chirp amplitude threshold is discussed in Section 5.5.

The MB-ToF functional fit was also applied to the chirp amplitude scan data, as shown in Figure 5.13. This alternative fit function reveals a response similar to the chirp amplitude. The fitted peak temperatures are consistent with the analysis
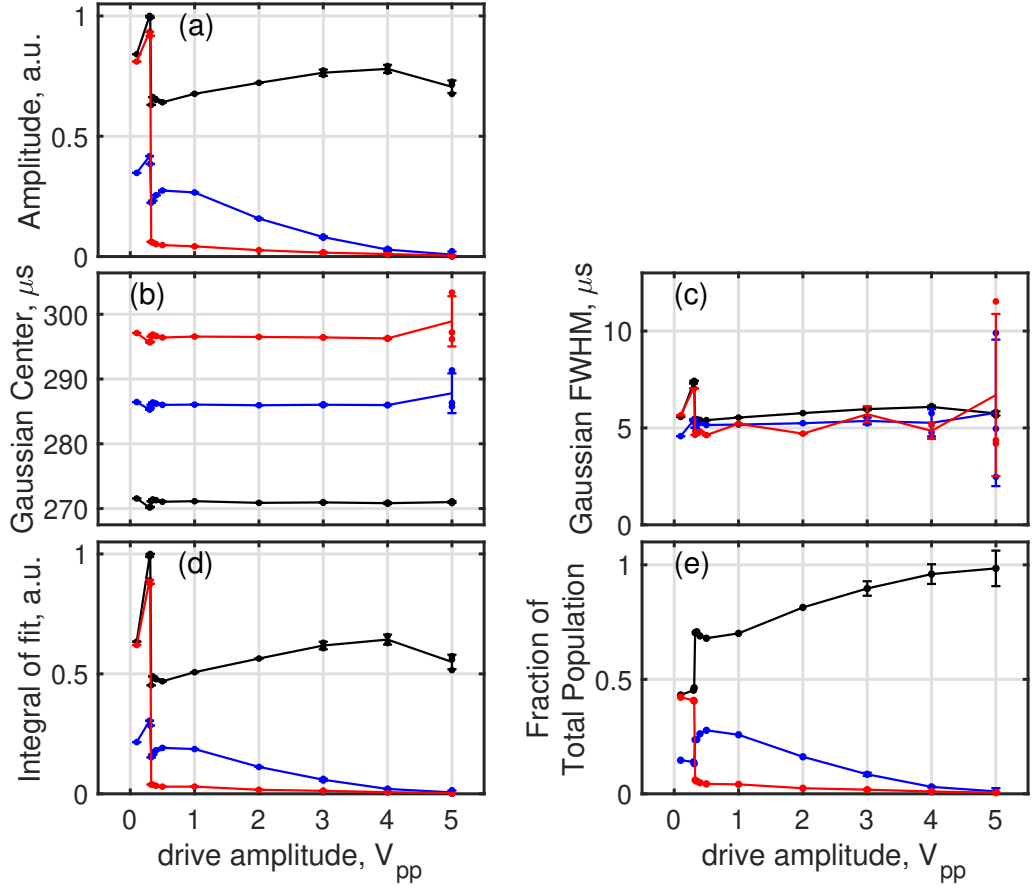
Figure 5.12: Gaussian fit parameters, obtained by a residual minimiser applied to the deconvolved chirp amplitude scan data. Black, blue and red dots are the proton, H_2^+ and H_3^+ peaks, respectively. The Gaussian fit parameters: amplitude, center time, full-width-half-maxima (FWHM), are shown in (a), (b), and (c), respectively. The integrated intensity of each Gaussian fit is shown in (d). The fractional amount of each ion species is shown in (e), this is the ratio of the integrated intensity to the summed integrated intensity of all ion species.

of the chirp start frequency set, as the H_2^+ and H_3^+ temperatures fit to similar values and the proton peak is the hottest. The fit temperatures of H_2^+ and H_3^+ range from 2000 K to 6000 K, significantly higher than the actual temperature diagnostic measurements of 1500 K before an AR chirp. Moreover, the correlation matrix, approximately calculated from the Jacobian matrix of each fit, has off-diagonal elements that measure the correlation between the temperature parameters to be nearly one. This indicates that the fitted temperatures are directly related, although the reason for the proton temperature scaling by nearly a factor of two compared to the other two ion species remains unclear. Consequently, the temperature parameter cannot be considered accurate.
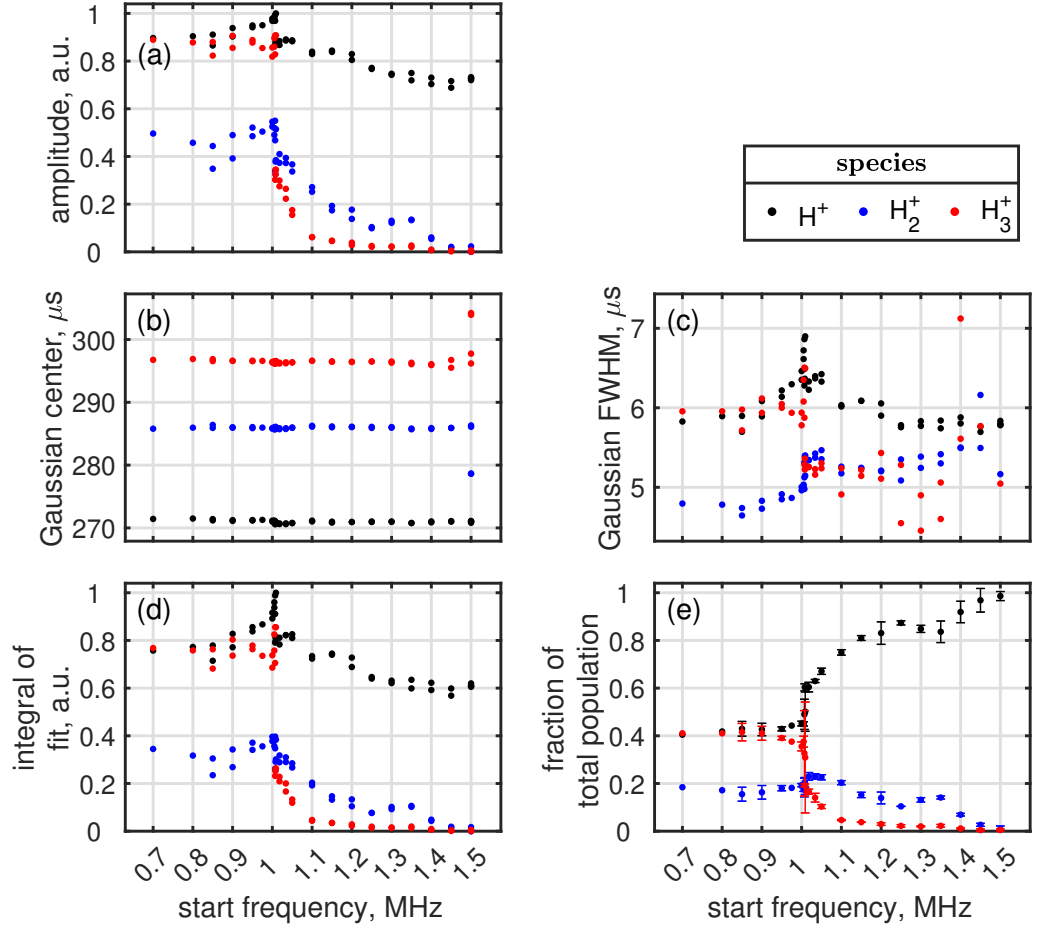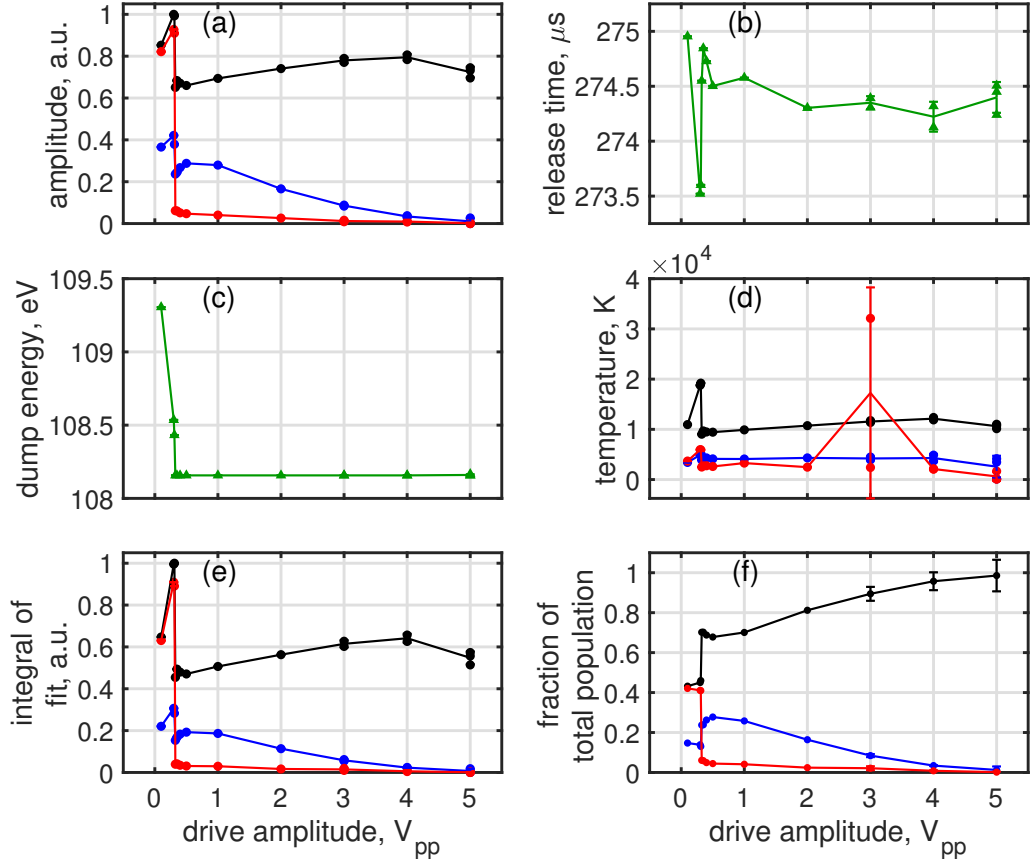
Figure 5.13: MB-ToF fit parameters, obtained by a residual minimiser applied to the deconvolved chirp amplitude scan data. Black, blue and red dots are the proton, H_2^+ and H_3^+ peaks, respectively. Green triangles are parameters shared by all three fits. The MB-ToF fit parameters: amplitude, release time, dump energy and temperature, are shown in (a), (b), (c), and (d), respectively. The integrated intensity of each MB-ToF fit is shown in (e). The fractional amount of each ion species is shown in (f), this is the ratio of the integrated intensity to the summed integrated intensity of all ion species.

5.6.4 Change in composition due to AR chirp

The calculated impulse functions $\overline{H}(f)$ were used to analyse time-of-flight measurements using the same sequence, except without an AR chirp. These are called the 'initial population distribution', as analysis was used to estimate the initial fractional composition of each species. The subset of signals with the chirp parameters: $\omega_i = 1.5$ MHz, $\omega_f = 0.1$ MHz, $\bar{\epsilon} = 5$ V_{pp} and $\alpha = 200$ MHz s^{-1}, is called the 'proton plasma' population. The corresponding statistical mean and standard statistical errors are presented in Table 5.6.4. Both Gaussian and MB-ToF fits produce consistent values for each population fraction, except for the H_3^+ fraction, which is non-zero for the Gaussian fit. This may indicate a small remaining H_3^+ population, though dominated by protons.

Measurements for both chirp parameter scans were performed on September 19 and 20, 2020 (see Figure 4.10). The total population of positive ions in plasma

	initial population distribution			'proton plasma' population distribution		
Species	proton [%]	H_2^+ [%]	H_3^+ [%]	proton [%]	H_2^+ [%]	H_3^+ [%]
MB-ToF	43.2 ± 1.1	16.8 ± 1.7	40.0 ± 1.5	98.6 ± 7.9	1.3 ± 1.8	0.2 ± 0.3
Gaussian	42.9 ± 1.3	16.5 ± 1.7	40.5 ± 1.4	98.6 ± 1.4	0.9 ± 1.2	0.5 ± 0.3

Table 5.2: The fraction of each species with respect to the total population signal, obtained using either a Gaussian fit or an MB-ToF fit. The 'initial population distribution' values were calculated from the subset of signals without an applied chirp. The 'proton plasma' population distribution values were calculated from the subset of signals with the chirp parameters: $\omega_i = 1.5$ MHz, $\omega_f = 0.1$ MHz, $\bar{\epsilon} = 5$ V_{pp}, and $\alpha = 200$ MHz s^{-1}. Errors are standard deviations.

was found to be $(3.0 - 3.4) \times 10^6$, limiting the initial population size of protons to $(1.2 - 1.5) \times 10^6$. No Faraday cup measurement was performed on the remaining population due to time constraints. However, assuming that the integral of the proton peak in the time-of-flight signal is linearly proportional to the number of protons, the remaining proton population is 76 ± 1 % of the initial proton population, which is between $(0.9 - 1.2) \times 10^6$ protons.

5.7 Radial distribution post AR sequence

In addition to time-of-flight measurements, the positive ion plasma was imaged with the MCP instrument following the AR chirp and well depth cut. Measurements were performed during both the AR chirp start frequency and AR chirp drive amplitude scans. Figure 5.14 shows a selection of images that highlight notable changes in the plasma, which were partially observed in time-of-flight measurements. The positive ion species appear as at least two overlapping regions of different sizes, most prominently visible in (a) and (e).

The top row of Figure 5.14 shows select images from the AR chirp amplitude scan.
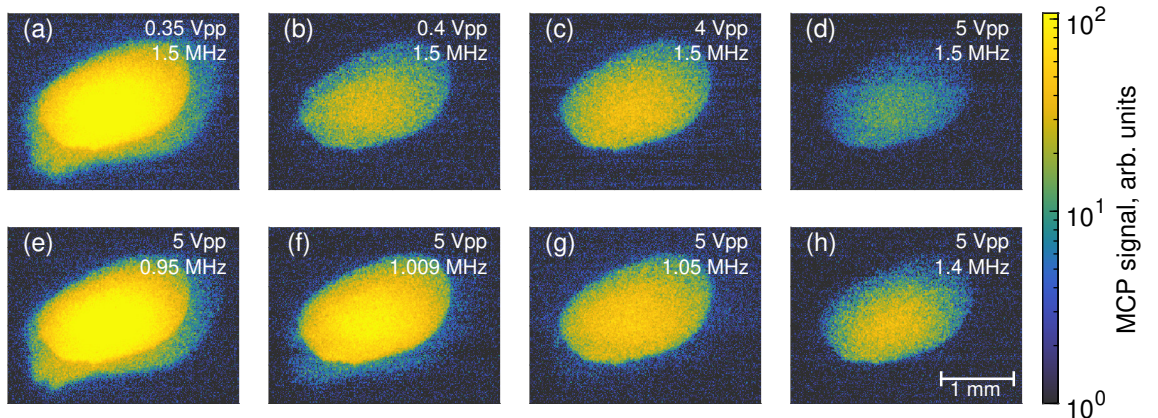
Figure 5.14: MCP signals sampled from both the chirp amplitude scan (a,b,c,d) and the chirp start frequency scan (e,f,g,h), all with a common log-scale colour map.

The largest particle region disappears with a 50 mV$_{pp}$ increase in chirp amplitude between (a) and (b), leaving only one distinguishable particle region in image (b). The remaining smaller region is believed to consist of both protons and H$_2^+$ ions, as both populations cannot be differentiated. As the chirp amplitude increases, the remaining particle region becomes sparser.

The bottom row of Figure 5.14 presents images from the frequency scan of the chirp start drive, which reveal only two distinct particle regions. As the chirp start frequencies increase from (e) to (h), the transition between coupling none, some, and all particles in the largest region's nonoverlapping area is observed. The optimal AR chirp configuration is shown in (d), appearing sparse, which aligns with the corresponding time-of-flight measurements, indicating loss of the proton population in addition to the intended removal of all other species.

5.8 Isolated protons

After optimising the AR chirp and well depth cut, the remaining protons were radially diffuse, as shown in Figure 5.15 (b). Two temperature measurements were obtained, 1.4×10^4 K and 1.5×10^4 K. The protons were radially compressed by mixing it with a second bunch of positrons and then applying a rotating wall, this was done to improve the MCP signal of the protons, this also provided sympathetic cooling to reduce the proton temperature. A second bunch of positrons was accumulated and transferred to the Atom Trap while the initial positron bunch was in the Catching Trap. Once the protons were obtained, they were moved to the
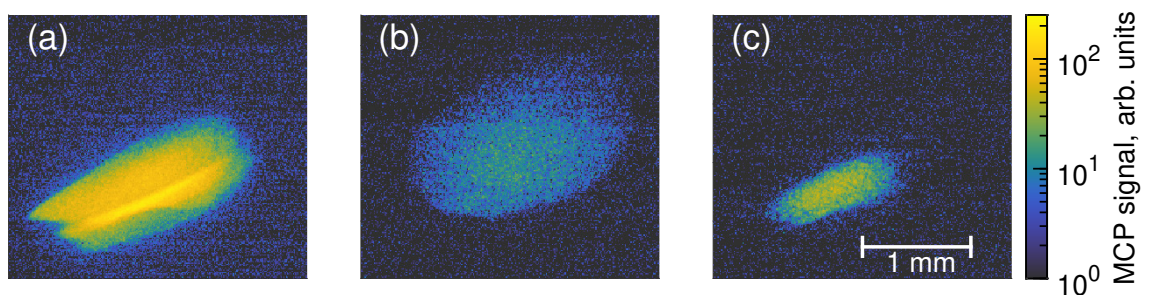
Figure 5.15: Chronologically ordered MCP images with a log-scale colour map. (a) A positive ion mixture before applying any AR drive. (b) The remaining proton population after optimal AR drive and well depth cut. (c) Protons after mixing with a 'clean' positron population and sympathetically compressed. The scale bar is common across (a), (b) and (c), this corresponds to distances within the trap region.

upstream side of the Catching Trap, and the remaining unused electrodes were used to capture the second positron bunch. This second bunch was 'cleaned' of positive ions using a heating signal that repeatedly swept across the axial frequencies of all

positive ions. The remaining positrons and protons were mixed by merging their two potential wells and then radially compressed using the rotating wall method. Figure 5.15 (b,c) shows the uncompressed and compressed protons, respectively, after removing the second positron bunch with the electron kicking method discussed in Section 2.2.2.

The compressed protons have a temperature of 3.1×10^3 K. Only one temperature measurement was performed, but its accuracy is not of significant importance.

This represents the latest development in the ALPHA apparatus and is a successful demonstration of the proton source method.

5.9 Conclusion

The isolation of protons from the positive hydrogen ions plasma can be achieved using the autoresonance technique. Autoresonance, a phenomenon of ion motion coupling to an externally oscillating electric field generated by an oscillating voltage applied to an electrode, is a common occurrence in ions trapped within a Penning trap. Autoresonance can escalate the axial kinetic energy close to ejection energies, albeit insufficiently for the driven ions to escape the trap. When the axial kinetic energy is near the ejection energy, thermal fluctuations can stochastically cause ions to escape. To expedite the removal of driven ions from the trap, the depth of the electric well can be diminished. Lighter species possess higher axial frequencies compared to heavier species, enabling selective coupling of different ion species. However, when a targeted light species is driven towards lower axial frequencies, all heavier species will couple to the drive, leading to their removal. For instance, targeting H_2^+ will also remove H_3^+. In this study, the autoresonance technique was explored in positive hydrogen ion plasma to identify the drive parameters that could facilitate the removal of the majority of H_2^+ and H_3^+ ions, thereby producing an isolated proton plasma.

Predictions of the coupling frequencies for each species were made on the basis of the mass-to-charge ratio and the chosen potential well shape. Initial attempts with a shallower electric potential well revealed poor coupling between the target ions and the drive electric field. Using a deeper electric potential well, the coupling performance was improved, enabling the successful removal of H_2^+ and H_3^+ ions from the positive hydrogen ions plasma.

In a single-particle regime, the ion motion would be independent of other ions, leaving species above the initial drive frequency unaffected. However, in the plasma, lighter species were also observed to be ejected during the autoresonance drive, albeit with smaller coupling strengths. This study demonstrated that approximately $24 \pm 1\%$ of the initial proton population was ejected from the mixture along with the heavier hydrogen ions during the isolation sequence. The removal of H^+ and H_2^+

was observed for chirps with start frequencies ranging from more than 1 MHz, the resonant axial frequency of H_3^+, to less than their predicted resonant axial frequencies of 1.7 MHz and 1.2 MHz for H^+ and H_2^+, respectively.

Two hypotheses are proposed to explain why a fraction of H^+ is coupled and, consequently, ejected from the trap. The first possibility is that the calculated thermalisation timescale between positive hydrogen ions was overestimated, leading to a too-long drive duration during which driven ions could collide, transferring energy from the heavier driven species to protons. For a single ion at the initial temperature before the autoresonance (AR) chirp, the average time between collisions was estimated to be 3 ms. The duration of the final AR chirp is 7 ms, with an additional 1 ms prior to driven-particle ejection, allowing some collisions between protons and coupled ions to occur. These collisions would elevate the protons' kinetic energies, leading to some proton ejection during the well depth cut. However, the collision rate between protons and heavier ions remains unmeasured, rendering this hypothesis unconfirmed.

The second hypothesis suggests that protons are resonantly coupled with their subharmonic axial frequencies, which are expected to exhibit weaker coupling strengths, and hence coupling only a fraction of the proton population. Subharmonic coupling is observed in the signal of ions ejected during the AR chirp, as depicted in Figure 5.6. However, the strength of this effect is currently unknown. The spectra of the time of flight of the remaining ions are too complex to interpret, which makes this hypothesis difficult to confirm, as seen in Figure 5.8.

The optimised experimental protocol yields an isolated proton plasma of $(0.9 - 1.2) \times 10^6$ protons. The final parameters of the autoresonance chirp were a start frequency of 1.5 MHz, a final frequency of 0.1 MHz, a sweep rate of 200 MHzs^{-1}, and an amplitude of 5 V_{pp}. The AR trapping potential is set for electrodes C05 through C11 with the following voltage values: [140, 140, 140, -70, 120, 120, 50] Volts. All other electrodes are electrically grounded. These parameters are specific to the Catching Trap design. For experiments employing different Penning trap geometries, the optimal autoresonance parameters would need to be reassessed.

The isolated proton plasma can be sympathetically cooled with positron plasmas, mirroring the sympathetic cooling of antiprotons by an electron plasma, as documented in [102]. Preliminary attempts have yielded successful cooling and compression results. At this stage, the development of the isolated proton plasma can continue with techniques analogous to those used in antiproton plasma preparation for antihydrogen production. This gives promising prospects for atomic hydrogen production in the ALPHA apparatus.

Further discussion can be found in the conclusions in Chapter 6.

CONCLUSIONS AND FURTHER SCOPE

This research aimed to develop a method for adapting an existing Penning trap to produce protons on demand within reasonable time scales. Successful generation and tailoring of protons within minutes was demonstrated using the ALPHA apparatus, which features specialised hardware. However, researchers without access to such methods may still achieve similar results through modifications.

The generation of positive ions seems applicable to hydrogen-rich vacuums, commonly found in liquid helium cryogenic environments. Alternatively, an inlet for low-pressure hydrogen gas flow through a system might be suitable. Cooling and tailoring positive ion plasmas rely on the existing ALPHA positron accumulator, but alternative methods, such as buffer gas cooling, resistive cooling, or sympathetic cooling with neighbouring electrons, are possible. The first two methods require specialised redesigns or modifications to the Penning trap and its vacuum system, whereas the latter risk recombination, leading to the production of untrappable neutral atoms and molecules.

6.1   Conclusion

The purpose of generating protons within the ALPHA apparatus is for a variety of studies and calibrations that are typically performed with antiprotons. The availability of antiprotons is limited by the operational schedule of the Antiproton Decelerator facility. One such study could be the development of an antiproton reservoir within the Catching Trap, similar to the preparation of electron plasma involved in magnetometry measurements [38], to provide tailored bunches of antiprotons for the synthesis of antihydrogen. Another study is the optimisation of the magnet beamline calibration, Section 2.6, for efficient antiproton transfer between the Catching Trap and one of the antihydrogen synthesising experiments, ALPHA-2 and ALPHA-g. The availability of protons allow for new physics studies within ALPHA

to be considered, such as hydrogen formation, hydrogen trapping and then *in situ* hydrogen-antihydrogen comparisons. These topics will be elaborated upon later in the further scope.

The time-of-flight measurements presented in this thesis demonstrate an experimental sequence in which a positive ion population was purified into isolated protons, as shown in Section 5.5. A deconvolution algorithm and analysis were used to quantify the results, detailed in Sections 5.6.1 and 5.6.4, respectively. The initial positive ions, protons, H_2^+, and H_3^+, were produced by a heated electron plasma causing electron impact ionisation of the residual gas of the Penning trap, described in Section 4.1. In this study all measurements of the number of positive ions and their axially integrated radial distributions were destructive, reproducibility of positive ion production was crucial. Therefore, variations in the trap vacuum quality were monitored to ensure the integrity of the measurements, which was observed as changes in the number of positive ions generated versus the electron heating time. The positive ion species were identified by introducing positrons into the mixture, allowing relative information to be obtained when performing time-of-flight measurements, as shown in Section 4.6.

Previous ALPHA studies have successfully used an oscillating electric signal on a trap electrode to perform AR [98, 94], so it was decided that this method would be used to remove all species except protons. It was believed that the AR method would require an initially cold plasma to successfully couple the charged particles to a frequency chirp. However, the initial positive ions were produced by an energetic production mechanism (eV scale), resulting in an initial temperature of $(3.2\pm0.4)\times10^5$ K, see Section 4.2. Furthermore, the initial positive ions were radially sparse, as shown in Section 4.5. Positrons were transported into the Penning trap and mixed with the positive ions, causing the unexpected but useful behaviour of axialisation of positrons at high radii, which sympathetically compressed the sparse positive ion cloud. The Penning trap's 3 T solenoid cooled the positrons via cyclotron radiation, which also cooled the positive ions. The evolution of the positive ion temperature during the full experimental sequence is shown in Appendix D. The positive ion temperature appears to cool exponentially between capturing and removing positrons, likely because of the decaying cooling power of the positron cyclotron radiation. Using the rotating wall compression method, described in Section 2.2.1, the positron population was targeted for radial compression, sympathetically compressing positive ions. The positrons were removed with a short electric pulse, as described in Section 2.2.2.

The resulting positive ion mixture has a population size of $(3.0 - 3.8) \times 10^6$, a temperature of 1500 ± 100 K and a plasma radius of 1.6 mm.

Autoresonance was performed on the remaining cold positive ion plasma by connecting a waveform generator via a high-pass filter to one of the trap electrodes.

1	Load 1.3×10^8 electrons in the Catching Trap
2	Set electric potentials of the trap electrodes to nest the electrons within a positive ion potential well
3	Apply electron heating drive to generate positive ions
4	Wait until 2.4×10^6 positive ions are generated, and then turn off heating drive (Ideally, this duration should be calibrated on a daily basis)
5	Remove electrons
6	Set the trap electric potential to nest a positive ion potential well within the catching potentials of positrons
7	Transfer positrons into the Catching Trap
8	Change the trap electric potentials slowly to merge the positive ions and positrons over 12 s
9	Guide the mixed plasma towards the segmented electrode and set the trap electric potentials to the rotating wall compression potential well
10	Apply a 900 kHz 0.5 V_{pp} rotating wall compression for 10 s
11	Set trap electric potentials to axially narrow and deep potential well and hold for 10 s
12	Remove positrons
13	Guide the cold and compressed positive ion plasma to the autoresonance potential well (manipulations occur over 5.7 s, faster manipulations cause significant heating)
14	Apply frequency chirp to perform autoresonance and reduce well depth to eject driven particles

Table 6.1: Full experimental sequence for producing isolated protons

A systematic study determined the optimal configuration of a frequency chirp to autoresonantly drive nonproton particles. The amount of particles ejected stochastically from the trap was very inefficient. Therefore, the potential well depth of the trap was reduced to the initial level of the plasma space charge, determined from a temperature diagnostic measurement, described in Section 2.5.2. The sequence of steps for proton generation and isolation is listed in Table 6.1.

The ALPHA experiment captures 1.1×10^5 antiprotons every 140 seconds from the Antiproton Decelerator [102]. In comparison, this experimental sequence generates approximately $(0.9 - 1.2) \times 10^6$ protons in 61.3 seconds, not counting the time required for the generation of positive ions, which depends on current vacuum conditions, see Section 4.1 Figure 4.6 (b). During the second run, when the vacuum degradation reached a steady state, 2.4×10^6 positive ions were generated in approximately 12 seconds.

6.2 Further scope

Shortly after taking the last data for this study, the Catching Trap system underwent a significant upgrade in preparation for the new antiproton source, ELENA

[29], which delivers a reduced energy antiproton beam of 100 keV. In the ALPHA experiment, antiprotons are caught using a degrader foil specifically designed to optimise the resulting antiproton energy distribution. The Catching Trap can only trap axial energies up to 5 keV antiprotons. The upgrade involved a major mechanical redesign, as the new degrader, approximately 1 μm thick, cannot serve as a primary vacuum window between the vacuum of the ALPHA apparatus and ELENA, unlike the previous degrader. ELENA antiproton beamlines are expected to operate at around 10^{-10} mBar. The absence of a primary vacuum window led to a redesign of the Catching Trap vacuum system and cryopumping surfaces. Siara Fabbri's Ph.D. thesis [30] provides further details.

Since the study in this thesis was performed before the upgrade, some work is needed to re-establish the proton isolation method. First, feasibility experiments should be conducted to assess the current vacuum quality either by extending the duration of positive ion generation experiments or by studying the trap lifetime of antiprotons captured within the upgraded system. The operating vacuum pressure can be estimated using the antiproton lifetime.

Second, if the vacuum quality is not sufficient to generate a useful amount of positive ions, vacuum degradation should be considered. This could potentially be achieved by isolating the cryogenic Catching Trap vacuum from the rest of the ALPHA apparatus and turning off the Catching Trap vacuum pumps (turbo molecular pumps, as described in Section 4.1), along with closing a gate valve between the Catching Trap and the Extra Low Energy Antiproton ring (ELENA). However, this should be studied within a safe operating mode for the new degrader foil. Alternatively, if the Catching Trap cannot be degraded, another existing Penning trap within the ALPHA apparatus could be considered. It is unclear whether the positron accumulator can be adapted due to its distinct electrode stack geometry, described in Section 2.1.3.

If the vacuum quality in the Catching Trap is sufficiently poor to produce positive ions at a practical production rate, then the experimental sequences from the proton isolation study could be implemented within a few weeks. For reference, the second proton isolation study that produced the AR results shown in Chapter 5 was conducted within a month, including an entire week dedicated to degrading the vacuum quality.

This study relied on the availability of positrons from the positron accumulator to tailor and cool the positive ions, as described in Section 4.5. The positron source, detailed in Section 2.3.2, has a radioactive half-life of 950 days. As the source has not been replaced, its reduced radioactivity would require durations longer than 70 seconds to accumulate approximately $(3.0 - 3.5) \times 10^7$ positrons, as shown in the Appendix C. This extended duration would further increase the proton isolation sequence time. However, theoretically a four-fold improvement could be obtained

when positrons are transferred between the Atom Trap and the Catching Trap, as described in Section 4.3. This improvement would reduce the required positron accumulation times.

6.2.1 Optimisation of the proton source

Possible modifications to the experimental proton isolation sequences could be considered to simplify the process or increase the yield of isolated protons:

- Initial attempts to transfer positrons from the Positron Accumulator to the Catching Trap were unsuccessful. While Faraday cup measurements detected captured charged particles, no particles could be imaged on the MCP-phosphor diagnostic. This issue led to the abandonment of a direct transfer and the focus was on capturing positrons in ALPHA-2 before transferring them to the Catching Trap. During the early development of transferring positrons between the Atom Trap and the Catching Trap, an annular positron radial profile was imaged on the MCP-phosphor diagnostic. This issue was resolved by holding the captured positrons for several seconds, which is believed to be due to diocotron damping, discussed in Section 4.3. No attempt was made to perform a direct positron transfer from the Positron Accumulator to the Catching Trap with this additional hold time. This approach might lead to an increased positron transfer efficiency and simplify the experimental sequence by not involving the Atom Trap.

- In the first development run for proton isolation, the initial number of loaded positive ions was 1.2×10^7. The same electric potential manipulations were used as in the second development run. However, the plasma response to the AR frequency chirp and well depth cut was inconsistent. The well depth cut was calibrated by conducting the full experimental sequence until the AR chirp was applied. The well depth was then reduced and the remaining population was measured with a Faraday cup. This method was time-consuming and not calibrated daily.

  The second development run used two temperature diagnostic measurements, as described in Section 2.5.2. These measurements were performed daily, and the well depth cut was adjusted accordingly. A more consistent response to frequency chirp and well depth cut could be achieved with this calibration implemented for a positive ion population size of 1.2×10^7.

- Toward the end of the second development run's data collection, the experimental sequence was altered to exclude positrons. Instead, the sequence manipulated the initial hot positive ion population within the AR potential well,

applying a frequency chirp with the optimal chirp configuration and a potential well depth cut, reducing the potential well depth to 20 eV. Before the chirp signal, the ion temperature within the AR potential well was measured twice, resulting in temperatures of 6.05×10^4 K and 6.13×10^4 K. Comparison of time-of-flight measurements taken before and after the frequency chirp and potential well depth cut steps suggests that AR does occur. The outcome resembled the cooled and tailored positive ion plasma.

This experimental deviation took only one hour, offering promising prospects for future considerations. If successful, this approach could substantially simplify the entire experimental sequence, reducing its duration to approximately 10 seconds. Moreover, this simplification would allow for the generation of isolated protons using only a single cryogenic Penning trap, potentially increasing its appeal for applications beyond ALPHA. However, the hot isolated protons might alter their composition by reacting with residual gas or triggering further ionisation events, potentially introducing impurities.

6.2.2 Hydrogen formation studies

The work presented herein was primarily motivated by the aim of generating an isolated proton plasma to facilitate cold hydrogen production within the ALPHA-2 apparatus. The prospect of trapping and studying hydrogen using the same apparatus and experimental protocol as those employed for antihydrogen allows for a direct comparison, thereby bolstering the confidence of CPT tests.

The key developments necessary for the preparation of isolated protons for physics studies can be drawn from the experimental sequences of the ALPHA antiproton. Similar manipulations of protons can be achieved by simply reversing the polarity of the voltages applied to the electrode stack, assuming the proton population is identical in number to the antiprotons involved in the ALPHA sequences. Furthermore, the preparation of electrons, as opposed to positrons, is readily facilitated by the existing electron gun in the ALPHA-2.

Several critical steps must be taken in this process. First, the transport of proton plasma from the Catching Trap to the ALPHA-2 trap warrants a thorough study to minimise transfer losses. Following this, protons must be sympathetically cooled with a positron plasma and radially compressed to achieve parameters similar to the antiproton plasma [102].

The strong drive regime evaporative cooling method [37], used for the preparation of positrons, can be equivalently applied to prepare an electron plasma with parameters comparable to those of the positrons used for antihydrogen production. Optimising the parameters of the antimatter plasmas is crucial to enhance the production of cold antihydrogen, which requires increasing the overlap between both

species, decreasing the temperatures of both plasmas, and reducing their radial size to mitigate the influence of a radially increasing magnetic field generated by the octupole magnets of the neutral atom trap.

However, the formation of hydrogen cannot be verified by existing antihydrogen detectors, which rely on annihilation detection. This presents an initial challenge to confirm hydrogen production. One potential solution could be to ionise hydrogen and detect the resulting protons with one of the MCP detectors at the axial ends of the traps. To determine whether hydrogen formation can occur in the ALPHA-2 trap, the initial study does not require the production of cold and trappable hydrogen. A similar scheme to the one developed by the ATRAP group, which previously demonstrated the detection of antihydrogen formation by field ionisation within a Penning trap, could be adopted [103].

Antiproton-positron mixing produces antihydrogen atoms in a variety of electronic states, including high principal quantum number states (Rydberg states). The distribution of these states depends on the mixing conditions, such as temperature and plasma manipulation. The binding energy in the Rydberg states is significantly lower than that of the ground states, enabling ionisation with the electric fields achievable in the ALPHA-2 Penning traps.

Figure 6.1 illustrates an example electric field produced by the Atom Trap mixing region, suitable for on-axis field ionisation of high Rydberg state hydrogen. The electric field strength required to field ionise hydrogen from the Rydberg state can be estimated using the classical formula $F = 3.2 \times 10^8/n^4$ V/cm [104], where n is the principal quantum number of a Rydberg state. In the present configuration, the largest DC electric fields that can be produced by Penning trap electrodes within the ALPHA-2 Atom trap mixing region are on the order of 40 V/cm, as shown in Figure 6.1. In theory, this electric field strength could field-ionise Rydberg states of a principal quantum number greater than 53. However, in principle higher voltage power supplies can be used safely in this system to obtain larger electric field strengths.

Initial ALPHA antihydrogen experiments have produced a wide range of Rydberg states, although later production protocols have reduced the distribution of initial Rydberg states during formation to principal quantum numbers too low to be field ionised. However, by mixing positrons and protons at hotter temperatures, the initial Rydberg state distribution during formation could be modified to enhance larger Rydberg values.

When protons are dumped into the electrons, the proton momentum is directed in one way. A proton that does not capture an electron will be deflected by further electric fields, whereas a proton that does capture an electron becomes electrically neutral and can travel through the electric fields. As the hydrogen atom moves further, it travels through a large static electric field that can field-ionise the hy-
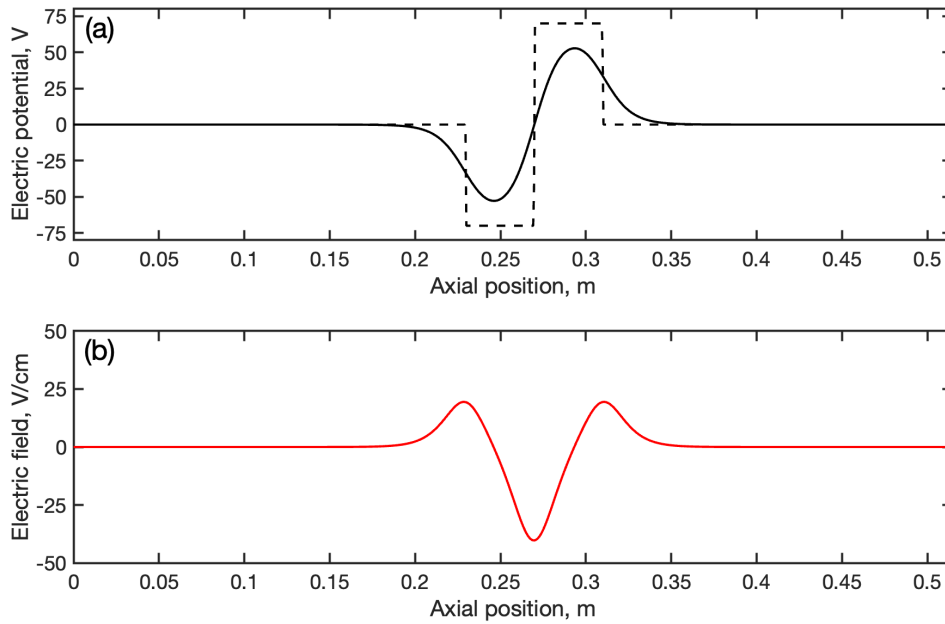
Figure 6.1: An example of an electric potential within the Atom Trap mixing region suitable for field ionisation of high Rydberg state hydrogen. (a) The solid black line is the on-axis electric potential and the dashed black line is the applied voltages on the electrodes. (b) The on-axis electric field corresponding to the same applied voltages as shown in (a).

drogen atom depending on its Rydberg state. Protons produced in the electric-field ionisation process are recaptured in the dedicated potential well, from which they can be ejected towards the MCP detector.

This method can also be used to determine the Rydberg state distribution of hydrogen by modifying the electric-field strength in the ionisation region. Although the field ionisation detection technique could confirm whether hydrogen can be formed in principle in the ALPHA-2 trap, this study would produce very few cold hydrogen atoms, making trapping rates impractical.

The formation of cold hydrogen for trapping, using a technique similar to ALPHA's antihydrogen production [102], will produce very few Rydberg states of high principal quantum number, making detection by electric field ionisation unsuitable. The trapped hydrogen atom will deexcite to its ground state, just as the trapped antihydrogen.

ALPHA studies detect trapped antihydrogen atoms by ejecting them from the neutral atom trap volume toward the inner apparatus walls. Charged pion products of antiproton annihilation are detected by external detectors surrounding the trap. This detection method is not possible with hydrogen.

During the ALPHA 1S-2S spectroscopy measurements, antihydrogen is photoionised by 243 nm laser light, and the product antiprotons escape outward, annihilating on apparatus surfaces. In order for protons to be detected, they would have to be di-

rected towards an internal detector, such as the MCP, installed on the central axis. The product protons of photoionised hydrogen would have to be recaptured using the Penning trap electric potentials and then ejected toward the MCP. Although ALPHA experiments have attempted to recapture antiprotons from photoionised products, these attempts have not been successful to date.

A detection method capable of detecting both hydrogen and antihydrogen could potentially rely on the detection of photons emitted by both atoms, for instance, fluorescence from the 2P-1S transition (121.6 nm). The integration of silicon photon multiplier chips for ultraviolet light detection within the Penning trap electrode stack is currently being investigated [105].

APPENDIX A

TIME-OF-FLIGHT ANALYSIS - ALL FITS AND MEASURES OF ERROR

Both figures A.1 and A.4 show the Gaussian curves and the Maxwell-Boltzmann time-of-flight curves fitted to the AR chirp start frequency scan. The amplitudes of the curves are shown as a heat map, where red indicates positive amplitudes and blue indicates negative amplitudes. The raw signal shown in (a) and the deconvolution signals are shown in (b), there is a clear reduction in negative amplitudes which are features introduced by the detector readout chain and seen as undershooting. The deconvolution relies upon the choice of guessing the real particle-current distribution, in this case a Gaussian distribution was chosen. Then three Gaussian curves were fitted to the deconvolved signal, as seen in (c). The residual errors between the Gaussian fits and the deconvolved signal are shown in (d); different colours are used to indicate positive and negative residuals due to the use of a different scale of amplitude values. The residuals oscillate between negative and positive values for start frequencies up to 1 MHz.
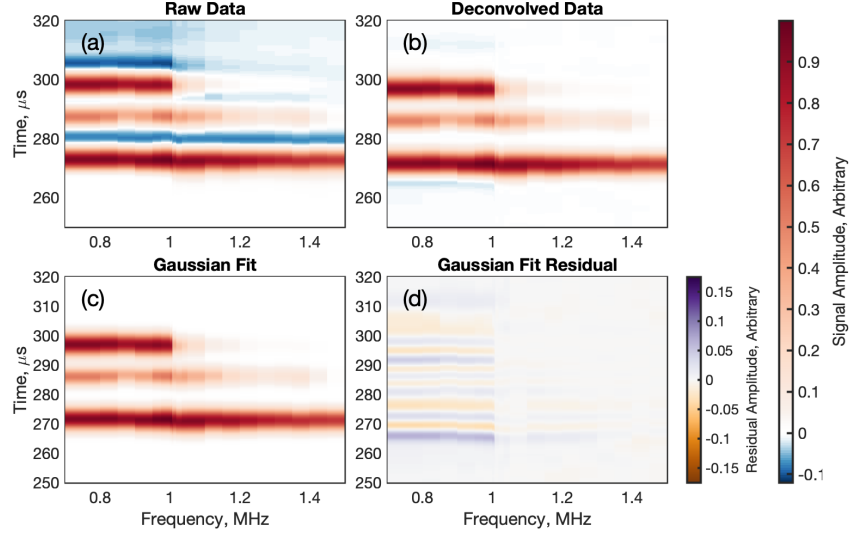
Figure A.1: The chirp start frequency scan measurements are shown above along with the corresponding analysis, which assumes a Gaussian particle-current distribution. The raw data amplitudes were normalised with respect to the maximal voltage from this scan's set of measurements. (a) The raw data shows red bands of particle-current and blue bands of negative valued signal. (b) The Gaussian deconvolved signals, which use a residual minimising chosen Gaussian signal shape. (c) Residual minimising Gaussian fits for each start frequency value. (d) The residual values of the Gaussian fit, coloured with an alternative (Purple-Orange) colour map.

Figure A.2: The chirp start frequency scan measurements are shown above along with the corresponding analysis, which assumes a Maxwell-Boltzmann time-of-flight distribution. The raw data amplitudes were normalised with respect to the maximal amplitude from this scan's set of measurements.(a) The raw data shows red bands of particle-current and blue bands of negative valued signal. (b) Maxwell-Boltzmann time-of-flight deconvolved fits. (c) Residual minimising Maxwell-Boltzmann time-of-flight fits for each chirp start frequency value. (d) The residual values of the Maxwell-Boltzmann time-of-flight fit, coloured with an alternative (Purple-Orange) colour map.
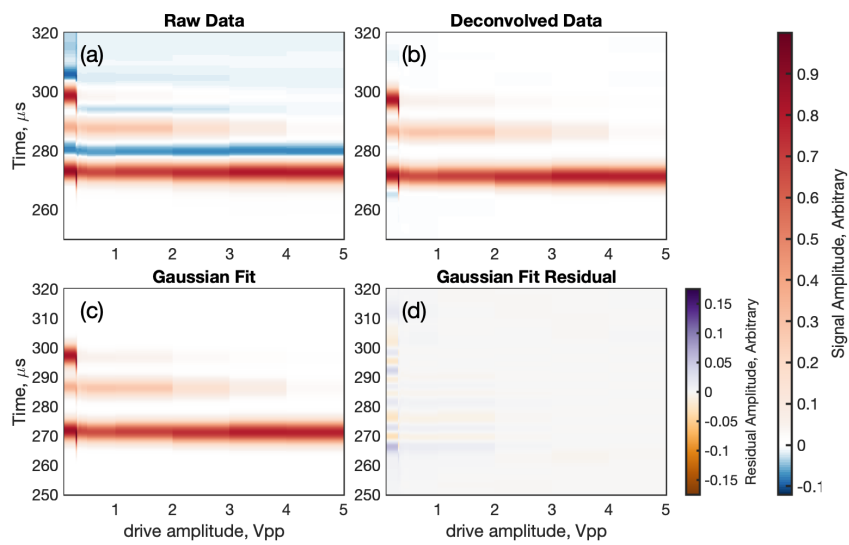
Figure A.3: The chirp amplitude scan measurements are shown above along with the corresponding analysis, which assumes a Gaussian particle-current distribution. The raw data amplitudes were normalised with respect to the maximal amplitude from this scan's set of measurements. (a) Raw data show red bands of the particle current and blue bands of negative valued signal. (b) Gaussian deconvolved signals, which use a residual minimising chosen Gaussian signal shape. (c) Residual minimising Gaussian fits for each start frequency value. (d) The residual values of the Gaussian fit, coloured with an alternative (Purple-Orange) colour map.
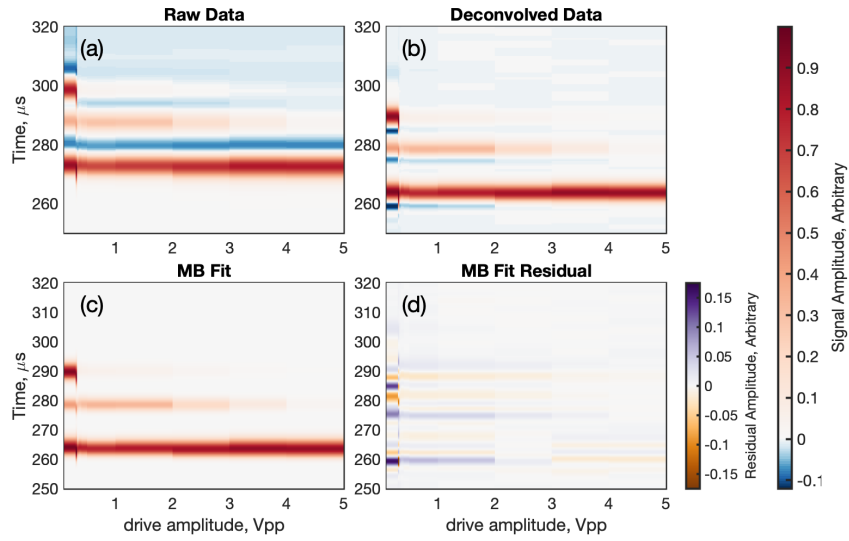
Figure A.4: The drive amplitude scan measurements are shown above along with the corresponding analysis, which assumes a Maxwell-Boltzmann time-of-flight distribution. The raw data amplitudes were normalised with respect to the maximal voltage from this scan's set of measurements.(a) The raw data shows red bands of particle-current and blue bands of negative valued signal. (b) Maxwell-Boltzmann time-of-flight deconvolved signals, which use a residual minimising the chosen Maxwell-Boltzmann time-of-flight signal shape. (c) Residual minimising Maxwell-Boltzmann time-of-flight fits for each drive amplitude value. (d) The residual values of the Maxwell-Boltzmann time-of-flight fit, coloured with an alternative (Purple-Orange) colour map.
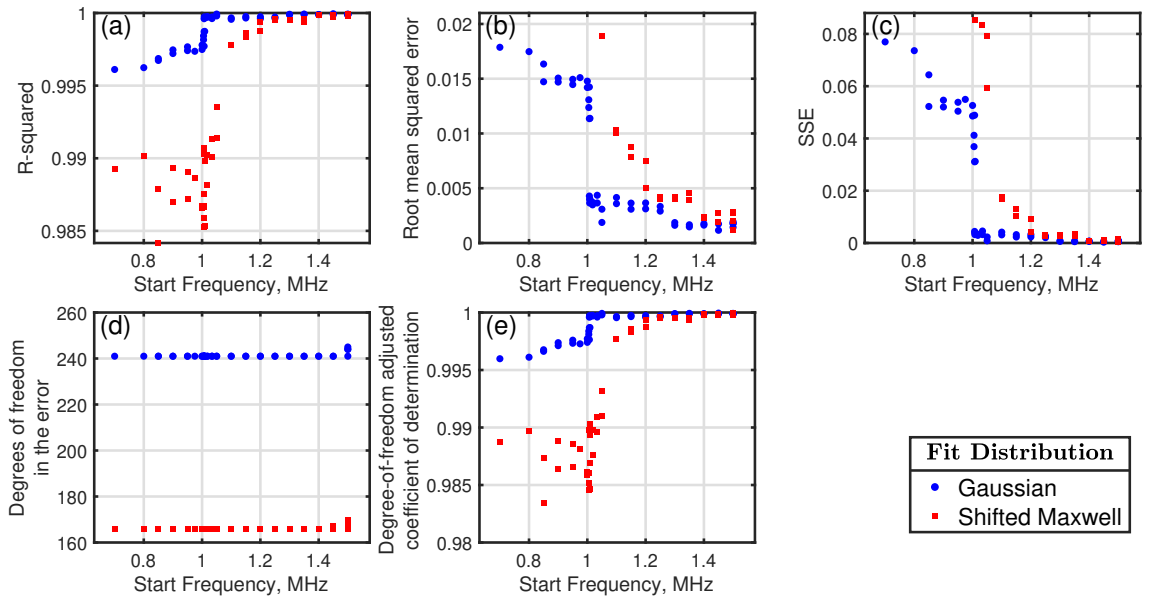
Figure A.5: Various measures of the Gaussian fit error, shown as blue dots, and Maxwell-Boltzmann time-of-flight fit error, shown as red squares, from the start frequency scan. (a) The R^2, the coefficient of determination. (b) The root mean squared error. (c) The sum of squares due to error. (d) The degrees of freedom in the error. (e) The degree of freedom adjusted coefficient of determination.
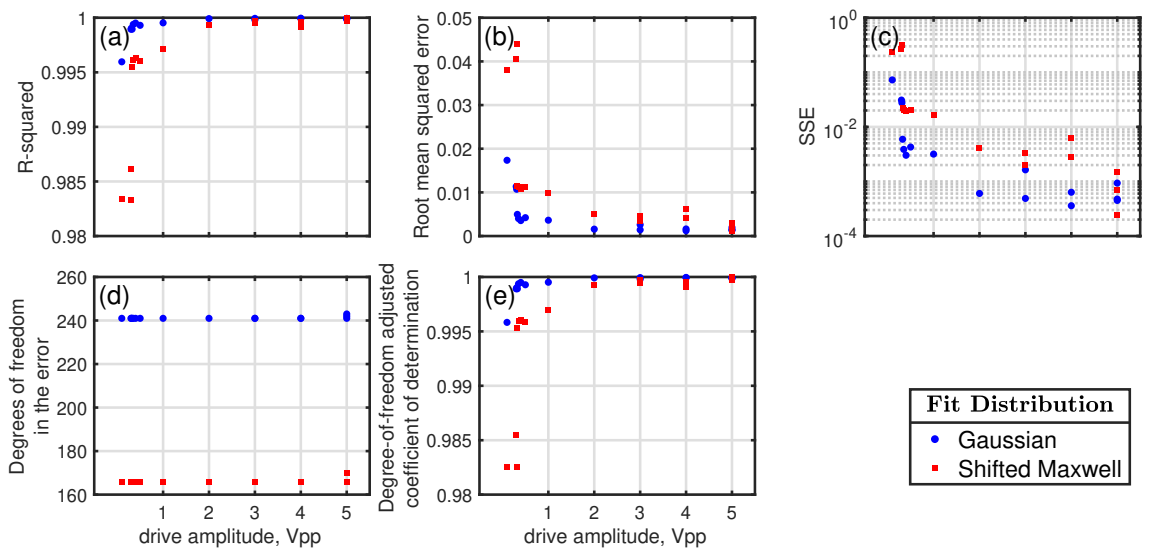
Figure A.6: Various measures of the Gaussian fit error, shown as blue dots, and Maxwell-Boltzmann time-of-flight fit error, shown as red squares, from the drive amplitude scan. (a) The R^2, the coefficient of determination. (b) The root mean squared error. (c) The sum of squares due to error. (d) The degrees of freedom in the error. (e) The degree of freedom adjusted coefficient of determination.

TWO COMPONENT AXIALLY INTEGRATED RADIAL PROFILE FIT

In the ALPHA group, axially integrated radial profiles are analysed using the Gaussian power curve given by:

$$N\left(\rho\right) = a \exp\left(-\left[\frac{\rho}{b}\right]^{n}\right),$$ (B.1)

where ρ is the radial position, b is the plasma radius, a is the plasma peak value, and n is the Gaussian power. This fit is empirically justified. It can be further extended to the context of a two-component plasma with a single sign charge. The ratio of the radial density distribution of two individual components is given by Equation 28 from Chapter 11 of Trapped Charged Particles by M. Knoop, N. Madsen, and R. C. Thompson. This equation assumes thermal equilibrium and is expressed as:

$$,\frac{N_B\left(\rho\right)}{N_A\left(\rho\right)} = C_{BA} \exp\left(\frac{1}{2\,k_B\,T}\left[M_B - M_A\right]\omega_\rho\rho^2\right)$$ (B.2)

$$= C_{BA} \exp\left(\left[\frac{c\rho}{b}\right]^2\right).$$ (B.3)

In this context, the distribution of the radial density of the heavier component 'B', with mass M_B, is denoted $N_B\left(\rho\right)$ and the lighter component 'A', with mass M_A, is denoted $N_A\left(\rho\right)$. Additionally, the constant C_{BA} is related to the fractional amount of each of the two species. T is the equilibrium temperature and ω_ρ is the bulk rotation frequency around the axisymmetric axis of the Penning trap. These plasma constants are not determined and instead are merged into the quotient of fit parameters c and b, where b is the same length-scale parameter as in the Gaussian power curve.

Since Equation B.1 has been found to be appropriate for a single-component plasma, it is chosen to be used with the primary (centre) component. Rearranging Equation

B.3 and substituting Equation B.1 for N_A, we obtain a massive Gaussian power curve:

$$N_B \left(\rho \right) = N_A \left(\rho \right) C_{BA} \exp \left(\left[\frac{c\rho}{b} \right]^2 \right) \tag{B.4}$$

$$= a' \exp \left(- \left[\frac{\rho}{b} \right]^n \right) C_{BA} \exp \left(\left[\frac{c\rho}{b} \right]^2 \right) \tag{B.5}$$

$$= a' C_{BA} \exp \left(- \left[\frac{\rho}{b} \right]^n + \left[\frac{c\rho}{b} \right]^2 \right) \tag{B.6}$$

$$N_B \left(\rho \right) = a \exp \left(- \left[\frac{\rho}{b} \right]^n + \left[\frac{c\rho}{b} \right]^2 \right). \tag{B.7}$$

Experiments performed by ALPHA feature a two-component plasma, the electron-antiproton plasma, which has been observed to centrifugally separate in a high-strength magnetic field Penning trap [106]. Typically, two-component plasmas' radial profiles are usually compared to simulations, the proposed massive Gaussian power curve provides a measurable parameterisation for both components. This enables the quantification of the degree of centrifugal separation independent of simulations.

Figure B.1 presents example measurements of electron-antiproton plasmas using the extended fitting curve, demonstrating its suitability for this context. The centre column displays the radial distributions of the antiproton component of the plasma. As shown, the antiproton component exhibits increased centrifugal separation down the rows, a phenomenon captured by the increasing values of the c parameter.

A relevant parameter is the plasma radius, typically defined as the radial distance from the plasma centre where the intensity decreases by a factor of $\exp(-1)$. For the Gaussian power curve, this value is simply represented by the parameter b. The maximum value of the massive Gaussian power curve can occur at any radial point, necessitating an extended definition of the plasma radius. In this case, it represents the farthest radial position where the value has decreased by a factor of $\exp(-1)$ from the maximum value.
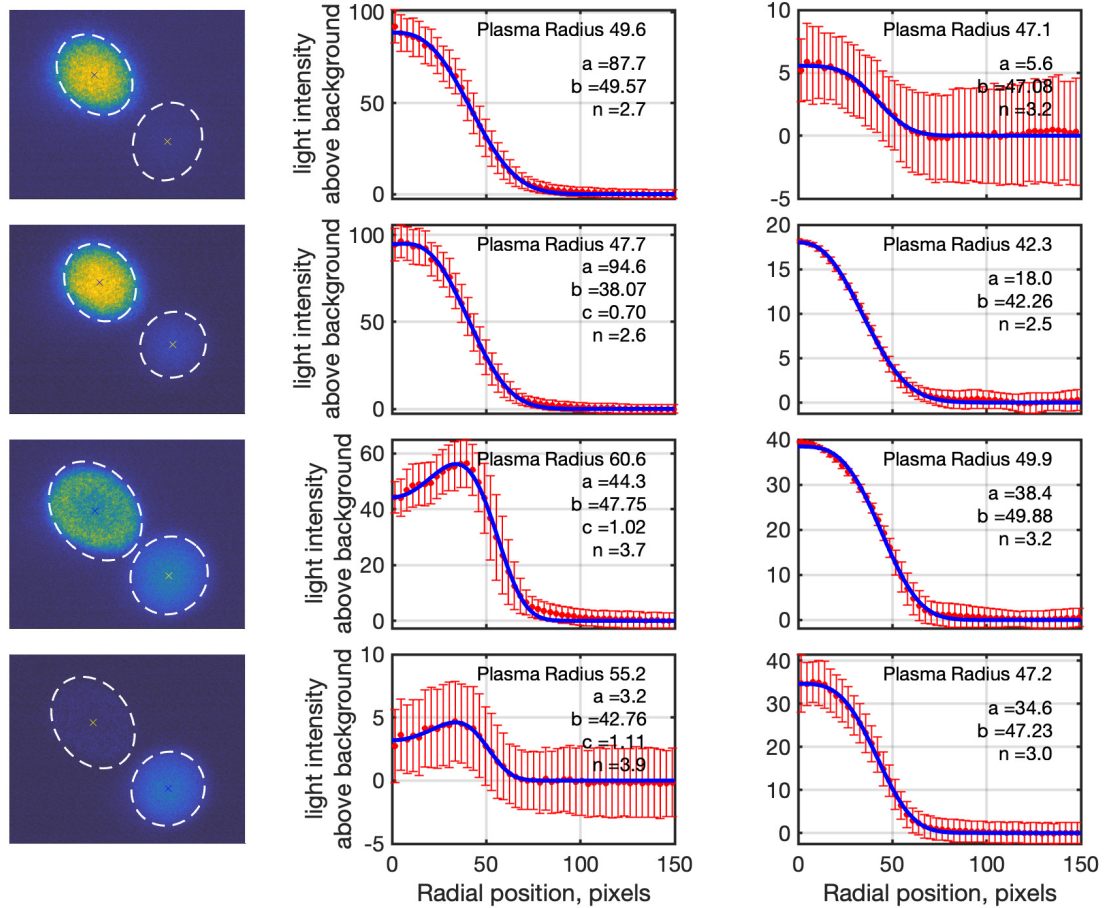
Figure B.1: The left column displays MCP images of electron-antiproton plasma, with identified components indicated by white dashed ellipses. The centre and right columns show the average MCP light intensity radially outward for each identified plasma component as red dots, whereas the statistical standard deviations are represented by red bars. The blue line corresponds to a fitted massive Gaussian power curve.

POSITIVE ION RUN 2 - DAILY BASELINE MEASUREMENTS OF POSITRON ACCUMULATION

During the positive ion study, it was crucial to monitor the number of accumulated positrons over fixed time intervals, as this information indicated when a new neon moderator of the positron source needed to be regrown and whether any instabilities in the measurements required further inspection of the accumulator hardware. Figure C.1 shows the baseline measurements from the second run of the positive ion study for fixed accumulation times of 50 s and 70 s.

The timeline can be divided into three periods. The earliest period exhibits significant instability in the 70 s accumulation baseline, which was caused by a burnt-out resistor on a high-pass filter connected to a segment of the segmented electrode. During the 2nd of September 2020, the resistor was fixed and a new neon moderator was grown, leading to a much more consistent baseline.
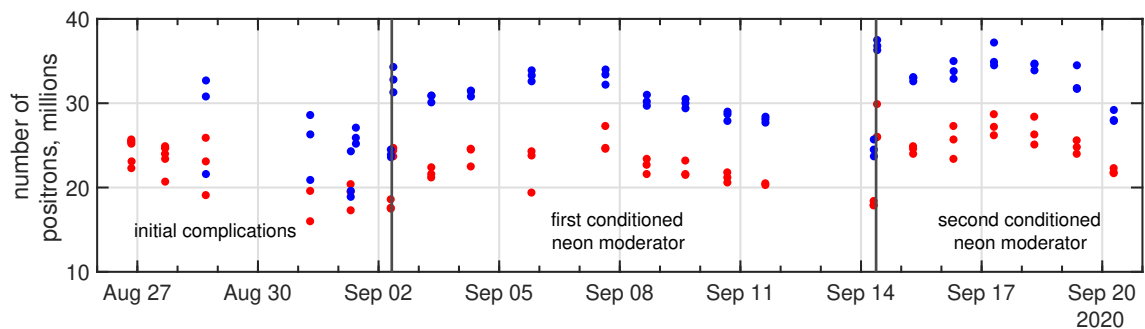
Figure C.1: The daily baseline of positron accumulation, this measurement has a fixed accumulation time followed by ejecting the positrons to the Catching Trap degrader foil, which serves as a Faraday cup. Red dots and blue dots correspond to fixed accumulation times of 50 s and 70 s, respectively.

POSITIVE ION TEMPERATURE FULL SEQUENCE

The temperature of positive ions can influence the generation of additional positive ions, which motivated efforts to minimise the temperature. Figure D.1 shows the temperature at key points during the optimised full sequence.
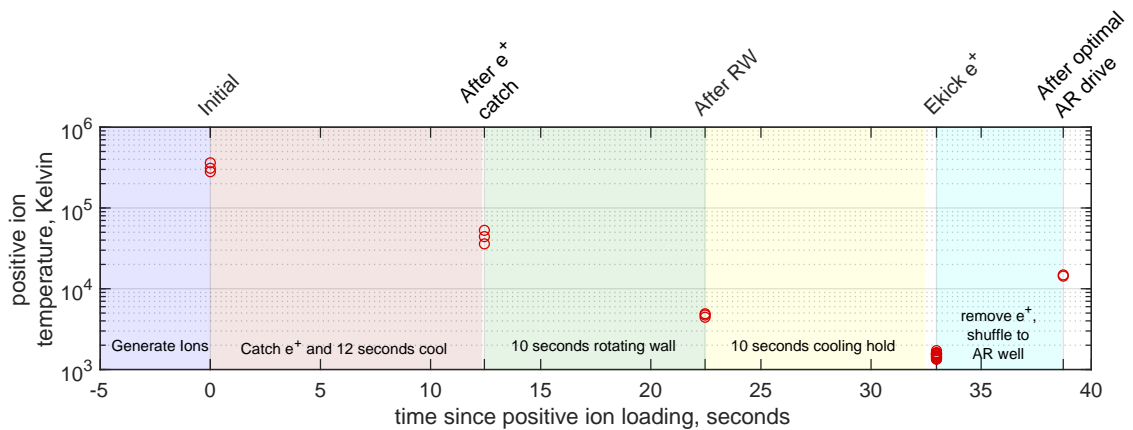
Figure D.1: Positive ion temperature at key points within the full proton generation sequence.

APPENDIX E

POSITIVE ION TOY MODEL AXIAL FREQUENCY PREDICTIONS

The axial frequencies of positive ions within the Catching Trap AR well, as shown in Figure 5.1, were calculated after performing the experiment to improve the interpretation of the results. These calculations are somewhat basic, as they only consider the motion of single particles along the axial degree for specific radial positions, disregarding radial motion. The trapping electric potentials were computed for a mesh of positions using COMSOL software, with an axial resolution of 12 μm and a radial resolution of 7 μm.

The natural cubic spline method, where the second derivatives of the spline polynomials are set to zero at the endpoints of the interpolation interval, was employed to interpolate the electric potential at nonmesh points, as it enforces smoothness. The electric potential due to the space charge was determined using a closed Poisson solver. In this process, an initial particle density distribution is estimated, the space charge electric potential is calculated, and then a new particle density distribution is computed. This new distribution must have an axially integrated radial profile that aligns with the measured MCP images. The last two steps are iterated until the particle density distribution converges.

The absence of centrifugal separation in MCP images of the positive ion mixture suggests that the thermal energy is greater than the outward centrifugal forces of the rotating plasma. This observation has been used to justify neglecting terms with an order higher than the first in the plasma rotational frequency. Consequently, the force balancing equation can be reduced to one that describes a single component plasma, simplifying the analysis.

Convergence was considered achieved when the total integrated difference between successive particle distributions was less than 1%. To reach convergence, the spacing of the interpolated position mesh needed to be smaller than the Debye length scale,

which increased the computational time for colder input temperatures. To overcome this, an initial hot converged particle density distribution was calculated and used as the initial guess distribution for a slightly colder input value. This process was repeated iteratively, fractionally lowering the temperature at each step until the desired cold temperature solution was obtained.

A single particle axial frequency, ω_{axial}, at a fixed radial position can be determined knowing both the axial path travelled by the particle for a specific total energy, K_{max}, and the particle velocity at each position along the path. The time period of motion can be determined from the closed axial integral of the reciprocal velocity of the particle. This can be expressed in terms of energy as follows:

$$\frac{2\pi}{\omega_{\text{axial}}(K_{\text{max}})} = \oint \sqrt{\frac{m}{2K(z, K_{\text{max}})}} \mathrm{d}z, \qquad (E.1)$$

where K is the particle kinetic energy dependent on the axial position and K_{max} denotes the total particle energy. For a specific trapping electric potential, $\phi(z)$, K_{max} parameterises the axial path of the particle, defining the maximum extent to which the particle can travel along either direction of the axis. The stored energy of the electric potential $q\bar{\phi}(z) = q\phi(z) - q\phi_{\text{min}}$ represents the electric potential relative to the minimum electric potential accessible within the path of the trapped particle. Consequently, the particle kinetic energy can be expressed as a function of both the total particle energy and the axial position-dependent electric potential:

$$K(z, K_{\text{max}}) = K_{\text{max}} - q\bar{\phi}(z). \qquad (E.2)$$

The integral was calculated by finding the turning points of the particles for a specific total particle energy K_{max}, integrating between the two axial positions and multiplying by a factor of 2 to account for the closed path. The axial frequency to total particle energy curves were calculated for both the vacuum electric potential of the AR well electrode configuration and the space charge included electric potential obtained using the previously described closed Poisson solver. These curves are shown in Figure 5.2.

The calculations were performed for two radial positions: the on-axis (electrode centre) and off-axis at 1.6 mm, which represents the plasma radius used when calculating the space charge contribution to the electric potential. These radial positions are meant to approximate the range of axial frequencies experienced by the trapped particles.

The electrode-only electric potentials are determined by the known trap geometry, but the prepared positive ion mixture can vary in the number of positive ions and its temperature. As a result, the particle density distributions were calculated for various combinations of lower and upper experimental error bounds, taken from Ta-

thermal average 1500 ± 100 K	electrodes + space charge		electrodes only	
species	on-axis (MHz)	plasma radius (MHz)	on-axis (MHz)	plasma radius (MHz)
proton	0.3643 - 0.4340	0.7251 - 0.8515	1.723	1.744
H2+	0.2575 - 0.3068	0.5126 - 0.6019	1.218	1.233
H3+	0.2104 - 0.2506	0.4188 - 0.4918	0.9952	1.007

Table E.1: Temperature averaged axial frequencies of the three hydrogen ion species within the Catching Trap AR well.

zero energy	electrodes + space charge		electrodes only	
species	on-axis (MHz)	plasma radius (MHz)	on-axis (MHz)	plasma radius (MHz)
proton	0.2580 - 0.3280	0.6483 - 0.7848	1.724	1.745
H2+	0.1823 - 0.2319	0.4583 - 0.5547	1.218	1.233
H3+	0.1490 - 0.1895	0.3744 - 0.4532	0.9954	1.008

Table E.2: Linearly interpolated zero energy axial frequencies of the three hydrogen ion species within the Catching Trap AR well.

Max Frequency	electrodes + space charge	
species	on-axis	plasma radius
proton	1.536 - 1.556 MHz [10.27 - 10.38 eV]	1.585 - 1.604 MHz [8.963 - 9.037 eV]
H2+	1.086 - 1.100 MHz [10.27 - 10.38 eV]	1.121 - 1.134 MHz [8.963 - 9.037 eV]
H3+	0.8870 - 0.8988 MHz [10.27 - 10.38 eV]	0.9155 - 0.9261 MHz [8.963 - 9.037 eV]

Table E.3: Maximum axial frequencies of the three hydrogen ion species within the Catching Trap AR well. Square brackets indicate the respective axial energies.

ble 4.2, and their corresponding space charge electric fields were used to constrain the range of calculated axial frequencies.

Refer to tables E.1 to E.3 for notable values extracted from the curves shown in Figure 5.2. The axial frequency is scaled by the square root of the particle mass, as seen in Equation E.1. Therefore, the axial frequency to axial energy curves can be scaled to any species of interest, such as the three lightest hydrogen positive ions.

BIBLIOGRAPHY

[1] P. A. M. Dirac. "The quantum theory of the electron". *Proceedings of the Royal Society of London. Series A, Containing Papers of a Mathematical and Physical Character* 117.778 (Feb. 1928), pp. 610–624. DOI: 10.1098/rspa.1928.0023.

[2] J. R. Oppenheimer. "On the Theory of Electrons and Protons". *Physical Review* 35.5 (Mar. 1, 1930), pp. 562–563. DOI: 10.1103/PhysRev.35.562.

[3] P. A. M. Dirac. "Quantised singularities in the electromagnetic field," *Proceedings of the Royal Society of London. Series A, Containing Papers of a Mathematical and Physical Character* 133.821 (Sept. 1931), pp. 60–72. DOI: 10.1098/rspa.1931.0130.

[4] C. D. Anderson. "The Apparent Existence of Easily Deflectable Positives". *Science* 76.1967 (Sept. 9, 1932), pp. 238–239. DOI: 10.1126/science.76.1967.238.

[5] O. Chamberlain *et al.* "Observation of Antiprotons". *Physical Review* 100.3 (Nov. 1, 1955), pp. 947–950. DOI: 10.1103/PhysRev.100.947.

[6] G. Baur *et al.* "Production of antihydrogen". *Physics Letters B* 368.3 (Feb. 1996), pp. 251–258. DOI: 10.1016/0370-2693(96)00005-6.

[7] G. Blanford *et al.* "Observation of Atomic Antihydrogen". *Physical Review Letters* 80.14 (Apr. 6, 1998). Publisher: American Physical Society, pp. 3037–3040. DOI: 10.1103/PhysRevLett.80.3037.

[8] G. Lemaître. "Un Univers homogène de masse constante et de rayon croissant rendant compte de la vitesse radiale des nébuleuses extra-galactiques". *Annales de la Société Scientifique de Bruxelles* 47 (Jan. 1, 1927), pp. 49–59.

132

[9] E. Hubble. "A relation between distance and radial velocity among extragalactic nebulae | Proceedings of the National Academy of Sciences". *Proceedings of the national academy of sciences* 15.3 (Apr. 25, 1929), pp. 168–173.

[10] M. Aguilar *et al.* "The Alpha Magnetic Spectrometer (AMS) on the international space station: Part II — Results from the first seven years". *Physics Reports.* The Alpha Magnetic Spectrometer (AMS) on the International Space Station: Part II - Results from the First Seven Years 894 (Feb. 7, 2021), pp. 1–116. DOI: 10.1016/j.physrep.2020.09.003.

[11] T. D. Lee and C. N. Yang. "Question of Parity Conservation in Weak Interactions". *Physical Review* 104.1 (Oct. 1, 1956), pp. 254–258. DOI: 10.1103/PhysRev.104.254.

[12] C. S. Wu *et al.* "Experimental test of parity conservation in beta decay". *Physical Review* 105.4 (Feb. 15, 1957). Publisher: American Physical Society, pp. 1413–1415. DOI: 10.1103/PhysRev.105.1413.

[13] D. Colladay and V. A. Kostelecký. "Lorentz-violating extension of the standard model". *Physical Review D* 58.11 (Oct. 26, 1998). Publisher: American Physical Society, p. 116002. DOI: 10.1103/PhysRevD.58.116002.

[14] M. Charlton, S. Eriksson, and G. M. Shore. *Antihydrogen and fundamental physics.* Springer, 2020. 101 pp.

[15] W. M. Fairbank and F. C. Witteborn. "Experiments to measure the force of gravity on positrons". *Proc. 23 Rencontre de Moriond; 5th Force Neutrino Physics.* 1988, pp. 617–622.

[16] M. Holzscheiter. "Free Fall Experiments with Charged Particles - A historical journey". 3rd International Workshop on Antimatter and Gravity. University College London, United Kingdom, Aug. 5, 2015.

[17] G. Testera *et al.* "The AEgIS experiment". *Hyperfine Interactions* 233.1 (Aug. 1, 2015), pp. 13–20. DOI: 10.1007/s10751-015-1165-5.

[18] P. Pérez *et al.* "The GBAR antimatter gravity experiment". *Hyperfine Interactions* 233.1 (Aug. 1, 2015), pp. 21–27. DOI: 10.1007/s10751-015-1154-8.

[19] A. E. Charman. "Description and first application of a new technique to measure the gravitational mass of antihydrogen". *Nature Communications* 4.1 (Apr. 30, 2013). Publisher: Nature Publishing Group, p. 1785. DOI: 10.1038/ncomms2787.

[20] R. J. Hughes and M. H. Holzscheiter. "Constraints on the gravitational properties of antiprotons and positrons from cyclotron-frequency measurements". *Physical Review Letters* 66.7 (Feb. 18, 1991). Publisher: American Physical Society, pp. 854–857. DOI: 10.1103/PhysRevLett.66.854.

[21] M. J. Borchert *et al.* "A 16-parts-per-trillion measurement of the antiproton-to-proton charge–mass ratio". *Nature* 601.7891 (Jan. 6, 2022), pp. 53–57. DOI: 10.1038/s41586-021-04203-w.

[22] S Baird *et al.* "The Antiproton Decelerator: AD". *Nuclear Instruments and Methods in Physics Research Section A: Accelerators, Spectrometers, Detectors and Associated Equipment.* Proceedings of the Eleventh International Advanced ICFA Beam Dynamic Workshop on Beam Cooling and Instability Damping Dedicated to the 30th Anniversary of Electron Cooling on board a ship from Moscow to Nizhny Novgorod 391.1 (May 21, 1997), pp. 210–215. DOI: 10.1016/S0168-9002(97)00359-8.

[23] D. Möhl. "Production of low-energy antiprotons". *Hyperfine Interactions* 109.1 (Aug. 1, 1997), pp. 33–41. DOI: 10.1023/A:1012680728257.

[24] J. Y. Hémery and S. Maury. "The Antiproton Decelerator: Overview". *Nuclear Physics A.* Proceedings of the Fifth Biennial Conference on Low-Energy Antiproton Physics 655.1 (Aug. 9, 1999), pp. c345–c352. DOI: 10.1016/S0375-9474(99)00223-7.

[25] C. Smorra *et al.* "BASE – The Baryon Antibaryon Symmetry Experiment". *The European Physical Journal Special Topics* 224.16 (Nov. 1, 2015), pp. 3055–3108. DOI: 10.1140/epjst/e2015-02607-4.

[26] A. Kellerbauer *et al.* "Proposed antimatter gravity measurement with an antihydrogen beam". *Nuclear Instruments and Methods in Physics Research Section B: Beam Interactions with Materials and Atoms.* Low Energy Positron and Positronium Physics 266.3 (Feb. 1, 2008), pp. 351–356. DOI: 10.1016/j.nimb.2007.12.010.

[27] C. Malbrunot *et al.* "The ASACUSA antihydrogen and hydrogen program: results and prospects". *Philosophical Transactions of the Royal Society A: Mathematical, Physical and Engineering Sciences* 376.2116 (Mar. 28, 2018). Publisher: Royal Society, p. 20170273. DOI: 10.1098/rsta.2017.0273.

[28] R. S. Hayano *et al.* "Antiprotonic helium and CPT invariance". *Reports on Progress in Physics* 70.12 (Nov. 2007). Publisher: IOP Publishing, pp. 1995–2065. DOI: 10.1088/0034-4885/70/12/R01.

[29] Wolfgang Bartmann *et al.* "The ELENA facility". *Philosophical Transactions of the Royal Society A: Mathematical, Physical and Engineering Sciences* 376.2116 (Mar. 28, 2018). Publisher: Royal Society, p. 20170266. DOI: 10.1098/rsta.2017.0266.

[30] S. Fabbri. "Optimization of Antiproton Capture and Delivery for the ALPHA Antihydrogen Experiment". PhD thesis. The University of Manchester, 2021.

[31] C. G. Parthey *et al.* "Improved Measurement of the Hydrogen 1S-2S Transition Frequency". *Physical Review Letters* 107.20 (Nov. 11, 2011). Publisher: American Physical Society, p. 203001. DOI: 10.1103/PhysRevLett.107.203001.

[32] M. Ahmadi *et al.* "Characterization of the 1S–2S transition in antihydrogen". *Nature* 557.7703 (May 2018). Number: 7703 Publisher: Nature Publishing Group, pp. 71–75. DOI: 10.1038/s41586-018-0017-2.

[33] M. Ahmadi *et al.* "Observation of the hyperfine spectrum of antihydrogen". *Nature* 548.7665 (Aug. 2017). Number: 7665 Publisher: Nature Publishing Group, pp. 66–69. DOI: 10.1038/nature23446.

[34] M. Ahmadi *et al.* "Investigation of the fine structure of antihydrogen". *Nature* 578.7795 (Feb. 2020). Number: 7795 Publisher: Nature Publishing Group, pp. 375–380. DOI: 10.1038/s41586-020-2006-5.

[35] C. J. Baker *et al.* "Laser cooling of antihydrogen atoms". *Nature* 592.7852 (Apr. 2021). Number: 7852 Publisher: Nature Publishing Group, pp. 35–42. DOI: 10.1038/s41586-021-03289-6.

[36] J. Jones. "Sympathetically Laser-Cooled Positron Plasmas for Antihydrogen Formation". PhD thesis. Swansea: Swansea University, Jan. 1, 2022. DOI: 10.23889/SUthesis.59731.

[37] M. Ahmadi *et al.* "Enhanced Control and Reproducibility of Non-Neutral Plasmas". *Physical Review Letters* 120.2 (Jan. 8, 2018). Publisher: American Physical Society, p. 025001. DOI: 10.1103/PhysRevLett.120.025001.

[38] E. D. Hunter *et al.* "Electron cyclotron resonance (ECR) magnetometry with a plasma reservoir". *Physics of Plasmas* 27.3 (Mar. 2020), p. 032106. DOI: 10.1063/1.5141999.

[39] A. Weiser. "A low energy proton source for ASACUSA's matter studies". Master Thesis. Austrian Academy of Sciences, 2020.

[40] C. Amole *et al.* "The ALPHA antihydrogen trapping apparatus". *Nuclear Instruments and Methods in Physics Research, Section A: Accelerators, Spectrometers, Detectors and Associated Equipment* 735 (Jan. 21, 2014). Publisher: North-Holland, pp. 319–340. DOI: 10.1016/j.nima.2013.09.043.

[41] R. G. Greaves and C. M. Surko. "Solid neon moderator for positron-trapping experiments". *Canadian Journal of Physics* 74.7 (July 1996). Publisher: NRC Research Press, pp. 445–448. DOI: `10.1139/p96-063`.

[42] D. P van der Werf *et al.* "The ATHENA positron accumulator". *Applied Surface Science.* 9th International Workshop on Slow Positron Beam Techniques for Solids and Surfaces 194.1 (June 21, 2002), pp. 312–316. DOI: `10.1016/S0169-4332(02)00141-1`.

[43] S. Gov, S. Shtrikman, and H. Thomas. "Magnetic trapping of neutral particles: Classical and quantum-mechanical study of a Ioffe-Pritchard type trap". *Journal of Applied Physics* 87.8 (Apr. 15, 2000). Publisher: American Institute of Physics Inc., pp. 3989–3998. DOI: `10.1063/1.372444`. arXiv: `quant-ph/9907044`.

[44] M. Ahmadi *et al.* "Observation of the hyperfine spectrum of antihydrogen". *Nature* 548.7665 (Aug. 2017). Number: 7665 Publisher: Nature Publishing Group, pp. 66–69. DOI: `10.1038/nature23446`.

[45] M. Johnson. "Design and Commissioning of Beamlines for the ALPHA Antihydrogen Experiment". PhD thesis. The University of Manchester, 2019.

[46] C. Amole *et al.* "The ALPHA antihydrogen trapping apparatus". *Nuclear Instruments and Methods in Physics Research Section A: Accelerators, Spectrometers, Detectors and Associated Equipment* 735 (Jan. 21, 2014), pp. 319–340. DOI: `10.1016/j.nima.2013.09.043`.

[47] R. C. Thompson, N. Madsen, and M. Knoop. *Trapped charged particles : a graduate textbook with problems and solutions.* WSPC (Europe), 2016.

[48] M. E. Glinsky *et al.* "Collisional equipartition rate for a magnetized pure electron plasma". *Physics of Fluids B* 4.5 (May 4, 1992). Publisher: American Institute of PhysicsAIP, pp. 1156–1166. DOI: `10.1063/1.860124`.

[49] X. P. Huang *et al.* "Steady-State confinement of non-neutral plasmas by rotating electric fields". *Physical Review Letters* 78.5 (Feb. 3, 1997). Publisher: American Physical Society, pp. 875–879. DOI: `10.1103/PhysRevLett.78.875`.

[50] T. D. MacMahon and A. P. Baerg. "The electron capture to positron branching ratio in the decay of ^{22}Na". *Canadian Journal of Physics* 54.14 (July 15, 1976). Publisher: Canadian Science Publishing, pp. 1433–1437. DOI: `10.1139/p76-168`.

[51] A. P. Baerg. "Electron capture to positron branching ratios in the decay of ^{22}Na and ^{44}Sc." *Canadian journal of physics* 61.8 (1983). Publisher: NRC Research Press Ottawa, Canada, pp. 1222–1226. DOI: `10.1139/p83-155`.

[52] H. Houtermans, O. Milosevic, and F. Reichel. "Half-lives of 35 radionuclides". *The International Journal Of Applied Radiation And Isotopes* 31.3 (Mar. 1, 1980). Publisher: Pergamon, pp. 153–154. DOI: `10.1016/0020-708X(80) 90139-8`.

[53] G. Z. Li *et al.* "Adiabatic cooling of antiprotons in a Penning trap". *Hyperfine Interactions* 76.1 (Dec. 1993). Publisher: Baltzer Science Publishers, Baarn/Kluwer Academic Publishers, pp. 281–284. DOI: `10.1007/BF02316725`.

[54] G. Savard *et al.* "A new cooling technique for heavy ions in a Penning trap". *Physics Letters A* 158.5 (Sept. 2, 1991), pp. 247–252. DOI: `10.1016/0375- 9601(91)91008-2`.

[55] H. F. Powell, D. M. Segal, and R. C. Thompson. "Axialization of Laser Cooled Magnesium Ions in a Penning Trap". *Physical Review Letters* 89.9 (Aug. 12, 2002). Publisher: American Physical Society, p. 093003. DOI: `10. 1103/PhysRevLett.89.093003`.

[56] D. L. Eggleston *et al.* "Parallel energy analyzer for pure electron plasma devices". *Physics of Fluids B* 4.10 (Oct. 4, 1992). Publisher: American Institute of PhysicsAIP, pp. 3432–3439. DOI: `10.1063/1.860399`.

[57] E. D. Hunter *et al.* "Plasma temperature measurement with a silicon photomultiplier (SiPM)". *Review of Scientific Instruments* 91.10 (Oct. 1, 2020). Publisher: American Institute of Physics Inc., p. 103502. DOI: `10.1063/5. 0006672`. arXiv: `2002.11216`.

[58] S. Sellner *et al.* "Improved limit on the directly measured antiproton lifetime". *New Journal of Physics* 19.8 (Aug. 31, 2017). Publisher: Institute of Physics Publishing, p. 083023. DOI: `10.1088/1367-2630/aa7e73`.

[59] X. Fei. "Trapping Low-Energy Antiprotons in an Ion Trap". PhD thesis. Harvard University, 1990.

[60] S. A. Jones. "Observation of the 1S-2S transition in trapped antihydrogen - Swansea University". PhD thesis. Swansea University, 2017.

[61] M. Ahmadi *et al.* "Observation of the 1S–2S transition in trapped antihydrogen". *Nature* 541.7638 (Jan. 2017). Number: 7638 Publisher: Nature Publishing Group, pp. 506–510. DOI: `10.1038/nature21040`.

[62] C. Ø. Rasmussen. "Tests of Fundamental Symmetries with Trapped Antihydrogen". PhD thesis. Aarhus University, 2016.

[63] J. Fajans and C. M. Surko. "Plasma and trap-based techniques for science with antimatter". *Physics of Plasmas* 27.3 (Mar. 19, 2020), p. 030601. DOI: `10.1063/1.5131273`.

[64] N. Madsen, F. Robicheaux, and S. Jonsell. "Antihydrogen trapping assisted by sympathetically cooled positrons". *New Journal of Physics* 16.6 (June 2014). Publisher: IOP Publishing, p. 063046. DOI: 10.1088/1367-2630/16/6/063046.

[65] C. J. Baker *et al.* "Sympathetic cooling of positrons to cryogenic temperatures for antihydrogen production". *Nature Communications* 12.1 (Oct. 22, 2021). Number: 1 Publisher: Nature Publishing Group, p. 6139. DOI: 10.1038/s41467-021-26086-1.

[66] A Christensen *et al.* "Patch Potential Induced Particle Loss in an Antimatter Penning-Malmberg Trap". Conference Name: APS Division of Plasma Physics Meeting 2019. Jan. 1, 2019.

[67] A. A. Kabantsev, K. A. Thompson, and C. F. Driscoll. "First experiments with e⁻/H⁻ plasmas: Enhanced centrifugal separation from diocotron mode damping". *AIP Conference Proceedings* 1928.1 (Jan. 23, 2018). Publisher: American Institute of Physics, p. 020008. DOI: 10.1063/1.5021573.

[68] Paolo Chiggiato. *Outgassing properties of vacuum materials for particle accelerators.* June 16, 2020. DOI: 10.48550/arXiv.2006.07124. arXiv: 2006.07124[physics].

[69] H. Drexel *et al.* "Dissociative electron attachment to hydrogen". *Journal of Physics B: Atomic, Molecular and Optical Physics* 34.8 (Apr. 2001), p. 1415. DOI: 10.1088/0953-4075/34/8/307.

[70] M. Allan and S. F. Wong. "Effect of Vibrational and Rotational Exictation on Dissociative Attachment in Hydrogen". *Physical Review Letters* 41.26 (Dec. 25, 1978). Publisher: American Physical Society, pp. 1791–1794. DOI: 10.1103/PhysRevLett.41.1791.

[71] Jacek Komasa *et al.* "Quantum Electrodynamics Effects in Rovibrational Spectra of Molecular Hydrogen". *Journal of Chemical Theory and Computation* 7.10 (Oct. 11, 2011). Publisher: American Chemical Society, pp. 3105–3115. DOI: 10.1021/ct200438t.

[72] Jinjun Liu *et al.* "Determination of the ionization and dissociation energies of the hydrogen molecule". *The Journal of Chemical Physics* 130.17 (May 7, 2009). Publisher: American Institute of Physics, p. 174306. DOI: 10.1063/1.3120443.

[73] R. L. Sacramento *et al.* "Matrix isolation sublimation: An apparatus for producing cryogenic beams of atoms and molecules". *Review of Scientific Instruments* 86.7 (July 1, 2015). Publisher: American Institute of Physics Inc., p. 073109. DOI: 10.1063/1.4926774.

[74] I. C. Lane. "Production of ultracold hydrogen and deuterium via Doppler-cooled Feshbach molecules". *Physical Review A - Atomic, Molecular, and Optical Physics* 92.2 (Aug. 24, 2015). Publisher: American Physical Society, p. 022511. DOI: 10.1103/PhysRevA.92.022511.

[75] B. C. Sawyer *et al.* "Reversing hydride-ion formation in quantum-information experiments with Be^+". *Physical Review A - Atomic, Molecular, and Optical Physics* 91.1 (Jan. 12, 2015). Publisher: American Physical Society, p. 011401. DOI: 10.1103/PhysRevA.91.011401. arXiv: 1412.0634.

[76] S. A. Jones. "An ion trap source of cold atomic hydrogen via photodissociation of the BaH^+ molecular ion". *New Journal of Physics* 24.2 (Feb. 1, 2022). Publisher: IOP Publishing Ltd, p. 023016. DOI: 10.1088/1367-2630/ac4ef3.

[77] W. Bleakney. "The ionization of hydrogen by single electron impact". *Physical Review* 35.10 (May 15, 1930). Publisher: American Physical Society, pp. 1180–1186. DOI: 10.1103/PhysRev.35.1180.

[78] Jung-Sik Yoon *et al.* "Cross Sections for Electron Collisions with Hydrogen Molecules". *Journal of Physical and Chemical Reference Data* 37.2 (June 2008). Publisher: American Institute of Physics, pp. 913–931. DOI: 10.1063/1.2838023.

[79] A. Crowe and J. W. McConkey. "Dissociative ionization by electron impact. I. Protons from H_2". *Journal of Physics B: Atomic and Molecular Physics* 6.10 (Oct. 1, 1973). Publisher: IOP Publishing, p. 2088. DOI: 10.1088/0022-3700/6/10/022.

[80] R. K. Janev, D. Reiter, and U. Samm. "Collision Processes in Low-Temperature Hydrogen Plasmas". *Forschungszentrum, Zentralbibliothek Jülich* 4105 (2003), p. 189.

[81] R. K. Janev and P. S. Krstic. "Excitation and ionization processes in slow collisions of ground-state and excited hydrogen atoms with protons". *Physical Review A* 46.9 (Nov. 1, 1992). Publisher: American Physical Society, pp. 5554–5573. DOI: 10.1103/PhysRevA.46.5554.

[82] V. Dudnikov. *Development and Applications of Negative Ion Sources*. Vol. 110. Series Title: Springer Series on Atomic, Optical, and Plasma Physics. Cham: Springer International Publishing, 2019. DOI: 10.1007/978-3-030-28437-4.

[83] L. Dodd. "Development of a proton beamline for measurements of the cross section of proton-positronium interactions for the production of H⁻". PhD thesis. Swansea: Swansea University, Jan. 1, 2020. DOI: 10.23889/SUthesis.59731.

[84] H. G. Dehmelt and F. L. Walls. "'bolometric' technique for the rf spectroscopy of stored ions". *Physical Review Letters* 21.3 (July 15, 1968). Publisher: American Physical Society, pp. 127–131. DOI: 10.1103/PhysRevLett.21.127.

[85] D. A. Church and H. G. Dehmelt. "Radiative cooling of an electrodynamically contained proton gas". *Journal of Applied Physics* 40.9 (Aug. 18, 1969). Publisher: American Institute of PhysicsAIP, pp. 3421–3424. DOI: 10.1063/1.1658214.

[86] D. S. Hall and G. Gabrielse. "Electron cooling of protons in a nested penning trap". *Physical Review Letters* 77.10 (Sept. 2, 1996). Publisher: American Physical Society, pp. 1962–1965. DOI: 10.1103/PhysRevLett.77.1962.

[87] Igor Savić, Stephan Schlemmer, and Dieter Gerlich. "Formation of H_3^+ in Collisions of H_2^+ with H_2 Studied in a Guided Ion Beam Instrument". *ChemPhysChem* 21.13 (2020). _eprint: https://onlinelibrary.wiley.com/doi/pdf/10.1002/cphc.202000258, pp. 1429–1435. DOI: 10.1002/cphc.202000258.

[88] Carl S. Weimer *et al.* "Electrostatic modes as a diagnostic in Penning-trap experiments". *Physical Review A* 49.5 (May 1, 1994). Publisher: American Physical Society, pp. 3842–3853. DOI: 10.1103/PhysRevA.49.3842.

[89] Timothy Peter Friesen. "Probing Trapped Antihydrogen. In Situ Diagnostics and Observations of Quantum Transitions". PhD thesis. Jan. 31, 2014.

[90] U. Chowdhury *et al.* "A cooler Penning trap for the TITAN mass measurement facility". *AIP Conference Proceedings.* Vol. 1640. Issue: 1 ISSN: 15517616. American Institute of Physics Inc., Feb. 17, 2015, pp. 120–123. DOI: 10.1063/1.4905408.

[91] COMSOL AB. *COMSOL Multiphysics®*. Version 5.5. Stockholm, Sweden, Nov. 14, 2019.

[92] ALPHA Collaboration *et al.* "Compression of Antiproton Clouds for Antihydrogen Trapping". *Physical Review Letters* 100.20 (May 19, 2008). Publisher: American Physical Society, p. 203401. DOI: 10.1103/PhysRevLett.100.203401.

[93] Edward H. Chao *et al.* "Self-consistent numerical solution to Poisson's equation in an axisymmetric Malmberg-Penning trap". *AIP Conference Proceedings* 498.1 (Dec. 10, 1999). Publisher: American Institute of Physics, pp. 461–468. DOI: 10.1063/1.1302149.

[94] C. Amole *et al.* "Autoresonant-spectrometric determination of the residual gas composition in the ALPHA experiment apparatus". *Review of Scientific Instruments* 84.6 (June 25, 2013). Publisher: American Institute of PhysicsAIP, p. 065110. DOI: 10.1063/1.4811527.

[95] Samuel Speller. *The Investigation of Residual Gas in Ultra High Vacuum Systems*. Master thesis. Swansea University, 2013.

[96] W. Bertsche, J. Fajans, and L. Friedland. "Direct Excitation of High-Amplitude Chirped Bucket-BGK Modes". *Physical Review Letters* 91.26 (Dec. 29, 2003). Publisher: American Physical Society, p. 265003. DOI: `10.1103/PhysRevLett.91.265003`.

[97] J. Fajans and L. Frièdland. "Autoresonant (nonstationary) excitation of pendulums, Plutinos, plasmas, and other nonlinear oscillators". *American Journal of Physics* 69.10 (Oct. 2001). Publisher: American Association of Physics Teachers, pp. 1096–1102. DOI: `10.1119/1.1389278`.

[98] G. B. Andresen *et al.* "Autoresonant excitation of antiproton plasmas". *Physical Review Letters* 106.2 (Jan. 14, 2011). Publisher: American Physical Society, p. 025002. DOI: `10.1103/PhysRevLett.106.025002`.

[99] M. Baquero-Ruiz. "Studies on the Neutrality of Antihydrogen". PhD thesis. University of California, Berkeley, 2013.

[100] L. Friedland, J. Fajans, and E. Gilson. "Subharmonic autoresonance of the diocotron mode". *Physics of Plasmas* 7.5 (May 2000). Publisher: American Institute of Physics, pp. 1712–1718. DOI: `10.1063/1.873989`.

[101] S. W. Smith. *The scientist and engineer's guide to digital signal processing*. California Technical Pub, 1997. 650 pp.

[102] M. Ahmadi *et al.* "Antihydrogen accumulation for fundamental symmetry tests". *Nature Communications* 8.1 (Sept. 25, 2017). Number: 1 Publisher: Nature Publishing Group, p. 681. DOI: `10.1038/s41467-017-00760-9`.

[103] G. Gabrielse *et al.* "Background-Free Observation of Cold Antihydrogen with Field-Ionization Analysis of Its States". *Physical Review Letters* 89.21 (Oct. 31, 2002), p. 213401. DOI: `10.1103/PhysRevLett.89.213401`.

[104] Thomas F. Gallagher. *Rydberg Atoms*. Cambridge Monographs on Atomic, Molecular and Chemical Physics. Cambridge: Cambridge University Press, 1994. DOI: `10.1017/CBO9780511524530`.

[105] J.D. Schoonwater. "Towards observing antihydrogen fluorescence: characterizing SiPMs down to 6.1 K". Master Thesis. Eindhoven University of Technology, June 2022.

[106] G. B. Andresen *et al.* "Centrifugal separation and equilibration dynamics in an electron-antiproton plasma". *Physical Review Letters* 106.14 (Apr. 4, 2011). Publisher: American Physical Society, p. 145001. DOI: `10.1103/PhysRevLett.106.145001`.